ABSTRACT

Title of Dissertation: DIRECT INK WRITING SOLID-STATE LI+ CONDUCTING CERAMICS FOR NEXT GENERATION LITHIUM METAL BATTERIES

Griffin Luh Godbey, Doctor of Philosophy, 2024

Dissertation directed by: Dr. Eric Wachsman
Department of Materials Science and Engineering

The global pursuit of safer and higher-capacity energy storage devices emphasizes the crucial link between the microstructures of electrochemically active materials and overall battery performance. The emergence of solid-state electrolytes featuring multi-layered, variable porosity microstructures presents fresh opportunities for developing the next generation of rechargeable batteries. However, this advancement also brings forth novel challenges in terms of device integration and operation. In this dissertation, solid-state Li-ion conducting electrolytes were 3D printed to enhance the performance of porous electrolyte layers within porous-dense-porous trilayer systems.

LLZO-based garnet electrolyte scaffolds were fabricated via 3D printing using direct ink writing (DIW), facilitating the generation of scaffolds with minimal tortuosity and constriction in comparison to previous porous scaffolds manufactured through tape casting. Rheological

techniques, including stress and time sweep tests, were employed to characterize the DIW inks and discern their conformal and self-supporting properties.

The analysis focused on ink characteristics critical for Direct Ink Writing (DIW), emphasizing properties essential for achieving high aspect ratio printing and minimal constriction in 3D structures. Drawing from this ink research, two distinct 3D architectures, columns and grids, were fabricated. Column structures were utilized in assembling Li-NMC622 and Li-SPAN cells, with detailed discussions highlighting improvements in printing and sintering outcomes. Notably, NMC622, characterized by larger particle sizes, demonstrated complete infiltration within 3D printed porous networks, yielding a promising specific capacity of 169.9 mAh/g with minimal capacity fade. Further optimization involved integrating a porous 3D scaffold to facilitate SPAN infiltration in Li-SPAN cells, resulting in a specific capacity of 1594 mAh/g, albeit with significant capacity fade. The Li-S was implemented into a grid structure achieving 763 mAh/g_S with less than 0.25% capacity loss over 16 cycles. Lastly, comprehensive morphology analysis was conducted to evaluate the effectiveness of our optimal DIW structures and to inform future enhancements of such cells.

DIRECT INK WRITING SOLID-STATE LI+ CONDUCTING CERAMICS FOR NEXT GENERATION LITHIUM METAL BATTERIES

by

Griffin Luh Godbey

Dissertation submitted to the Faculty of the Graduate School of the
University of Maryland, College Park, in partial fulfillment
of the requirements for the degree of
Doctor of Philosophy
2024

Advisory Committee:
Professor Eric Wachsman, *Chair*
Associate Professor Yifei Mo
Associate Professor Isabel Lloyd
Assistant Professor Paul Albertus
Professor Nam Wang, *Dean's Representative*

Dedication

To Mom, Dad, and Erika,

Your unwavering support and guidance have been the cornerstone of my journey. Your encouragement fueled my determination, and your sacrifices made this journey possible. This degree is not just a testament to my hard work, but to the love and support you've given me along the way. It's as much yours as it is mine.

With deepest appreciation,

Griffin

Acknowledgements

To Dr. Eric Wachsman for his professional guidance, insights into academic writing, and lessons of leadership over the years.

To Dr. Gibson Scisco, Dr. George Alexander, Dr. Prem Jaschin, and Dr. Christopher Tang for the academic advice, paper revisions, the regular lunches, the occasional chess match, and most importantly the best support a person could ask for.

To Dr. Evans Gritton, Dr. Muhammad Saqib, Aniqa Anjum, and Dr. Yi-Lin Huang for being the best office mates, providing invaluable support, and offering invaluable advice during challenging times.

To Dr. Ichiro Takeuchi for his professional advice, positivity, and assistance through the last few years.

To Dr. Shaomao Xu, Hua Xie, Qi Dong, and Dr. Jiaqi Dai for their help with battery assembly and testing over the years.

To John Hummel, Mark Lecates, John Abrahams, and Tom Laughran for their guidance and assistance will all sorts of advanced tools in the UMD FabLab.

To Dr. Aldo Ponce, Dr. Nikhil Subraveti and Dr. Srinivasa Raghavan for guidance on how to utilize rheology for my experiments and ultimately for access to their rheometers.

To Rick Blanton and his team for maintenance of the n-Scrypt printer.

To my other lab colleagues, including but not limited to: Dr. Changmin Shi, Dr. Tanner Hamann, William Schubert, Michael Danner, Dr. Lei Zhang, Dr. Yaoyu Ren, Jon O'Neill, Adam Blickley, Dr. Sam Horlick, and Tyler Rae, for their collaborative spirit, support, and assistance throughout this journey.

Table of Contents

Dedication ii

Acknowledgements ii

List of Tables vii

List of Figures viii

List of Abbreviations xiv

Chapter 1: Lithium-ion Batteries 1

1.1 Organic Liquid Electrolytes 3
1.1.1 Background 3
1.1.2 Material Challenges/Safety 5
1.2 Solid-State Lithium-Ion Electrolytes 7
1.2.1 Background 7
1.2.2 Lithium Garnet 9
1.2.3 Improving the Interface for $Li_7La_3Zr_2O_{12}$ 10
1.2.4 Improved Cell Performance with Three-Dimensional Structures 12
1.2.5 Effects of Microstructure on Conductivity 13
1.3 Research Objective: Develop Li Garnet Inks for Direct Ink Writing for Porous Electrolyte Control 16

Chapter 2: Development of Li Garnet Inks for Direct Ink Writing 18

2.1 Fundamentals of Direct Ink Writing 18
2.1.1 Background 18
2.1.2 Direct Ink Writing Concepts and Design Goals 19
2.2 Rheology Background 20
2.2.1 Concepts 20
2.2.2 Stress and Time Sweeps 22
2.2.3 Viscoelastic Recovery 25
2.3 Rheology Testing 27
2.3.1 Oscillatory Stress Sweeps 27
2.3.2 Oscillatory Time Sweeps 29
2.3.3 Oscillatory Frequency Sweeps 33
2.4 Ink Composition 34
2.5 Particle Size and Ink Rheology 36
2.6 Aging Effects 39
2.7 Tuning Ink Rheology for Direct Ink Writing 40
2.8 Conclusions 41

Chapter 3: Direct Ink Writing $Li_7La_3Zr_2O_{12}$ Columns 43

3.1 Implementing NMC into 3D Structures 43
3.1.1 Li-NMC Solid State Batteries 43
3.1.2 Evolution of Li-Garnet 3D Structures 43
3.2 Substrate Design 45
3.2.1 Tape Casting Li-Garnet Bilayers 45
3.2.2 Laser Cutting for Increasing Sample Throughput 46
3.3 Direct Ink Writing 48
3.3.1 Direct Ink Writing Controls for Column Printing 48
3.3.2 Column Design 50
3.4 3D Printing Process 51
3.4.1 N-scrypt Commands 51
3.4.2 Troubleshooting 52
3.5 Sintering 3D Structures 53
3.5.1 Sintering Setup and Procedure 53
3.5.2 Post-sintering Processing 55
3.6 Effects of Solvents on Structure 55
3.7 Column Structures and Surface Morphology 58
3.8 Li-NMC Cell Assembly and Testing 60
3.9 Column Structures with a Li-SPAN Battery 65
3.9.1 SPAN Background 65
3.9.2 SPAN Cell Assembly and Results 67
3.10 Conclusions 68

Chapter 4: Direct Ink Writing $Li_7La_3Zr_2O_{12}$ Grids for Li-S Batteries 69

4.1 Direct Ink Writing Li Garnet Grid Structure 69
4.1.1 Sulfur Cathodes 69
4.1.2 Grid Structures for Cathode Scaffolds 70
4.2 3D Printing Design 71
4.2.1 Substrate Design 71
4.2.2 Structure Design 72
4.3 3D Printing Grid Structures 73
4.3.1 N-scrypt Instructions and Raster Design 73
4.3.2 Direct Ink Writing Grid Adjustments 74
4.4 Sintering LLZO Grid Structures 75
4.4.1 Sintering and Post Sintering Procedure 75
4.4.2 Shrinkage-Based Cracking 76
4.5 Cell Assembly and Cycling 77
4.5.1 Lithium Symmetric Testing 77
4.5.2 Sulfur Infiltration and Cell Assembly 78
4.6 Li-S Cell Results and Analysis 80
4.6.1 Li-S Impedence and Cycling 80
4.6.2 Tortuosity and Constriction in Grids 82
4.7 Direct Ink Writing Symmetric Cells 82

4.8 Conclusions 86

Chapter 5: Overall Conclusions and Future Outlook 88

5.1 Summary of Research Results 88
5.1.1 Li-Garnet Inks and their Rheological Properties 88
5.1.2 Li-Garnet Column Structures 89
5.1.3 Li-Garnet Grid Structures 90
5.2 Future Work 91
5.2.1 Tying Particle Size to Rheology 91
5.2.2 Effects of 3D structure on Lithium Cycling 92
5.2.3 Implementation of MIEC into DIW inks 92
Appendices 94

Appendix A: Example Ink Recipes for LLZO 94
Appendix B: Excerpt of Text Code Used to 3D Print Column Structures 94
Appendix C: Text Code Used to 3D Print Grid Structures 96
Bibliography 99

List of Tables

Table 1.1: Select incidents of battery fires around the world between 2013 and 2018. 6

Table 3.1: Compiled information about the 3D printed structures and cells shown in figure 3.13. Additional surface area represents the percent increase to surface area compared to a planar interface. Surface area to volume ratio only considers the surface area and volume added by the columns. Porosity is calculated from the void space between the columns and nothing above the column height. Impedance is measured from the EIS. Discharge capacity was taken from the initial capacity after the formation cycle and coulombic efficiency is the final coulombic efficiency after 20 cycles. 63

Table 4.1 presents compiled information regarding the 3D printed structure and cell shown in figure 4.8. Additional surface area denotes the percentage increase compared to a planar interface. Porosity is calculated based on the void space within the grid structure. Impedance is measured via EIS across a frequency range from 1 MHz to 1 Hz. Discharge capacity refers to the initial capacity, while coulombic efficiency represents the final coulombic efficiency. 81

List of Figures

Figure 1.1: Lithium solid-state battery publication analysis showing (a) number of publications by year during 2000 to 2020 and (b) radar plot depicting the distribution of research in key technical areas. 1

Figure 1.2: Left) Basic schematic of a battery charging. Right) Basic schematic of a battery discharging. 3

Figure 1.3: Total number of electric vehicles by segment and market between 2015 to the projection of 2025. 4

Figure 1.4: The global count of aviation battery fires caused by thermal runaway from the very first incident in 1996 to 2019. 5

Figure 1.5: Li metal anode growing a dendrite through PEO during battery cycling. 6

Figure 1.6: Radar plots of various solid-state electrolytes including oxides (a), sulfides (b), hydrides (c), halides (d), thin films (e), and polymers (f). 8

Figure 1.7: a) Schematic of Li metal wetting on LLZO before and after ALD interlayer deposition. b) SEM demonstration LLZO wetting without ALD layer and with ALD layer. 10

Figure 1.8: EIS measurements of Li-Li symmetric cells with and without Al_2O_3 ALD. The sample with ALD layer has an inlay to highlight its over 20x drop in impedance. 11

Figure 1.9: a) Schematic of Li-Li symmetric cell built utilizing a tapecast-trilayer LLZO structure. b) SEM cross section of Li-Li symmetric cell built utilizing a trilayer LLZO structure. 13

Figure 1.10: Trilayer structure produced by tape casting and freeze casting Li garnet. . 13

Figure 1.11: Schematics demonstrating a) geometric tortuosity, b) percolation factor, and c) constriction factor. 15

Figure 1.12: Microstructure terms plotted for various porosity LLZO samples ranging from 0% porosity to 56.67% porosity. P is percolation factor, $1/\tau^2$ is the tortuosity component, β is constriction factor, f is the volume fraction, and M-factor is the combined effect on conductance of all of the previous factors. 15

Figure 2.1: The viscosity data for the self-supporting ink was compared with that of a conformal ink exhibiting Newtonian behavior. Viscosity of the self-supporting and

conformal inks wer measured at 1500 cP and 1090 cP respectively. The self-supporting ink exhibited a yield stress of 280 Pa, while the conformal ink showed no yield stress. 19

Figure 2.2: Viscosity measurements of a non-Newtonian LLZO ink exhibiting shear thinning. This ink had 68 wt%$_{LLZO}$ loading and 32 wt% organic solvents. 21

Figure 2.3: LLCZN ink oscillatory stress sweep test. The concept of flow point is demonstrated at where δ is 45° and where G" becomes larger than G′. 23

Figure 2.4: LLCZN ink oscillatory time sweep test or 3ITT. Interval I and III are low stress holds below the flow point and interval II is a high stress hold above the flow point. 24

Figure 2.5: Rheological data for two inks and their corresponding 3D printed structures. a-b) Stress sweep results of ink A and ink B, respectively. c-d) Time sweep resultf of ink A and ink B, respectively. e-f) SEM cross-section images depicting column structures printed using ink A and ink B, respectively. 26

Figure 2.6: Oscillatory stress-sweep rheology tests of three different inks; a) ink 1 – conformal ink, b) ink 2 – semi self-supporting ink, and c) of ink 3 – conformal ink. G′ and G" of ink 3 are inaccurate due to exceeding the maximum measurable modulus of the rheometer. 28

Figure 2.7: Initial G' and complex viscosity of inks 1, 2, and 3. Both G' and η^* of ink 3 is approximated from the time sweep $G"$ and assuming initial δ is 10°. 29

Figure 2.8: Oscillatory time-sweep rheology tests of three different inks; a) ink 1 – conformal ink, b) ink 2 – semi self-supporting ink, and c) of ink 3 – conformal ink. G′ and G" of ink 3 are inaccurate due to exceeding the maximum measurable modulus of the rheometer. 31

Figure 2.9: Normalized data from interval III of the 3 ink samples from the time sweep test in figure 2.8. Data is normalized using each of the inks G_0' as 0 and G_∞' as 1. 32

Figure 2.10: Frequency sweeps of two Li-garnet inks: a) low-modulus, conformal ink and b) high-modulus, semi self-supporting inks. 33

Figure 2.11: Photograph of two inks tilted on a 50° stage to demonstrate the difference between self-supporting and conformal inks. 34

Figure 2.12: Figure 2.12: Scatter plot of several LLCZN inks with various LLCZN wt% (right). G′ increases as LLCZN wt% increases. Vol % of the LLCZN powder is also plotted (left). 35

Figure 2.13: Scatter plot of several LLCZN inks with various LLCZN wt%. τ increases as LLCZN wt% increases. 36

Figure 2.14: Particle size in diameter of LLCZN powder supplied by Trans-Tech. 37

Figure 2.15: Plot of ink compositions 69±0.3 wt%$_{LLCZN}$ with differing particles size measured by DLS. Each of these inks low stress G' as measured with a oscillatory stress sweep. 38

Figure 2.16: a) Particle size distributions from the inks in figure 2.15. b) G' plotted against average particle size data from figure 2.15 labeled for reference. LLZO powder in inks 1 and 2 were milled for 2 to 3 additional weeks where as LLZO ink inks 3 and 4 were only milled for 1 additional week. 39

Figure 2.17: Oscillatory stress sweep of an ink after 14 days compared to its initial stress sweep. Original ink was G'' dominant, but after two weeks the ink became G' dominant and increased modulus by over 2 orders of magnitude. A slight slip happened at round 1000 Pa stress for the 14-day sample which caused a slight deviation in the high stress measurements. 40

Figure 3.1: 3D schematic of our NMC622-Li full cell with an electrolyte scaffold made through direct ink writing. Self-supporting columns are printed on the dense side of a bilayer substrate. Lithium metal is infiltrated on the random porous side and NMC622 with carbon black infiltrated on the 3D printed side. 45

Figure 3.2: Laser cutting profile used for laser cutting the 4 cm by 4 cm LLCZN tape samples. Individual squares are 1.1 cm by 1.1 cm. The pattern is slightly larger than 4 cm by 4 cm to ensure proper cutting to the edges of the sample. 47

Figure 3.3: Nine 3D-printed column samples were produced on a laser-perforated sample. The entire sample measures 4 cm by 4 cm, with each internal sample measuring 1.1 cm by 1.1 cm. The sample is taped to the plate below to prevent sliding during the 3D printing process. 48

Figure 3.4: Top-down images depict 3D printed columns arranged in a hexagonal pattern: a) an optical image of inks before sintering, and b) a profilometer heat map generated from a sintered column structure. 51

Figure 3.5: Sintering profile of Li-garnet in tube furnaces. The entire process is done in flowing oxygen for just under 24 hours. Holds are at 240°C, 600°C, and 1100°C. . 54

Figure 3.6: XRD pattern of LLZO powder from Trans-Tech after sintering (black) and its Rietveld refinement (Red). No splitting at the peaks indicates cubic phase as opposed to tetragonal. 54

Figure 3.7: SEM images depict columns printed with high solvent loading, resulting in damage to the dense layer due to uneven drying after rewetting of the layers during the 3D printing process. 56

Figure 3.8: SEM images reveal excellent contact between the 3D printed garnet columns and the dense garnet. Accidental knocking over of the column during handling resulted in the extraction of a significant portion of the dense garnet, highlighting the intimate contact achieved. 57

Figure 3.9: SEM images depict samples with 3D printed columns containing varying ethanol content: a) 5.1 wt% EtOH, b) 2.2 wt% EtOH, and c) 1.8 wt% EtOH. 57

Figure 3.10 a-b) Top-down images show 3D printed columns employing high viscosity inks with rapid recovery time. a) Top-down optical microscope images capturing the pre-sintering 3D printed column structure. b) Isometric view of a column sample before sintering. c) Top-down SEM image capturing the sintered 3D printed column structure. d) Cross section view of a column sample after sintering. 58

Figure 3.11 a-c) SEM images of various sintered column structures a) columns printed with more conformal inks. b) Columns printed with semi self-supporting inks. c) Columns printed with self-supporting inks. 59

Figure 3.12: SEM images show 3D printed cells infiltrated with a NMC622 slurry containing carbon black. a) Top-down view of columns coated with the drop-casted NMC622 slurry. b) Presents cross-section images showing the close contact between the NMC622 slurry and the 3D printed Li-garnet electrolyte. 61

Figure 3.13: a-c) SEM cross-section images illustrate the DIW structure of three cells reported in this work. d-f) EIS measurements were conducted on the structures when assembled into Li-NMC622 cells. g-i) Cell cycling results show 20 cycles for each of the assembled structures in Li-NMC622 cells. The cells were tested between 2.5V to 4.3V, a rate of 0.05C, and at room temperature (22°C). 62

Figure 3.14: Bar chart comparing the theoretical capacities of LFP (170 mAh/g), NMC622 (277 mAh/g), and elemental sulfur (1675 mAh/g). 66

Figure 3.15: Comparison of 3D printed Li-SPAN cell (a) and bilayer Li-SPAN cell from literature (b).[108] 3D printing allowed achieving theoretical capacity of SPAN at 1594 mAh/g_S. with 7.5 mg_S/cm^2 loading. Bilayer SPAN cell did not achieve theoretical and only had 1.0 mg_S/cm^2 loading. Both cells were cycled at 60°C at similar rates. 67

Figure 3.16: SEM images revealing degradation of the SPAN/LiFSI after cycling caused by volume expansion and loss of cathode contact. 68

Figure 4.1: a) 3D schematic of a grid DIW electrolyte scaffold. b) Schematic representation of a complete Li-S/C cell, showcasing Li metal infiltration on the porous side of the bilayer and sulfur and carbon infiltration into the 3D printed side opposite to the Li metal. 71

Figure 4.2: Top-down optical microscope images depict 3-layer grid structures. Layers 1 and 3 are aligned in the same direction, while layer 2 runs perpendicular to layers 1 and 3. Layers 1 and 3 are offset from each other, allowing both layers to be visible in the optical image. 74

Figure 4.3: a-c) Top-down optical microscope images showcasing 3D printed grid structures prior to sintering. High-definition representations of each structure were obtained, demonstrating precise control during the 3D printing process. 75

Figure 4.4: Splitting in the dense layer due to excess liquid absorption, resulting in localized weaknesses that cracked during sintering. 75

Figure 4.5: Shrinkage-induced cracking is evident in the grid structure both before and after sintering. a-b) depict grid structures experiencing structural breakages during the drying process after 3D printing. c-d) show an increased frequency of grid structure breakages after sintering, likely due to greater shrinkage during the organic burnout step. 77

Figure 4.6: a) Li-Li symmetric cell EIS area-normalized Nyquist plot was reported by McOwen et al. b) SEM of the 3D printed raster pattern reported by McOwen et al. c) Li-Li symmetric cell EIS area-normalized Nyquist plot is presented in this study. d) SEM of the 3D printed raster pattern printed for direct comparison to past work. 78

Figure 4.7: Cross-sectional image showcasing intimate interface between the S/C slurry and the 3D printed grid LLZO electrolyte. 79

Figure 4.8: Figure 4.8: a) EIS measurement of a Li-S/C with an inlayed SEM of the 3D printed grid microstructure. b) Cell cycling results of this cell after cycling 16 cycles. The cell had a mass loading of 1 mg_S/cm^2, had impedance measured from 1 MHz to 1 Hz, and was full cell cycled between 1.1V to 3.0V and a rate of 0.02C. 80

Figure 4.9: Image of the 3D printing support for DIW double-sided samples. Square inlays serve as rests for 3D printing on the first side while the second side is being printed. During the printing process, the sample is secured to the sample holder with tape. 83

Figure 4.10: SEM cross-sectional image of a symmetrical 3D printed cell. Both grid patterns on opposing sides exhibit self-supporting characteristics while maintaining effective contact with the initial layer to mitigate constriction. The density of the dense layer appears satisfactory for the designated thickness. 85

Figure 4.11: The SEM cross-section of a Li wet sample of a 3D printed raster pattern. In the middle of the image, a 3D printed feature is visible, with open space on the left unfilled by Li metal, while the space on the right is fully occupied by Li metal. Uniform application of Li metal was applied across the entire surface of this sample. . 86

Figure 5.1: Three images of various DIW inks: a) standard LLZO ink, b) MIEC ink with 1 to 1 LLZO replacement, and c) adjusted MIEC ink. 93

List of Abbreviations

ALD	Atomic layer deposition
ASR	Area specific resistance
β	Constriction factor
BBP	Benzyl butyl phthalate
δ	Phase angle (for rheology)
Δl	Length of travel pathways through porous microstructure
Δx	Straight path distance across porous microstructure
DLS	Dynamic light scattering
DMC	Dimethyl carbonate
DME	1,2-dimethoxyethane
EC	Ethylene carbonate
ESL	Electro Science Labs (Company)
EV	Electric Vehicle
G^*	Complex modulus (for rheology)
G'	Storage modulus (for rheology)
$G^{"}$	Loss modulus (for rheology)
G_0	Initial modulus (for rheology)
G_∞	Steady-state modulus (for rheology)
γ	Shear strain
Li	Lithium
LFP	Lithium iron phosphate
LIFSI	Lithium bis(fluorosulfonyl)imide
$LiPF_6$	Lithium hexafluorophosphate
LISICON	Lithium superionic conductor
LiTFSI	Lithium bis(trifluoromethanesulfonyl)imide
LLCZN	Calcium and niobium doped lithium lanthanum zirconium oxide ($Li_7La_{2.75}Ca_{0.25}Zr_{1.75}Nb_{0.25}O_{12}$)
LLZO	Lithium lanthanum zirconium oxide ($Li_7La_3Zr_2O_{12}$)
M	M-factor/microstructure factor (for conductivity calculation)
$n_{\text{phase, connected}}$	Total units in the phase that are non-isolated (for percolation factor calculation)
$n_{\text{phase, total}}$	Total units in the phase (for percolation factor calculation)
NMC	Nickel manganese cobalt oxide
NMC622	Nickel manganese cobalt oxide ($LiNi_{0.6}Mn_{0.2}Co_{0.2}O_2$)
P	Percolation factor
Pa	Pascals (pressure unit)
PEO	Polyethylene oxide
PMMA	Poly-(methyl methacrylate)
Psi	Pounds per square inch ($lb/in.^2$) (pressure unit)
PVB	Polyvinyl butyral
r_{min}	Minimum cross-sectional radius (for constriction factor calculation)
r_{max}	Maximum cross-sectional radius (for constriction factor calculation)

σ	Shear stress (for rheology)
σ_{bulk}	Bulk conductivity material property (for conductivity calculation)
$\sigma_{effective}$	Effective conductivity of a material (for conductivity calculation)
SEI	Solid electrolyte interface
SEM	Scanning electron microscope
SPAN	Sulfurized polyacrylonitrile
SSB	Solid-state battery
SSE	Solid-state electrolyte
τ	Recovery time (for rheology)
τ_{geo}	Geometric tortuosity
τ_{50}	Recovery time for 50% of the steady-state modulus (for rheology)
XRD	X-ray diffraction
YSZ	Yttria Stabilized Zirconia
3D	Three-dimensional

Chapter 1: Lithium-ion Batteries

The surge in mobile technology and the increasing demand for environmentally friendly power sources in transportation have propelled battery technology into the forefront of research.[1–3] Current battery technologies are insufficient to satisfy the demands for batteries in grid storage systems, portable electronics, and electric vehicles.[1,2] Additionally, addressing the prevalent safety concerns associated with Li-ion battery technology has become imperative.[1–3] Over the past two decades, there has been a significant increase, approximately 24 times, in publications on lithium solid-state batteries. However, only a small fraction of these publications have centered on processing and manufacturing aspects as seen in figure 1.1.[4]

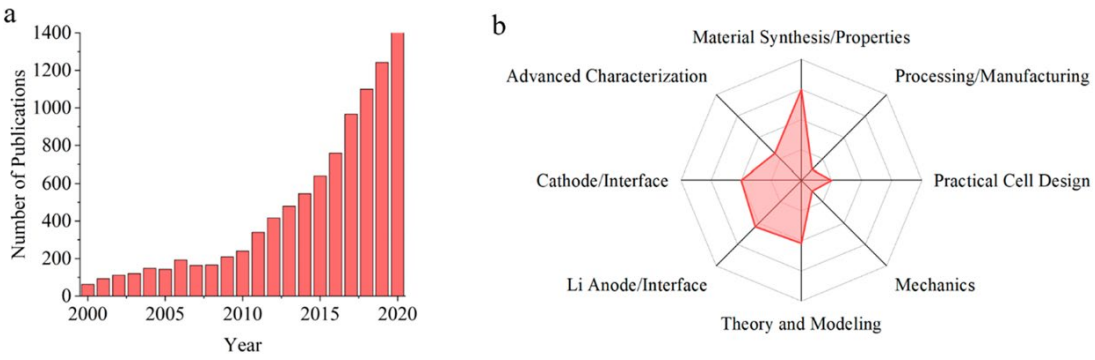

Figure 1.1: Lithium solid-state battery publication analysis showing (a) number of publications by year during 2000 to 2020 and (b) radar plot depicting the distribution of research in key technical areas.[4]

Batteries like other energy producing methods store energy in the form of chemical potential energy and release it in the form of direct current.[5] Batteries can be broken down into 4 major components: cathode, anode, electrolyte, and current collectors. Anodes naturally oxidize, while cathodes undergo reduction, establishing

the potential that determines the voltage of the anode-cathode pair. These two electrodes are separated by an ionically conductive and electronically insulating electrolyte. This setup forces the electrons to traverse through the electronically conductive current collectors and the ions to diffuse through the electrolyte. Commonly, a separator is incorporated into the electrolyte to prevent direct contact between the anode and cathode. During discharge, electrons move from the anode to the cathode, and during charging, electrons flow in the opposite direction as seen in figure 1.2. The potential energy stored in the battery is determined by the pairing of the cathode and anode, as well as their respective quantities. Current collectors establish a highly conductive pathway for negatively charged electrons, while the electrolyte establishes a highly ionic-conductive pathway for positively charged ions, such as Li^+, in lithium-ion batteries. Both negative electrons and positive ions will reunite to maintain charge neutrality. The electrolyte must not conduct electricity or permit the formation of electrically conductive species that bridge between the anode and the cathode; otherwise, electrons will bypass the current collectors, leading to a short circuit.

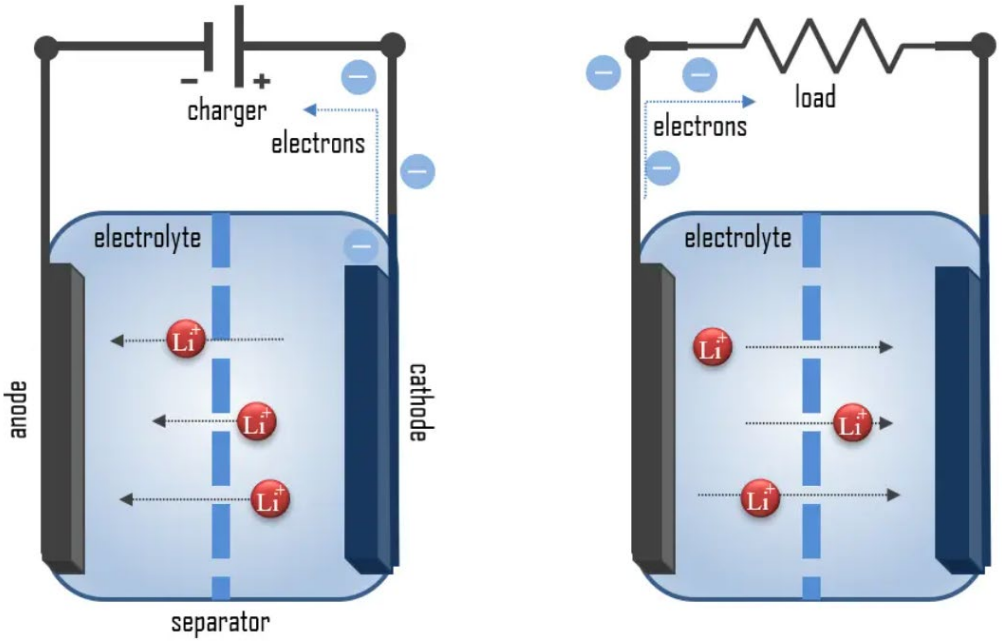

Figure 1.2: Left) Basic schematic of a battery charging. Right) Basic schematic of a battery discharging.[6]

1.1 Organic Liquid Electrolytes

1.1.1 Background

In contemporary lithium-ion batteries, a $LiPF_6$ organic liquid electrolyte separates a graphite anode from a lithium metal oxide cathode, such as $LiCoO_2$.[7] Battery technology has progressed slowly, particularly concerning the miniaturization of electronics, despite its apparent simplicity. Exxon pioneered lithium batteries in the 1970s, which led to the discovery that the lithium anode could react with the electrolyte, resulting in device explosions.[1,8] In the late 1970s to the early 1990s, John Goodenough utilized lithium metal oxides in cathodes to circumvent compatibility issues associated with lithium metal.[9–12] Sony produced modern commercial lithium-ion battery technology in 1991, employing graphite and lithium transition metal

oxides derived from Goodenough's research.[1,7] Liquid electrolytes, like $LiPF_6$ in EC or DMC, have dominated the modern battery market owing to their high ionic conductivity, typically around 1×10^3 S/cm.[13,14] This specific liquid electrolyte chemistry exhibited both high Li-ion conductivity (~10^{-3} S/cm) and the capacity to establish a stable SEI that passivated the electrolyte-graphite interface, significantly reducing detrimental side reactions responsible for performance deterioration.[14] To prevent the anode from bridging over to the cathode and forming a short circuit, a physical membrane or separator is necessary when using liquid electrolytes.

The surge in electric vehicle adoption over the past decade has led to a significant increase in demand for newer and improved batteries, reaching unprecedented levels.[15] In less than 10 years, the number of electric vehicles used has exploded from virtually none to hundreds of millions.[15]

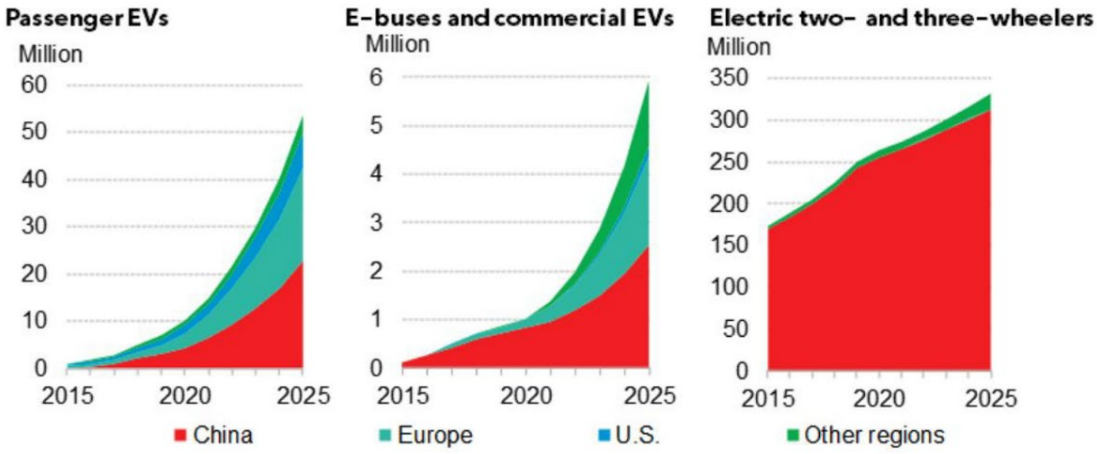

Figure 1.3: Total number of electric vehicles by segment and market between 2015 to the projection of 2025.[15]

Amidst the rise in electric vehicles, there has been an unprecedented increase in battery-related thermal runaway fires as seen in figure 1.4.[16] To sustain the

electrification of transportation and personal electronic devices, it is imperative to explore solutions and alternatives to mitigate the flammability of batteries.

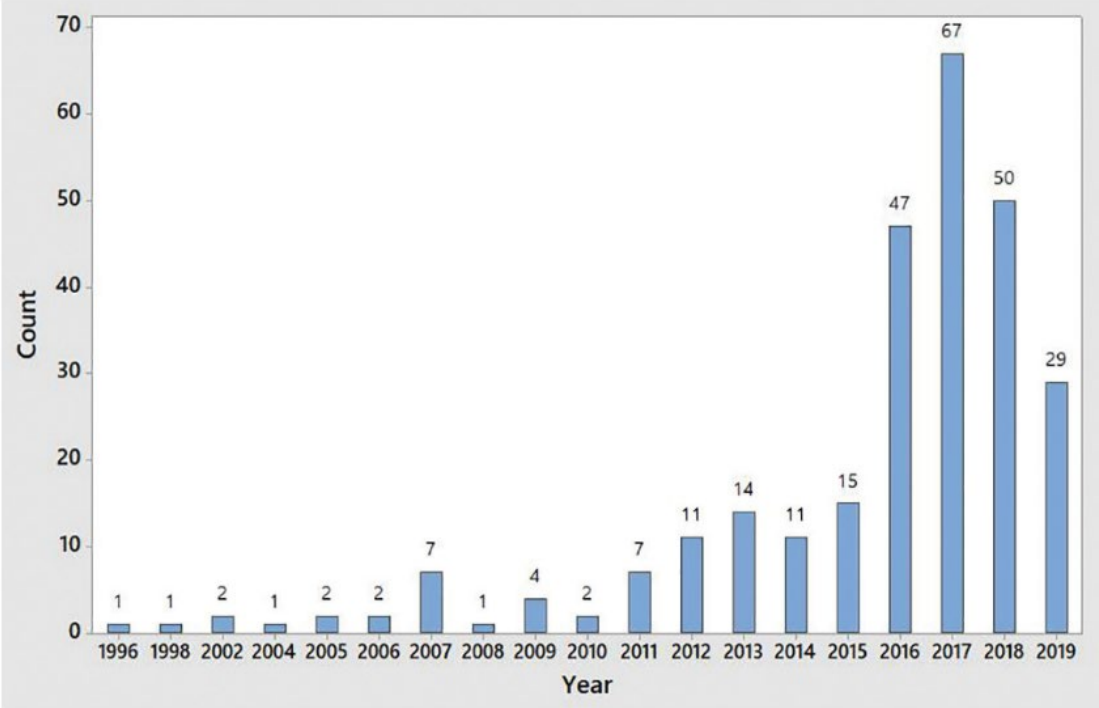

Figure 1.4: The global count of aviation battery fires caused by thermal runaway from the very first incident in 1996 to 2019.[16]

1.1.2 Material Challenges/Safety

$LiPF_6$, often mixed with carbonates, are crucial in both sustaining high ionic conductivity and ensuring electrode contact.[17,18] These electrolytes have low flash points, posing a significant danger, especially when exposed to oxidation reactions, leading to numerous fire-related accidents.[19–28] Attempts to mitigate the flammability in these electrolytes involves adding flame-retardant at the cost of electronic conductivity.[14,29]

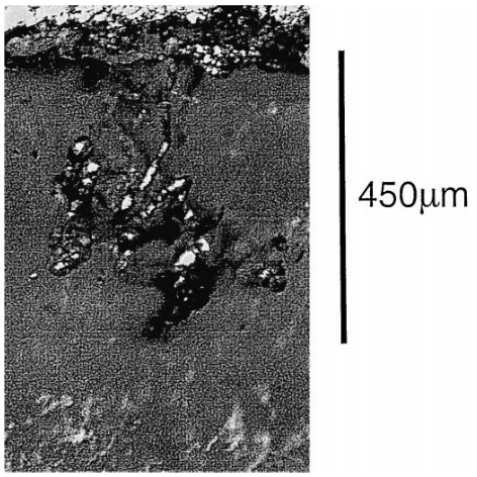

Figure 1.5: Li metal anode growing a dendrite through PEO during battery cycling.[30]

Table 1.1: Select incidents of battery fires around the world in between 2013 and 2018.[26]

Device	Date	Location	Description
Mobile Phone	2016/08/24	Korea	First explosion of a Samsung Note7 (World).[19]
	2016/09/18	China	First explosion of a Samsung Note7 (China).[19]
	2018/12/30	United States	User burned form iPhone XS max self-ignition.[20]
Electric Vehicles	2013/10/02 & 2017/10/18	United States	Tesla Model S fire after accident.[26,27]
	2016/01/01	Norway	Tesla Model S fire during charging.[21]
	2016/05/14	China	EV bus fire due to battery short.[21]
	2016/09/07	Netherlands	Tesla Model S battery fire killed driver.[21]
	2017/01/15 & 2018/05/21	China	EV bus self-ignited during operation.[22,23]
	2017/02/19	China	Tesla Model X fire after crash.[22]
	2017/05/01	China	EV bus fire during charging.[22]
	2018/03/24	United States	Tesla Model S fire.[23]
Airplanes	2013/01/07	United States	Boeing 787 battery pack fire.[24]
	2013/01/16	Japan	Boeing 787 fire midflight.[25]

$LiPF_6$-based electrolytes incorporate solid separators to inhibit the growth of electronically conductive dendrites within the battery.[31] Soft materials such as liquid electrolytes do not block dendrites from short circuiting the cell. Brissot et al.

demonstrate the formation of lithium dendrites in a lithium symmetric cell using a PEO electrolyte containing LiTFSI.[30]

$LiPF_6$ electrolytes exhibit a narrow stability range and decompose above 4.5V (vs. Li/Li^+), limiting the utilization of high-voltage cathodes and thus impeding the potential energy density of such systems.[3,32] This decomposition often means excluding the high specific capacity anode Li metal as it forms an unstable SEI layers with liquid carbonate electrolytes, resulting in capacity loss. Elemental sulfur is recognized as a promising cathode material due to its high theoretical capacity of 1670 mAh/g.[33,34] However, when paired with $LiPF_6$-based electrolytes, specific lithium sulfide species dissolve into the electrolyte, leading to irreversible capacity loss.[33–39] This phenomenon is known as the "polysulfide shuttle effect."[33,34]

1.2 Solid-State Lithium-Ion Electrolytes

1.2.1 Background

SSBs have emerged as a compelling technology to address the increasing demand for next-generation energy storage. They offer potential for high energy density and reduced flammability concerns.[4,40,41] Solid electrolytes should naturally fill the role of a physical separator to block dendritic growth with increased hardness.[42–44]

There are a number of new SSE technologies (oxides, sulfides, hydrides, halides, thin films, and polymers).[2] Oxides such as perovskites, NASICON, and Li-garnet have high ionic conductivity, chemical and electrochemical stability, voltage window, and mechanical strength.[2] Sulfides including Li_2S-SiS_2 and thio-LISICON have high ionic conductivity, mechanical strength, and flexibility.[2] $LiBH_4$, $LiNH_2$,

and other hydrides have high ionic conductivity, mechanical strength, flexibility, and stability with lithium metal, the golden standard anode.[2,40,45] The low intergranular resistance makes sulfides and hydrides very promising materials.[2] Halides and thin films are potentially suitable SSE, but they have ionic conductivities at least two orders of magnitude lower than oxides, sulfides, and halides.[2]

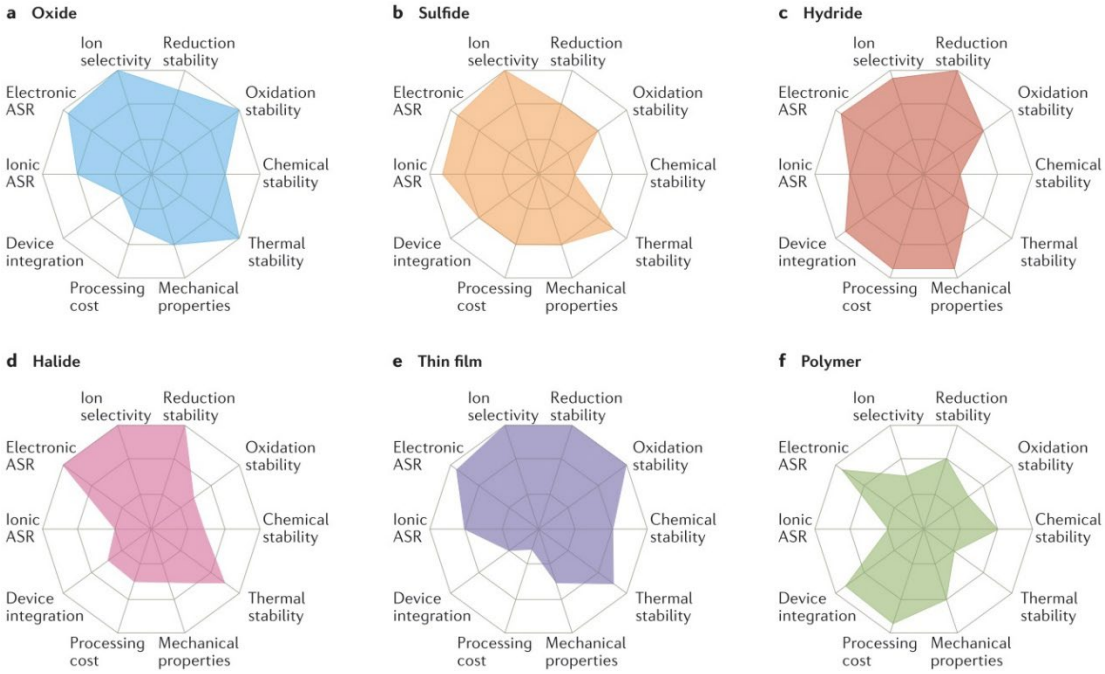

Figure 1.6: Radar plots of various solid-state electrolytes including oxides (a), sulfides (b), hydrides (c), halides (d), thin films (e), and polymers (f).[2]

Polymers often do not have the mechanical support to prevent dendrites as well as they have a limited voltage stability window, so they cannot pair with high potential cathode-anode pairings.[2,30] Taking a closer look at sulfides and hydrides, both of these SSEs are sensitive to moisture meaning these materials will need to be kept in dry environments during synthesis.[2] Controlling moisture tends to be more difficult during synthesis meaning oxides seem to have a distinct advantage over other SSEs.

Many SSEs have much better stability with higher capacity cathodes such as elemental sulfur.[2] The "polysulfide shuttle effect" does not occur in SSEs, indicating that SSEs will outperform conventional liquid electrolytes as long as the electrolyte does not react with elemental sulfur or any of the lithium polysulfide species.[46]

1.2.2 Lithium Garnet

Previously established is the oxide SSE show a great promise among emerging SSE technologies. Among the oxide SSEs, cubic Li-garnet ($Li_7La_3M_2O_{12}$, M = Zr, Ta, Nb) is one of the promising SSEs with its nonflammable, wide electrochemical stability windows, and its high ionic conductivity (~1 mS/cm).[47–50] Its high elastic modulus (156 GPa) and hardness (13 GPa) make it strong enough to block Li metal dendrites allowing it to act as a separator in addition to a SSE.[51] First principles studies have determined LLZO is stable with Li metal.[52] Li garnet has an electrochemical stability window of about 7 V (vs. Li/Li^+) making it stable with metallic lithium anodes.[53,54] A Li-S battery enabled by SSEs has the theoretical energy density of 2600 Wh/kg whereas a standard commercial battery only has an energy density of ~800 Wh/kg.[37,55]

Li garnet comprises two phases: the tetragonal phase, which exhibits 1 to 2 orders of magnitude lower conductivity, and the cubic phase, known for its higher conductivity.[56–58] The phase of garnet is determined by the sintering temperature, with the cubic phase requiring high temperature sintering.[56] Excessive temperature can lead to its decomposition as lithium vaporizes and leaves the system.[56] In undoped LLZO, the cubic conductive phase forms above 1150°C and breaks down above 1250°C to the lower conductivity phase of $La_2Zr_2O_7$.[56] Al doping of LLZO

from Al_2O_3 crucibles was utilized to stabilize cubic LLZO phase at much lower temperatures than undoped.[59] The addition of low parts of Al^{3+} ions into Li-sites creates extra Li vacancies which helps stabilize the cubic phase.[59] In addition to Al, other dopants have been investigated with goal to further stabilize the cubic phase of LLZO as well as to improve ionic conductivity.[50,60–62] Ca and Nb show promise as dopants for the La-site and Zr-site, respectively, in the form of LLCZN, reducing the sintering temperature while enhancing the ionic conductivity up to 0.8 mS cm^{-2}.[63,64] Ta-doped LLZO has been observed in the cubic phase with temperatures as low as 610°C.[61]

1.2.3 Improving the Interface for $Li_7La_3Zr_2O_{12}$

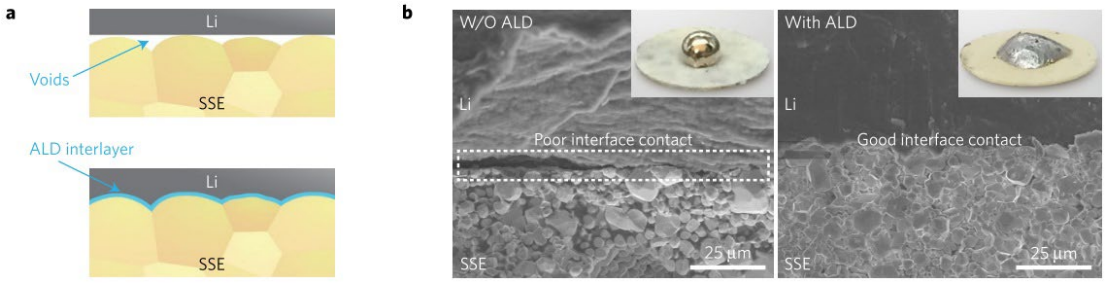

Figure 1.7: a) Schematic of Li metal wetting on LLZO before and after ALD interlayer deposition. b) SEM demonstration LLZO wetting without ALD layer and with ALD layer.[65]

One of the most distinct challenges with the implementation of LLZO as a SSE is the high interfacial impedance between it and Li metal.[66] As discussed previously, one of the main goals of using SSEs is the implementation of Li metal anodes.[1,32] LLZO has exhibits poor wetting with Li metal which means poor interfacial contact resulting in high ASR.[65,67] Applying an ALD coating to the surface improves the Li metal wetting with LLZO as shown in figure 1.7. Without ALD voids

were left in the interface between the LLZO electrolyte and Li metal causing localized high current in the areas of contact.[65] Such poor contact between the anode and electrolyte limits the available surface area for Li^+ transfer. These localized points of high current can be points of weakness in the electrolyte for dendrite growth.[68] The addition of an ALD layer drastically improves the wetting creating more surface area between the Li metal and LLZO eliminating the localized points of high current density.[65,67] The improved Li^+ transfer is reflected in the impedance as shown in figure 1.8 where the resistance decreases by over 20x (3528 Ω·cm^2 to 176 Ω·cm^2).

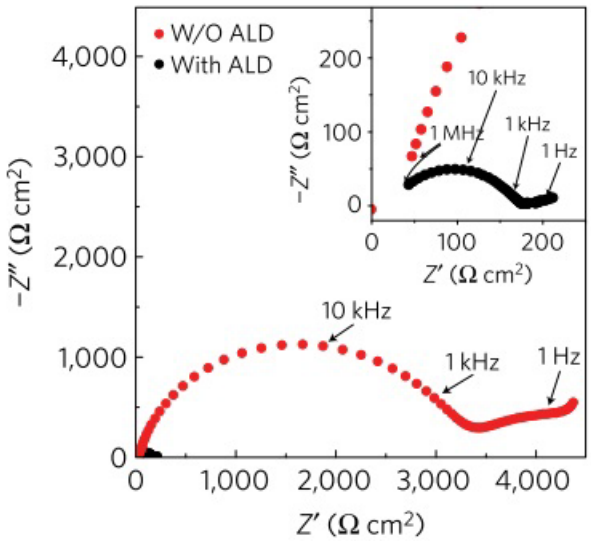

Figure 1.8: EIS measurements of Li-Li symmetric cells with and without Al_2O_3 ALD. The sample with ALD layer has an inlay to highlight its over 20x drop in impedance.[65]

There have been reports of LLZO reacting with H_2O from atmosphere via a substitution reaction as seen in equation 1.1.[61]

$$Li_7La_3Zr_2O_{12} + H_2O \leftrightarrow Li_{7-x}H_xLa_3Zr_2O_{12} + x \cdot LiOH \quad (1.1)$$

This reaction is believed to happen in conjunction with the presence of CO_2 in atmosphere and is reversible with a simple heating above 600°C in a dry atmosphere

where the water is removed from the surface and the Li is reinserted back into the LLZO structure. The LiOH on the surface does not aid Li metal wetting and it can cause difficulty for ALD deposition and is typically removed during LLZO processing.

1.2.4 Improved Cell Performance with Three-Dimensional Structures

Interfaces of LLZO still have higher impedance in full battery cells restricting their ability to be commercialized. ALD has improved Li metal wetting greatly reducing interfacial impedance and mitigating dendrite grown through Li-garnet SSEs,[65–67] while 3D structures created with tape casting-laminating approach (figure 1.9) and freeze casting (figure 1.10) both provide extended surface area to increase Li^+ transfer and electrode utilization.[69–72] 3D Li-garnet frameworks show outstanding cycling in Li symmetric cells with Li-garnet stably cycling at 10 mA/cm^2 for 500 h.,[65,69,73] and recently, a modified Li-garnet trilayer with a mixed ionic electronic conducting (MIEC) garnet in the porous structure achieved over 100 mA/cm^2.[74] 3D Li-garnet structures perform significantly better than all other Li-garnet interface strategies[75,76] and provide at least 40x improvement to electrode/garnet interfacial area when compared with planar structures.[69] Yi et al. with a 3D structure created from freeze-casting and were able to fill 80% to 90% of the pores with NMC622 suggesting that the porous structure shown in figure 1.10 is not open enough to easily infiltrate NMC622.[71] No published data exists on whether NMC particles will infiltrate into the pores of the trilayer structure proposed by Hitz et al.[69] However, the

community generally understands that the typically large particle sizes of NMC (3 to 6 µm) are too large to reliably fit into the random surface porosity of the porous layer.

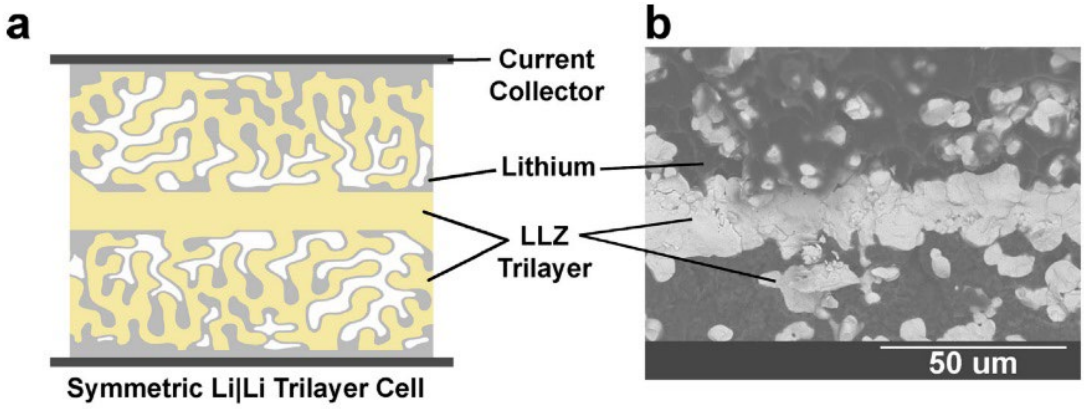

Figure 1.9: a) Schematic of Li-Li symmetric cell built utilizing a tapecast-trilayer LLZO structure. b) SEM cross section of Li-Li symmetric cell built utilizing a trilayer LLZO structure.[69]

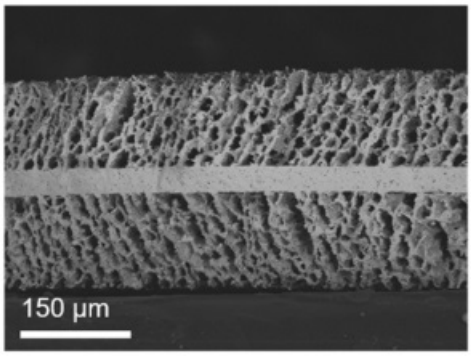

Figure 1.10: Trilayer structure produced by tapecasting and freeze casting Li garnet.[71]

1.2.5 Effects of Microstructure on Conductivity

Tortuosity refers to the measure of the indirectness or convolutedness of a pathway traversed by ions or particles within a medium. Applying tortuosity to LLZO applications, we are considering the diffusion path of Li ions and electrons within the electrodes. Geometric tortuosity, illustrated in figure 1.11a, is defined as the ratio of the diffusion path length to the straight-line distance. A tortuosity of 1 represents the ideal scenario for conduction paths, as indicated by equation 1.2, where $\Delta l = \Delta x$, indicating that the path traveled is the shortest possible.[77]

$$\tau_{geo} = \frac{\Delta l}{\Delta x_{geo}} \tag{1.2}$$

The percolation factor, depicted in figure 1.11b, quantifies the ratio of the connected structure to the isolated structure. The percolation factor is defined as the percentage of the connected phase over the total phase, as depicted in equation 1.3. If all of the phase is connected then the percolation factor is 1.[77]

$$P = \frac{N_{phase,\ connected}}{N_{phase,\ total}} \tag{1.3}$$

The constriction factor, as demonstrated in figure 1.11c, represents the ratio of the minimum cross-sectional area to the maximum cross-sectional area, reflecting bottleneck constriction as shown in equation 1.4.[77–80] A constriction factor of 1 is ideal as that would mean the conduction path across the entire path is uniform in radius and by extension area, so no constriction is occurring.[77]

$$\beta = \frac{r_{min}}{r_{max}} \tag{1.4}$$

While 3D structures improve the cell performance,[69–72] more control over the microstructure is required to optimize conductivity in the form of making conduction paths more direct between electrolyte and current collector.[77] Hamann et al. report that high tortuosity 3D structures or structures with nonlinear conduction paths reduce effective conductance by up to 19.85%.[77] Isolated pores in the LLZO system are also not conducive to a high performance system as isolated pores will have no paths to be infiltrated with electrode. Constriction in 3D structures works similar to the effect of

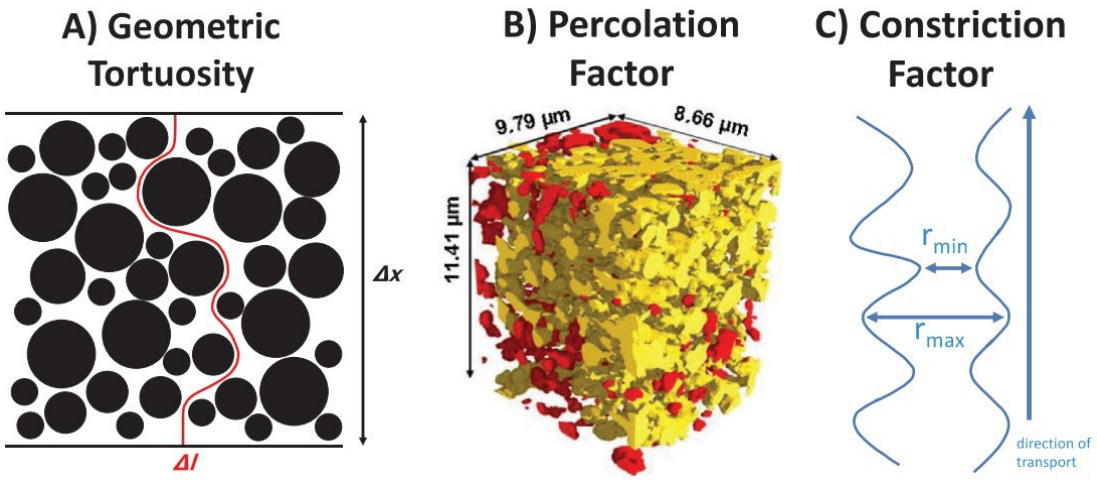

Figure 1.11: Schematics demonstrating a) geometric tortuosity, b) percolation factor, and c) constriction factor.[77–80]

the not ALD coated LLZO with Li metal. As the Li^+ conducts through the electrolyte, it is preferable for the number of bottlenecks to be minimized.[81] Hamann et al. found the constriction factor was the most important factor when it came to reducing conductivity losses due to microstructure.[81]

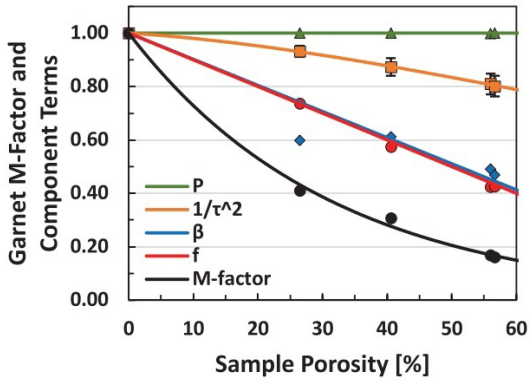

Figure 1.12: Microstructure terms plotted for various porosity LLZO samples ranging from 0% porosity to 56.67% porosity. P is percolation factor, $1/\tau^2$ is the tortuosity component, β is constriction factor, f is the volume fraction, and M-factor is the combined effect on conductance of all of the previous factors.[77]

Combining these factors allows for the determination of the M-factor, as illustrated in equation 1.5. Subsequently, the modified conductivity can be calculated using equation 1.6.

$$M = f * \frac{1}{\tau^2} * P * \beta \tag{1.5}$$

$$\sigma_{effective} = \sigma_{bulk} * M \tag{1.6}$$

1.3 Research Objective: Develop Li Garnet Inks for Direct Ink Writing for Porous Electrolyte Control

Introducing a 3D approach to conventional planar LLZO batteries has significantly enhanced the performance of SSBs. As this technology advances towards commercialization, optimizing performance becomes paramount. This dissertation aims to investigate and showcase the precise control of LLZO microstructure through DIW to further enhance SSB performance.

Transforming our random porous layer into an ordered 3D printed structure has many advantages. First, the porosity on the surface of the porous layers would be more open allowing larger particle cathodes to be more readily infiltrated. Additionally, an ordered 3D printed structure eliminates the possibility for isolated pores minimizing void area in the electrodes. Secondly, the tortuosity of 3D printed structures approaches 1 due to improved control over the structure, allowing for minimized conduction path lengths and ideal conductivity. Finally, 3D printing enables enhanced control over the constriction within each porous region. Hamann et al. identified constriction as the primary limitation in 3D porous SSEs, and through 3D printing, it can be eliminated.[77]

In our previous work, McOwen et al.[82] successfully developed various solid electrolyte inks for DIW type of 3D printing utilizing Li-garnet for Li-cycling. McOwen et al. found that there are two major classifications of inks for 3D printing, conformal and self-supporting.[82] Self-supporting inks offer direct control over 3D structures. However, the factors that make them ideal for DIW are not well understood. Furthermore, the creation of SSBs using 3D printing has yet to be demonstrated. This dissertation will investigate ink properties and establish correlations with DIW quality and battery performance.

Chapter 2: Development of Li Garnet Inks for Direct Ink Writing

2.1 Fundamentals of Direct Ink Writing

2.1.1 Background

McOwen et al.[82] and earlier researched discussed the correlation between viscosity and ink classification (conformal and self-supporting). Conformal inks were classified as having low viscosity and self-supporting inks as high viscosity as shown in figure 2.1. For a purely Newtonian fluid, flowability typically precludes self-supporting capability. Flowing behavior aligns more with conformal ink characteristics, while rigidity and high viscosity are indicative of self-supporting ink behavior. Achieving self-supporting structures relies heavily on higher viscosity. When aiming for self-supporting structures with a Newtonian fluid, extrusion of a nearly solid complex fluid is necessary, but this process is limited by the viscosity that can pass through the narrow opening of the 3D printer nozzle. Hence, it's imperative to consider self-supporting inks from a non-Newtonian fluid perspective. For structures with high aspect ratios, shear thinning behavior is essential, which can be measured from viscosity data. Shear thinning is a non-Newtonian fluid behavior where the viscosity of a fluid decreases as the shear rate increases. In other words, when a shear force is applied to the fluid, causing it to flow, the viscosity decreases, allowing the fluid to flow more easily. However, simple viscosity tests alone do not suffice as they fail to provide comprehensive insights on viscoelastic recovery. While basic viscosity experiments provide extrusion feasibility data, it fails to capture post-

shear thinning ink recovery properties. More in-depth methods of characterizing inks are required for such work.

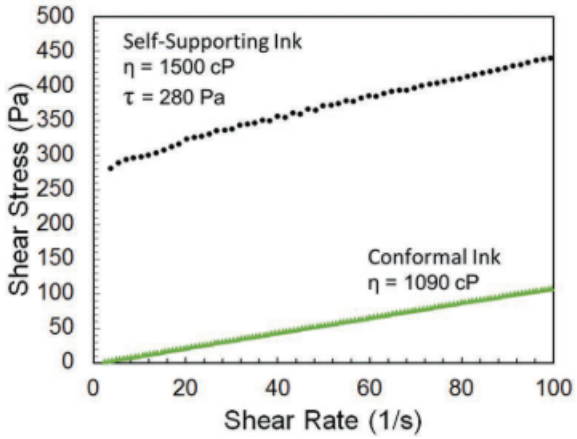

Figure 2.1: The viscosity data for the self-supporting ink was compared with that of a conformal ink exhibiting Newtonian behavior.[82] Viscosity of the self-supporting and conformal inks wer measured at 1500 cP and 1090 cP respectively. The self-supporting ink exhibited a yield stress of 280 Pa, while the conformal ink showed no yield stress.

2.1.2 Direct Ink Writing Concepts and Design Goals

DIW 3D ceramic structures require specific parameters to print high aspect ratio self-supporting structures. The ink must strike a balance; it cannot be excessively viscous, impeding flow through the printer head, nor excessively thin, risking collapse under its own weight. Shear thinning is crucial for DIW, as the ink needs to be stiff enough to support its weight in the final 3D printed product, yet flow easily and consistently during extrusion from the DIW printer head. Developing an ink with shear thinning properties is necessary to achieve these opposing behaviors. It is crucial for the ink to demonstrate shear thinning while also rapidly returning to a high viscosity state, ensuring quick viscoelastic recovery. To create a high-functioning DIW ink, it is essential to achieve a balance among three key factors: 1)

high viscosity under no stress or at rest, 2) flowability under elevated stress suitable for application by the DIW printer, and 3) rapid return to a high viscosity state after stress removal or a quick viscoelastic recovery time.

2.2 Rheology Background

2.2.1 Concepts

To understand the above stated requirements of the ink, the inks rheology must be studied. Achieving an optimal rheological balance is crucial when formulating inks for 3D features. The ink moduli must reach an adequate level to facilitate the formation of freestanding structures.[82] However, DIW printers have limited pressure capabilities, meaning that excessively high moduli or insufficient shear thinning will render the self-supporting ink non-printable.

In the early attempts to characterize the DIW printer inks, viscosity was the only viscosity was the major ink property investigated. McOwen et al. investigated shear stress and a function of shear rate to determine viscosity of the inks.[82] These tests are effective for Newtonian fluids they represent, but as discussed previously, the non-Newtonian shear-thinning behavior is crucial for optimizing and ensuring the long-term success of DIW SSE.[82] As ink viscosity increased, the non-Newtonian nature of the inks became apparent. In figure 2.2, a non-Newtonian ink exhibiting shear thinning is displayed. As the shear rate increases, the shear stress initially reaches a maximum before decreasing, while viscosity concurrently decreases.

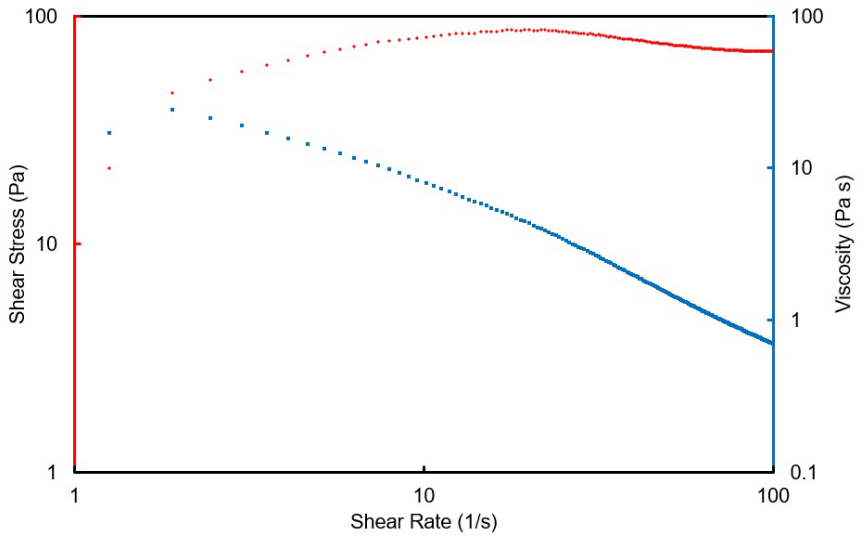

Figure 2.2: Viscosity measurements of a non-Newtonian LLZO ink exhibiting shear thinning. This ink had 68 wt%$_{LLZO}$ loading and 32 wt% organic solvents.

These inks have a much higher solids loading than reported by McOwen et al. leading to much more solid-like behavior.[82] These tests were conducted using continuous rotation, and, akin to other solids, high solid loading inks exhibit plastic deformation earlier under this mode compared to testing via oscillatory rotation. The high-viscosity, viscoelastic nature of the inks necessitates that oscillatory rheology be conducted.[83]

Viscosity is not the most descriptive term for characterizing inks, as discussed previously, because these high solid loading inks exhibit both solid-like and liquid-like characteristics. G^* and δ are much more useful variables when characterizing such inks. G^* is calculated from the shear stress (σ) and shear strain (γ) applied to the ink as shown in equation 2.1.

$$G^* = \frac{\sigma}{\gamma} \tag{2.1}$$

δ is the phase angle representing the lag in the response between σ and γ. This lag in a complex fluid's response means, G^* can be broken down into two components, storage modulus (G') and loss modulus (G'') as seen in equations 2.2 and 2.3.

$$G' = G^* \cos(\delta) \quad (2.2)$$

$$G'' = G^* \sin(\delta) \quad (2.3)$$

When $\delta = 0$, there is no lag in stress response, so $G' = G^*$, and when $\delta = \pi/2$, $G'' = G^*$. Solid-like behavior is often considered represented by G' and liquid-like behavior is represent by G'' of a complex fluid.[83,84] When dividing equations 2.3 by 2.2, we see δ, G', and G'' are related in equation 2.4.

$$\tan(\delta) = \frac{G''}{G'} \quad (2.4)$$

2.2.2 Stress and Time Sweeps

To characterize the inks, two rheology tests are conducted: stress sweeps, time sweeps, and frequency sweeps. During a stress sweep, the ink undergoes a range of stresses from low to high, as suggested by the name of the test. This test provides information on G', G'', flow point, and non-Newtonian behavior. For this test, a starting stress of 10 Pa was selected, which was the chosen initial point for most stress sweep tests. For extremely high viscosity inks, lower stresses may yield noisy data. Therefore, the starting stress is increased to mitigate the noise.

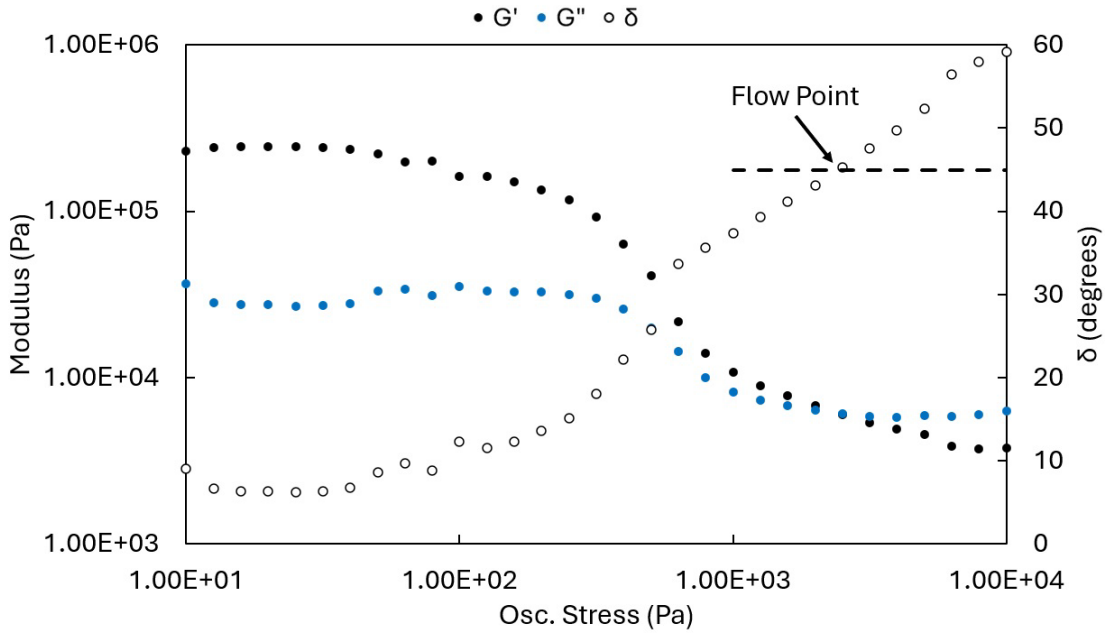

Figure 2.3: LLCZN ink oscillatory stress sweep test. The concept of flow point is demonstrated at where δ is 45° and where G" becomes larger than G′.

Figure 2.3 depicts a stress sweep test conducted on an LLZO ink. Initially, G′ is greater than G", and as stress increases, both G′ and G" decrease. However, G" declines slower with ramping stress, resulting in G" exceeding G′ beyond the flow point, identified as the point where δ reaches 45°. Since both G′ and G" are decreasing with increasing stress, the LLCZN ink system is shear thinning which is the desired property for DIW. At stresses lower than the flow point, G′ is dominant and at stresses higher than the flow point, G" is dominant.

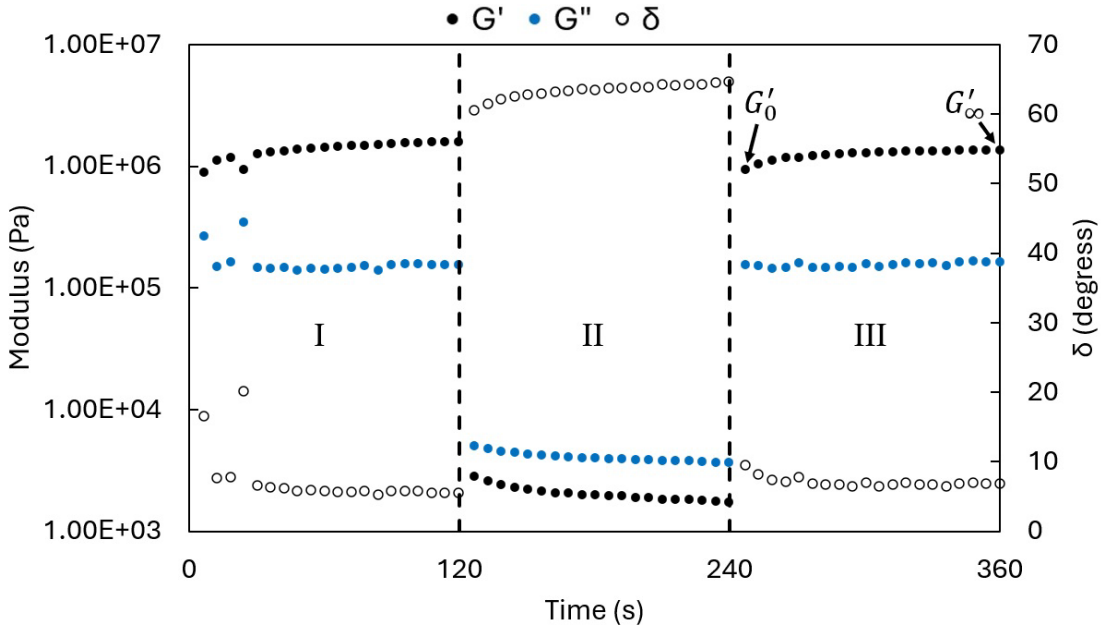

Figure 2.4: LLCZN ink oscillatory time sweep test or 3ITT. Interval I and III are low stress holds below the flow point and interval II is a high stress hold above the flow point.

The second test for inks involves analyzing their viscoelastic recovery, which requires a time sweep test, also known as a Three Interval Time Test (3ITT). An example time sweep test is depicted in Figure 2.4, illustrating the sequence of stress holds from low to high, and back to low stress. Intervals I and II are baseline holds and interval III is where recovery time is determined. If the time sweep test is conducted properly, G′ should be dominant in intervals I and III and G′ should be dominant in interval II. The LLCZN ink in Figure 2.4 exhibits a slight delay in returning to its steady-state condition. To determine the initial modulus value and the approximate steady-state value, G_0' and G_∞' are used, respectively. τ indicates the time required for the ink to recover a certain percentage back to G_∞' from G_0'. Due to the high solid loading in the inks, the moduli from interval III often does not recover back to the moduli in interval I. This occurs due to the plastic deformation induced by the

high stresses applied to the inks during the sweep tests. Both the stress sweep and time sweep tests are destructive, and the ink properties never fully recover to their original moduli.

The last test, the frequency sweep, holds fixes the stress experienced by the ink, but gradually increases the frequency of the stress experienced. This test looks at how inks behave at different time lengths. These types of tests could give insights on how to adjust applied pressure to the inks. Ideally, the time scale should change minimally in G′ and G″ and overall non-Newtonian character should not change.

For each of these tests, the ink is loaded underneath the geometry completely to ensure good measurements as the loss of a total filling will lead to inaccuracies for the measurements. Each test was performed in atmosphere with air cooling to the rheometer to prevent overheating to the mechanism. All of our rheology measurements were done with a TA Instruments AR2000 rheometer or a ThermoScientific Haake Mars iQ rheometer.

2.2.3 Viscoelastic Recovery

To underscore the need for comprehensive characterization, two similar inks are shown in figure 2.5. In figures 2.5a and 2.5b, stress sweep tests reveal comparable initial moduli (5410 Pa for ink A and 4275 Pa for ink B) and similar trends as oscillatory stress increases. However, upon closer examination of their time sweep tests, distinct differences emerge. Ink A exhibits a sharper modulus drop, accompanied by a rapid τ_{50} at 15 s (figure 2.5c), whereas ink B displays a more gradual modulus loss, with a slower τ_{50} at 39 s (figure 2.5d). The morphology

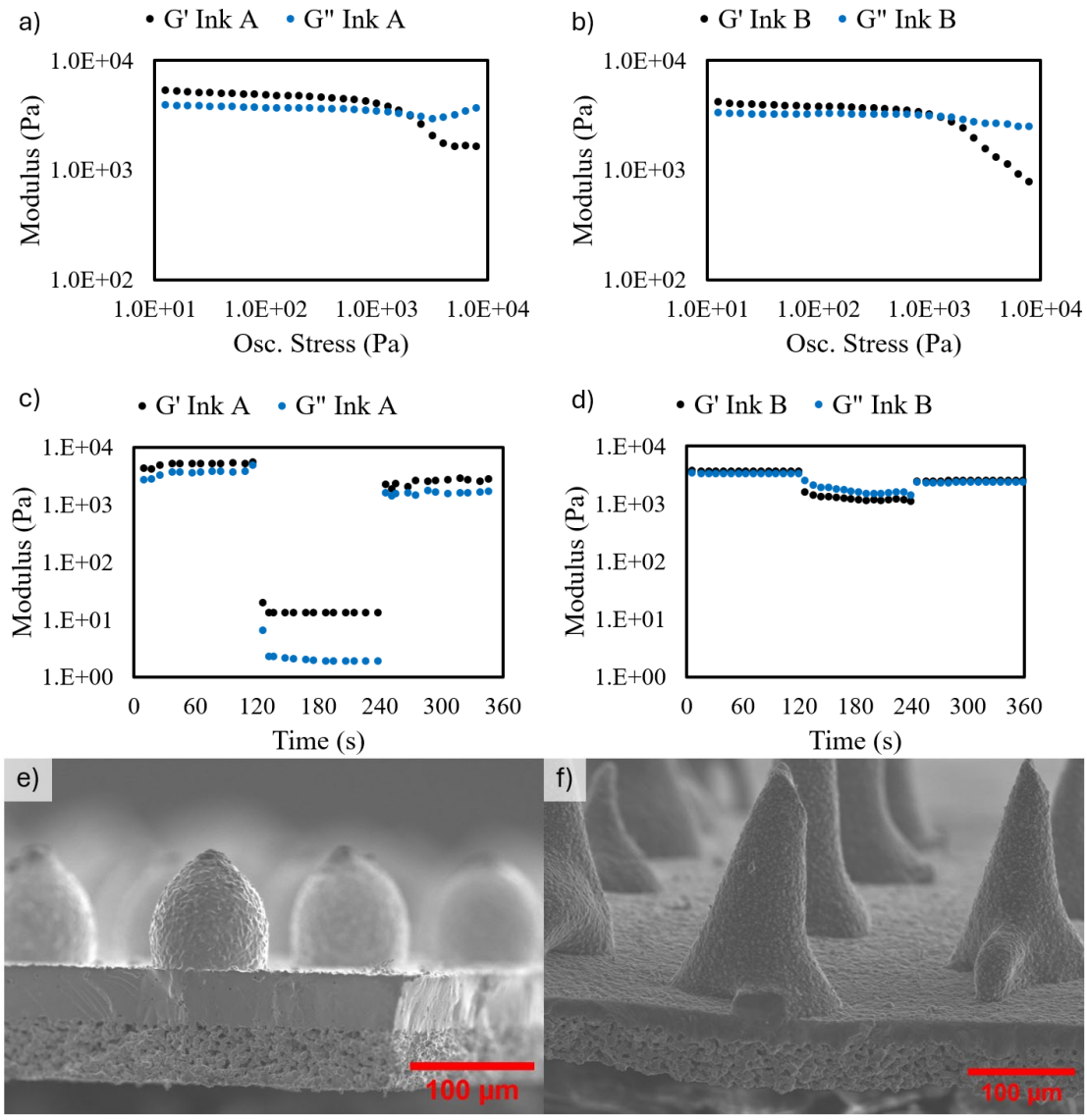

Figure 2.5: Rheological data for two inks and their corresponding 3D printed structures. a-b) Stress sweep results of ink A and ink B, respectively. c-d) Time sweep resultf of ink A and ink B, respectively. e-f) SEM cross-section images depicting column structures printed using ink A and ink B, respectively.

analysis in figure 2.5e reveals that ink A assumes a rounded, conformal appearance, likely due to its significant modulus reduction under high stress during the time sweep test. Conversely, ink B (figure 2.5f) exhibits a slightly more supportive structure and minimal beading compared to ink A, attributable to its more consistent modulus distribution throughout the time sweep test, despite a slower τ_{50}. These

findings underscore the inadequacy of stress sweep tests alone for characterizing these complex inks.

2.3 Rheology Testing

2.3.1 Oscillatory Stress Sweeps

Conformal and self-supporting inks were defined in previous sections and this section is apply the ideas and methods to characterize the inks. The first step to characterizing the inks was to conduct an oscillatory stress sweep test. It is crucial to characterize the changes in G' and G'' with increasing stress and identify the point at which they intersect (flow point) from the stress sweep. This data provides valuable insights for subsequent time sweep tests aimed at identifying thixotropic behavior. Each ink was subjected to oscillatory rheology testing at a frequency of 10 rad/s and shear stress ranging from 10 Pa to 1000 Pa. Shear stresses below 10 Pa often resulted in significant experimental noise. Although the AR2000 rheometer could measure up to 10 kPa, some inks exhibited noise levels exceeding 1 kPa, particularly when transitioning to a flowing state, due to ink ejection from underneath the geometry.

The experiments involved testing over one hundred inks, resulting in significant variations. These variations were initially challenging to control and not immediately intuitive, but we will discuss the hypotheses and findings later.

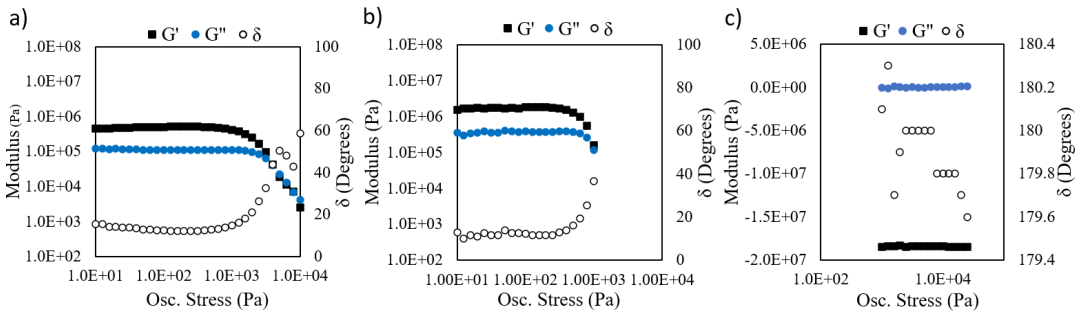

Figure 2.6: Oscillatory stress-sweep rheology tests of three different inks; a) ink 1 – conformal ink, b) ink 2 – semi self-supporting ink, and c) of ink 3 – conformal ink. G′ and G" of ink 3 are inaccurate due to exceeding the maximum measurable modulus of the rheometer.

Figure 2.6 depicts stress sweeps of three ink types: a) conformal, b) semi self-supporting, and c) self-supporting. These inks are the best examples that had rheology measured and were 3D printed in future chapters. G′ and G" are related to viscosity and previous work[82] classified higher viscosity inks as more self-supporting. From the figures 2.6a-c, one can see that as both G′ and G" increase, so did the classification from conformal to self-supporting.

When analyzing the resulting of figure 2.6, the important figures of merit are flow point which is characterized by $G' = G"$ or when $tan(\delta) = 1$ and yield stress which is characterized by the inks transition on a stress sweep from the linear region to its non-linear region.

Figure 2.6a presents the stress-controlled sweep of our first ink which started yielding around 800 Pa of oscillatory stress and flowing around 4 kPa with initial G' of 449 kPa and initial $G"$ of 124 kPa.

Figure 2.6b depicts the stress-controlled sweep of our next ink which started yielding around 300 Pa of oscillatory stress and the flow point is close to 1 kPa.

Comparing this stress sweep to figure 2.6a, we observe higher G' and $G^{"}$ (4.54 MPa and 3.75 MPa respectively) for this ink.

Figure 2.6c presents the stress-controlled sweep of our last ink. The data collected from the AR2000 rheometer was reading a negative G' and $G^{"}$ which does not have a physical meaning suggesting that the capabilities of the machine were exceeded. The G' and $G^{"}$ values would be significantly higher than those observed from the previous inks.

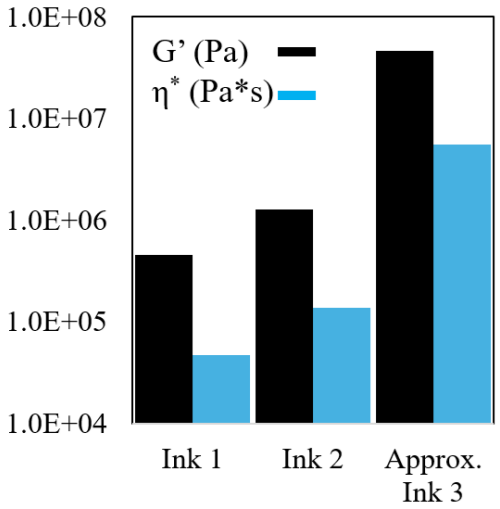

Figure 2.7: Initial G' and complex viscosity of inks 1, 2, and 3. Both G' and η^* of ink 3 is approximated from the time sweep $G^{"}$ and assuming initial δ is 10°.

As seen from figure 2.7 there is a trend from ink 1 to ink 3 as they are characterized with more self-supporting behavior, the inks G' and η^* both increase which is also in agreement with the previous study only analyzing viscosity.

2.3.2 Oscillatory Time Sweeps

Once the data from the aforementioned three inks was collected, their time responses were analyzed using time sweep tests. Similar to the stress sweep tests, the

testing frequency was maintained at 10 rad/s; however, the testing stresses were determined based on the stress sweeps conducted earlier.

As previously discussed, two stresses are analyzed for stress sweep tests: high and low. The high stress was set to a stress level beyond the flow point of the ink. For consistency, the high stress parameter was set as close to 200% strain as possible, as 200% strain was consistently observed in the high stress region during the stress sweeps. The low stress was set anywhere before yielding, preferably as low as possible where the measurable G' and G'' were not noisy. This value was kept as close to 1% strain as possible. Time sweep tests consist of three intervals, which can be simplistically referred to as Intervals I, II, and III. Intervals I and III are set to the fixed low stress value and interval II is set to the fixed high stress value. Interval I serves as a baseline measurement under low stress, interval II represents the ink past yielding and flowing at high stress, and interval III characterizes the ink's time dependent recovery in G' and G''. For inks which have a more noticeable viscoelastic response, there will be an arc in interval III as the G' and G'' recover back to steady state. G_0 is denoted the initial value for modulus immediately after relieving the high stress of interval II. G_∞ stands for the modulus steady state in interval III. The recovery time (τ) can then be derived from the interval III as the amount of time needed to recover to G_∞.[85,86]

Figure 2.8 illustrates stress sweeps of three ink types: a) conformal, b) semi self-supporting, and c) self-supporting. These inks are the best examples that had rheology measured and were 3D printed in future chapters.

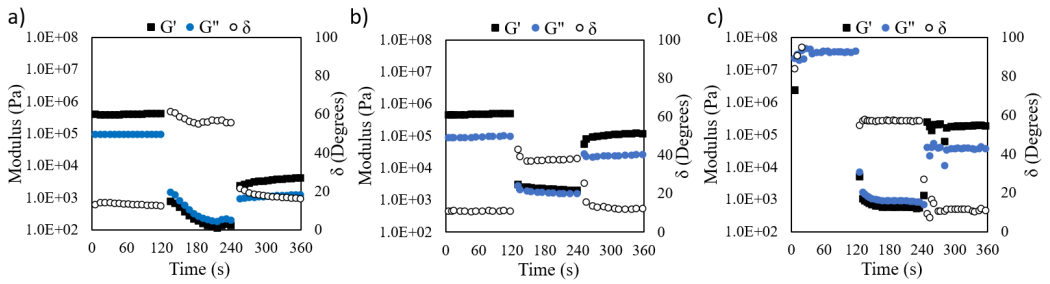

Figure 2.8: Oscillatory time-sweep rheology tests of three different inks; a) ink 1 – conformal ink, b) ink 2 – semi self-supporting ink, and c) of ink 3 – conformal ink. G′ and G" of ink 3 are inaccurate due to exceeding the maximum measurable modulus of the rheometer.

Figure 2.8a presents the time-controlled 3ITT of the first ink shown in figure 2.6a. The G' and $G"$ of the conformal ink recovered 50% of it G_∞ (τ_{50}) after 47.2s which is not quick enough to maintain the aspect ratios of the prints after extrusion. The combination of low moduli and high recovery time characterizes this ink as conformal.

Figure 2.8b presents the time-controlled sweep of ink shown in figure 2.6b. In contrast to the first ink, this ink exhibits a faster convergence to G_∞, 15.1 s of recovery to 50% of G'_∞ (τ'_{50}) and 66.4 s of recovery to 50% of $G"_\infty$ ($\tau"_{50}$). While the $\tau"_{50}$ is high, the overall change to $G"$ in interval III is only 2.72 kPa compared to the delta in G' in interval which is 62.4 kPa. Since the $G"_0$ and $G"_\infty$ are close in value, we suspect the real value of $\tau"_{50}$ is closer to τ'_{50}. The higher initial moduli and lower recovery time makes this ink self-supporting, but we will discuss our most self-supporting ink next.

Figure 2.8c depicts the time-controlled sweep of the ink shown in figure 2.6c which experienced the rheometer error as previously discussed. The G' in interval I was reading as negative indicating the similar error from the stress sweep test, but the $G"$ was giving a positive valve indicating that the real $G"$ value is close to 29.5 MPa.

Under the stress of interval II, G' and $G^{"}$ dropped in a measurable range indicating shear thinning behavior despite the ink's high initial moduli. Upon returning to interval III, both moduli remained measurable, revealing a both τ'_{50} and $\tau^{"}_{50}$ are less than 5.7 s. This ink at a very low time scale reached well over 50% to G'_{∞} and $G^{"}_{\infty}$, so this ink has a near instantaneous recovery with extremely high G' and $G^{"}$ classifying it as our most effective self-supporting ink.

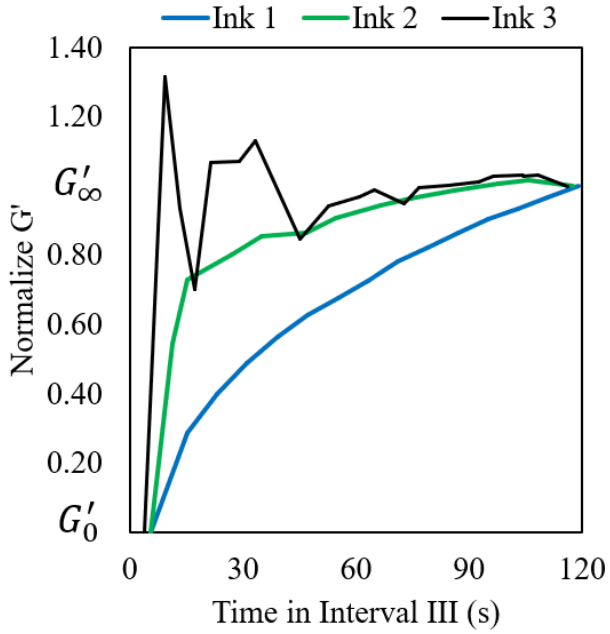

Figure 2.9: Normalized data from interval III of the 3 ink samples from the time sweep test in figure 2.8. Data is normalized using each of the inks G'_0 as 0 and G'_{∞} as 1.

From figure 2.9, there is noticeable quick response from the more self-supporting inks. The sharpness of the recovery arc increases as inks 1 to 3 increase in self-supporting behavior.

Simple viscosity tests are insufficient for classification, highlighting the importance of time sweep rheology for obtaining comprehensive data on an ink's conformal or self-supporting properties.

2.3.3 Oscillatory Frequency Sweeps

The last test completed were frequency tests. The frequency response to two example inks are shown in figure 2.10. The conformal ink from figure 2.10a saw some more interesting behavior from the frequency sweep where δ actually transitioned over 45° meaning $G^{"}$ briefly was dominating indicating flowing behavior, but overall the δ variation was not much more than 5 degrees throughout the entire test. The overall δ was quite high for this ink already indicating much more liquid-like behavior, which is indicative of its conformal classification.

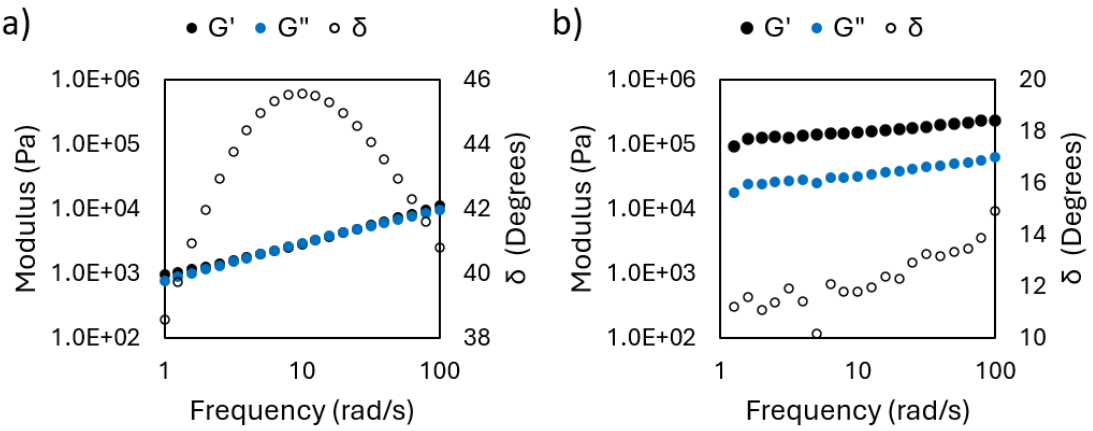

Figure 2.10: Frequency sweeps of two Li-garnet inks: a) low-modulus, conformal ink and b) high-modulus, semi self-supporting inks.

The much more self-supporting ink is shown in figure 2.10b. As indicated by the much lower δ, this ink naturally at all tested frequencies had much more solid-like behavior as G' is dominating throughout the entire test. For this reason, the δ is much lower than that of the conformal ink. Once again, this ink had fluctuation about 5° across the entire frequency sweep. For the remainer of this work, only inks with consistent behavior across the frequency sweep are targeted. This does coincidently correspond to high self-supporting inks.

2.4 Ink Composition

The early ink recipes were developed very similarly to McOwen et al. utilizing LLZO particles as the material of interest for DIW, ESL 441 as our commercial binder/plasticizer system, and an ethanol carrier solvent to aid with mixing.[82] ESL 441's exact formula is proprietary information, but it is understood to be a Texanol-based ink vehicle with alpha-terpineol, ethyl-cellulose, and other minor additives.

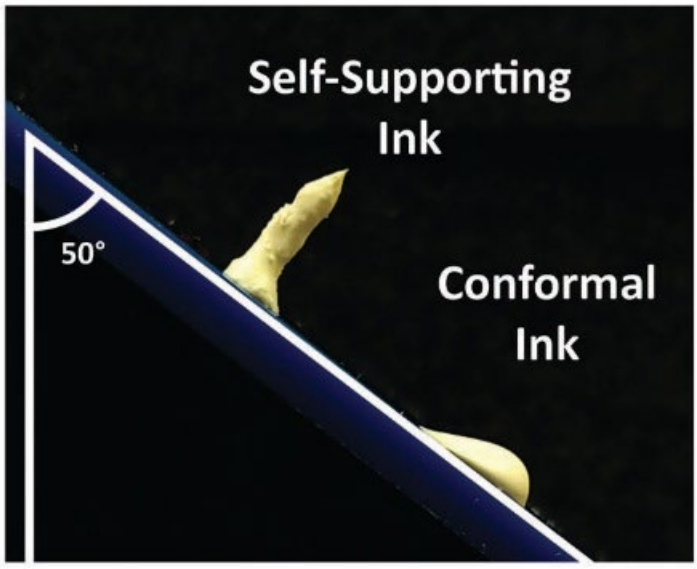

Figure 2.11: Photograph of two inks tilted on a 50° stage to demonstrate the difference between self-supporting and conformal inks.[82]

McOwen et al. classified DIW inks into two categories: conformal or self-supporting, as illustrated in figure 2.11. Conformal inks exhibit more liquid-like characteristics and cannot support their own weight to print high aspect ratio structures, whereas self-supporting inks possess more solid-like characteristics and are preferable for printing high aspect ratio structures. In the original formula, increasing LLZO loading would skew the inks towards self-supporting and increasing

ESL 441 and/or ethanol content would push the inks towards conformal characteristics as shown in figure 2.12. ESL 441 was discontinued as an ink vehicles product around 2020, so inks slowly transitioned to a similar ink composition containing Texanol, alpha-terpineol, ethyl-cellulose, and ethanol as the main organic components. Ethyl cellulose, naturally a solid, is dissolved in alpha-terpineol under heat at 180°C. All inks in this dissertation will be reported with the ESL441 replacement of ethyl cellulose with Texanol, alpha-terpineol, and ethyl cellulose.

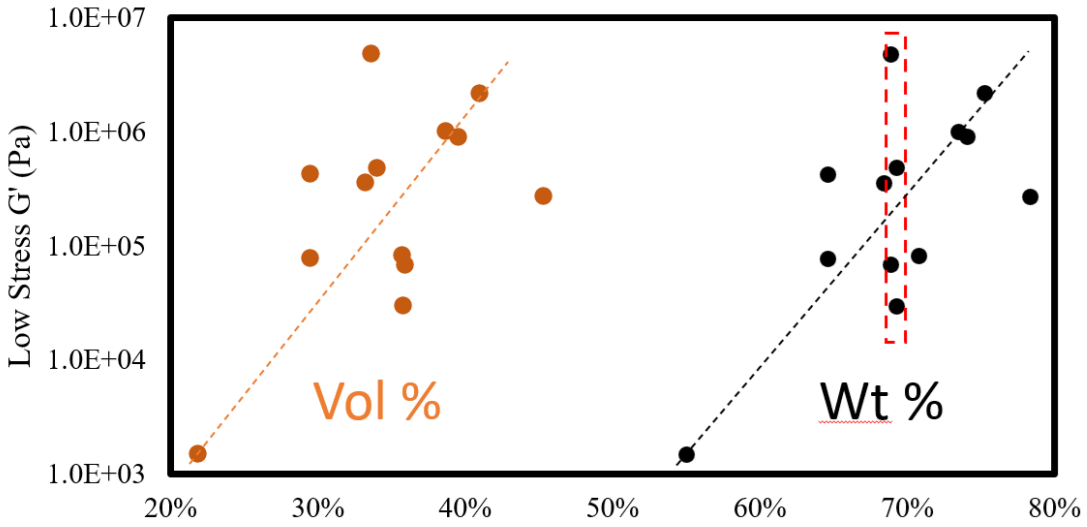

Figure 2.12: Scatter plot of several LLCZN inks with various LLCZN wt% (right). G′ increases as LLCZN wt% increases. Vol % of the LLCZN powder is also plotted (left).

As ink development progressed, it was clear that LLCZN and ESL 441 would not be enough to tune the rheological properties to the degree what was necessary to create self-supporting inks necessary for high aspect ratio structures. Ethyl-cellulose in DIW has been used as a binder/rheology tuner.[87,88] The addition of ethyl-cellulose to the LLCZN ink system allows the inks to have lower τ and higher moduli.

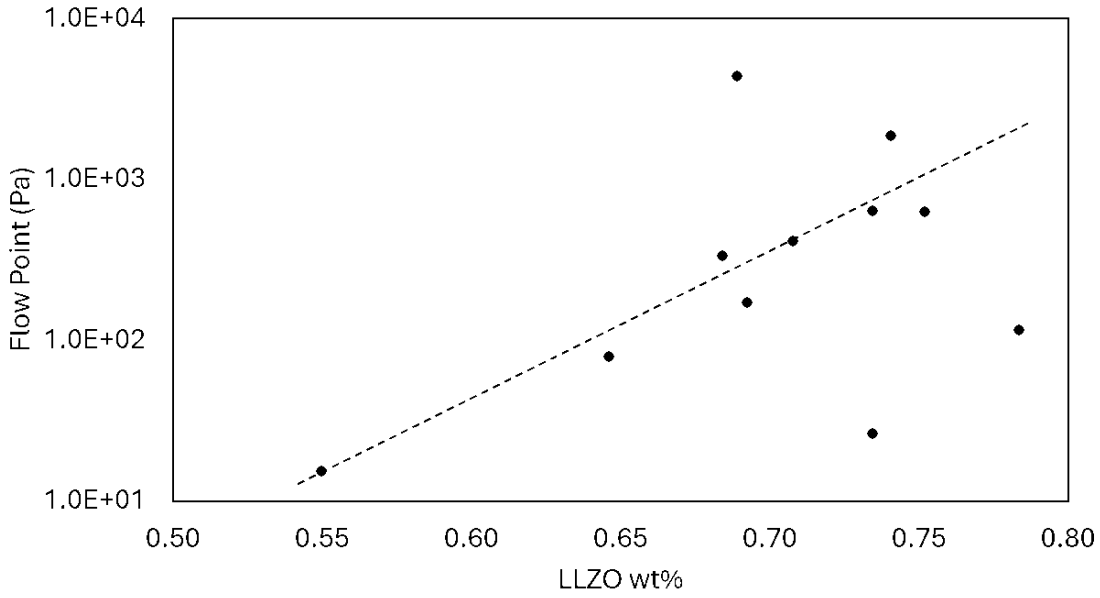

Figure 2.13: Scatter plot of several LLCZN inks with various LLCZN wt%. τ increases as LLCZN wt% increases.

LLCZN loading influences various physical properties of the inks, including the flow point. Figure 2.13 demonstrates that as LLCZN loading increases, the amount of oscillatory stress needed to exceed the ink's flow point also increases. This aligns intuitively with the conventional understanding that as LLCZN weight percentage rises, the behavior becomes more akin to that of a solid and the τ recovers quicker as a result. The nScrypt 3Dn-300 printer which is used for 3D printing can apply a pressure up to 70 psi which is equivalent to $4.8 \cdot 10^5$ Pa. Even considering a potential loss in pressure of over an order of magnitude due to friction within the system, the flow point should still be reached for each of the samples.

2.5 Particle Size and Ink Rheology

From figures 2.12 and 2.13, there is clearly not an exact correlation between LLCZN wt%, low stress G′, and τ. In figure 2.12, there are 4 samples within 0.3 wt%

of 69 wt%. There is a very clear discrepancy between each of these inks low stress G′. Upon closer examination of these sample inputs (Texanol, alpha-terpineol, and ethyl cellulose), no other clear trends driving rheological behavior are evident. This suggests that there is something going on outside of the direct controls. First analyzed was aging effects which will be further discussed in the following section. Aging was observed on 24-hour timescales, but differentiation between the inks persisted even among similarly aged samples, indicating that aging alone did not resolve the discrepancies in the inks.

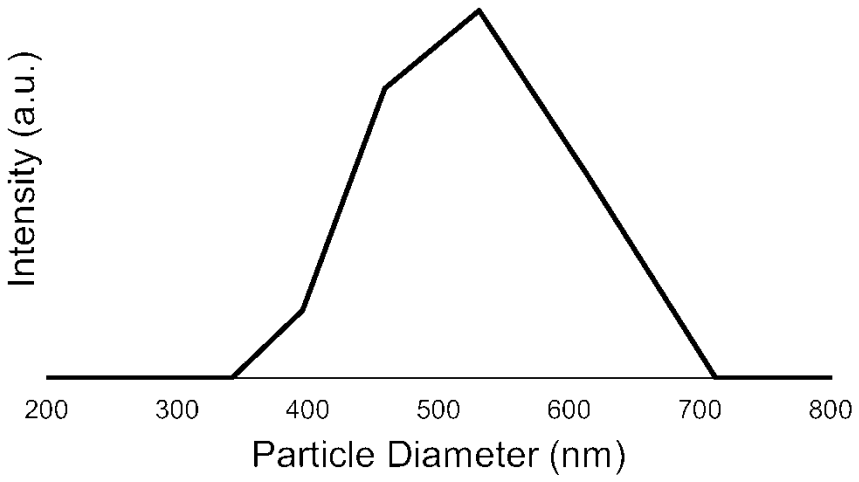

Figure 2.14: Particle size in diameter of LLCZN powder supplied by Trans-Tech.

The particle size of the powder obtained from Trans-Tech (a subsidiary of Skyworks), which was used for most of the rheology work in this thesis, was examined. The powder exhibited a wide range of particle sizes, as depicted in figure 2.14, ranging from 350 nm to 700 nm. Previously, it was assumed that the variation in particle size within each ink sample extracted from the container would not significantly impact the rheological data. In figure 2.6, there are 4 inks 69±0.3

wt%$_{LLCZN}$. These inks were diluted down back into a suitable state for DLS measurements, and these 4 inks increase in modulus with increasing particle size as seen in figure 2.15. Additionally milling of the Trans-Tech powder was able to reduce the particle size marginally, but the ball mill method is unable to drastically reduce the particle size or narrow the distribution as seen in figure 2.16. Further methods will be necessary to make more uniform particle size distributions.

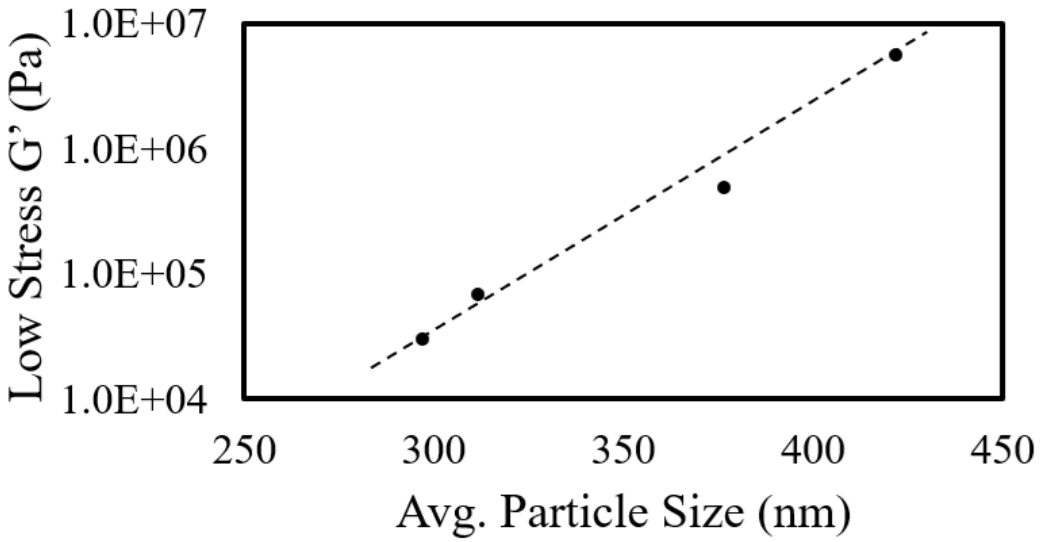

Figure 2.15: Plot of ink compositions 69±0.3 wt%$_{LLCZN}$ with differing average particles size measured by DLS. Each of these inks low stress G' as measured with a oscillatory stress sweep.

Inks which are complex fluids with a very high solid loading can be represented as stacked loose solid layers. Increased ink viscosity requires more force to slide one layer over another, similar to how friction acts between solid sheets. The observed direct correlation between G' and particle size in the inks is hypothesized to stem from larger particles requiring greater force to move past each other, leading to higher G'. A probable correlation exists between increases in surface area of solid powders in suspension and modulus; however, this correlation was not observed with

the particle sizes used in these experiments. It would likely only be discernible at much smaller particle sizes.

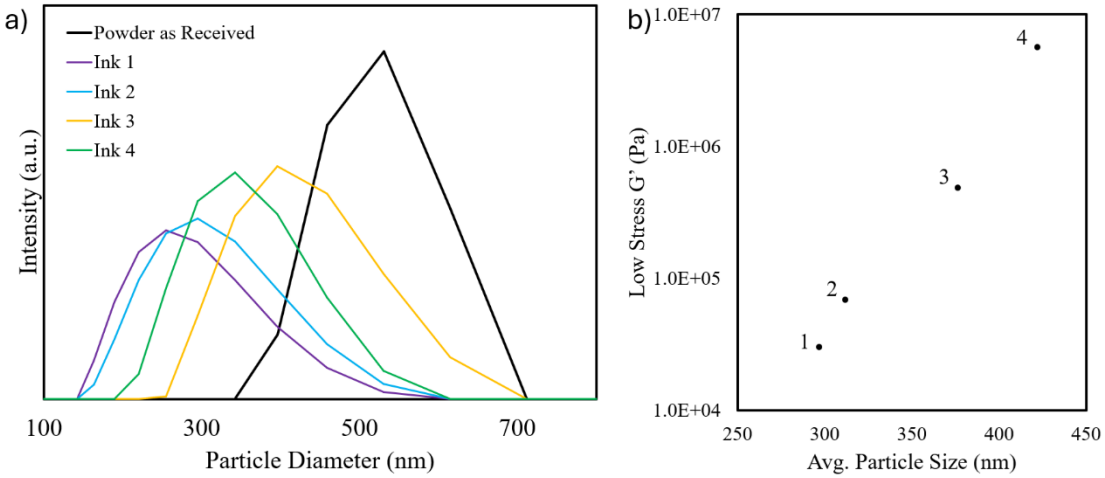

Figure 2.16: a) Particle size distributions from the inks in figure 2.15. b) G' plotted against average particle size data from figure 2.15 labeled for reference. LLZO powder in inks 1 and 2 were milled for 2 to 3 additional weeks where as LLZO ink inks 3 and 4 were only milled for 1 additional week.

2.6 Aging Effects

Preliminary studies show that inks have a natural increase of modulus value with time as seen in figure 2.17. The predominant theory is that this increase of modulus is caused by the evaporation of solvents from the ink with time. During ink making, ethanol is predominantly removed as ethanol does not provide any desirable ink properties in the final ink product and is only useful for homogeneous mixing. The standard ink formulations usually utilize less than 5% ethanol weight content as higher ethanol content leads to more conformal inks.

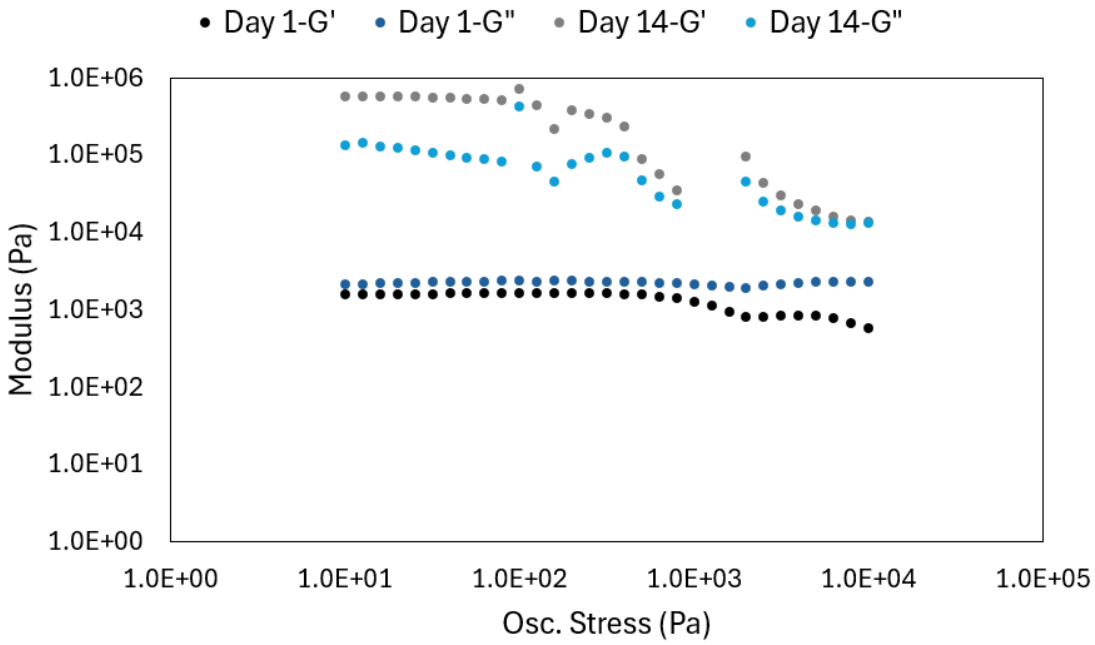

Figure 2.17: Oscillatory stress sweep of an ink after 14 days compared to its initial stress sweep. Original ink was $G^{"}$ dominant, but after two weeks the ink became G' dominant and increased modulus by over 2 orders of magnitude. A slight slip happened at round 1000 Pa stress for the 14-day sample which caused a slight deviation in the high stress measurements.

2.7 Tuning Ink Rheology for Direct Ink Writing

After extensive studies to expand the knowledge about direct ink writing inks, the classification between conformal and self-supporting inks has been made. Rheology including stress- and time- sweeps provide much needed information about ink morphology that simple stress strain rate tests cannot provide.

Elevated values of G' and $G^{"}$ are crucial for high self-supporting inks, consistent with prior research emphasizing the significance of higher viscosity for achieving self-supporting behavior. However, this represents only one aspect of the equation. The recovery of an ink after stress is also crucial for ensuring the quality of 3D printing. In our three sample inks, it is evident that not only the initial moduli of

the inks contribute to their classification, but also their recovery time after stress is significant.

Increased Li-garnet loading had a clear trend toward increasing G', G'', and flow point. Li-garnet particles size also had a noticeable trend effecting G' and G". The addition of ESL441 appeared to decrease τ; however, ESL441 was discontinued in late 2020, and a replacement consisting of texanol and ethyl-cellulose was utilized for the remainder of the 3D printing process.

To produce conformal inks, solid loading or Li-garnet particle size should be reduced, while the opposite approach is needed to achieve self-supporting inks. These principles in DIW ink formulation were applied to DIW Li-garnet for battery applications.

2.8 Conclusions

In this chapter, the rheological properties of DIW inks (storage modulus, loss modulus, and recovery time) of 3D printed Li-garnet inks were studied. The results indicate the following:

(1) Stress-strain plots are insufficient for characterizing complex inks for DIW. Stress sweep and time sweep tests are suitable tools for characterizing an ink's changes to physical properties with respect to applied stress and viscoelastic recovery.

(2) Self-supporting inks have high G', high G'', and low τ. High solid loading and large particle size for Li-garnet improves the rheological properties for

self-supporting inks. Such rheological properties can enable high aspect ratio structures.

(3) Conformal inks have lower G', lower $G^{"}$, and higher τ compared to self-supporting inks. While purely conformal inks are undesirable for more DIW applications, balances will need to be achieved to optimize certain structures.

Chapter 3: Direct Ink Writing $Li_7La_3Zr_2O_{12}$ Columns

3.1 Implementing NMC into 3D Structures

3.1.1 Li-NMC Solid State Batteries

NMC has been a popular cathode choice for Li-ion batteries due to its high specific energy density and stability.[89–91] Higher Ni content increases the capacity of NMC at the cost of lower thermal stability.[92–94] With commercial organic electrolytes, this lower thermal stability comes with the risk thermal runaway events leading to devastating battery fires.[95,96] Carbonate based electrolytes such as DMC are extremely flammable and have cause a large number of battery fires.[19–25,97–99] Naturally, the implementation of a non-flammable electrolyte would drastically reduce the concerns of battery fires.

Li-NMC batteries have been tested utilizing a Li-garnet separator and electrolyte. High NMC loading (32 mg/cm^2) on a planar Li-garnet geometry resulting in high energy density (330 Wh/kg) batteries has been demonstrated.[100] There has been very little literature demonstrating good NMC infiltration into Li-garnet porous structure and the only reported success was utilizing freeze casting.[71,101]

3.1.2 Evolution of Li-Garnet 3D Structures

Planar Li-garnet electrolyte structures have shown promising results in Li-NMC batteries.[100] Nonetheless, their geometry limit cathode loading and rate capability due to low surface area. Therefore, porous Li-garnet scaffolds have been introduced to increase the cathode surface area.[77] The porous Li-garnet scaffolds facilitates higher cathode loading by establishing ionic conductive pathways

throughout the cathode. This allows for the utilization of thicker NMC cathodes as they create additional surface area for Li^+ conduction between the Li-garnet and the NMC cathode. However, porous Li-garnet scaffolds, while enhancing battery cell performance, present two primary issues: 1) the random distribution of pores leads to tortuous and constrictive pathways, which adversely affect cell conductance, and 2) the pore sizes within the porous Li-garnet scaffolds are too small to accommodate the infiltration of relatively large NMC cathode particles (3 – 6 μm). To address these challenges, the freeze casting technique was developed to align the pores within a porous Li-garnet layer.[71,101] This structure has lower tortuosity and NMC is more easily infiltrated into it. Because the pores are better aligned (lower tortuosity), creating more direct paths to the Li-garnet separator, it is possible to achieve 80 to 90% NMC pore filling.[71,101] While this is a significant improvement, there is still 10 to 20% wasted space. Therefore, we propose constructing a precisely controlled structure using DIW 3D printing. This method enables precise control of the pore structure, eliminating conductance losses due to tortuosity and constriction, which will enhance battery performance. The best structure for low tortuosity, low constriction, and high porosity is the column structure. The proposed final full cell design is shown in figure 3.1.

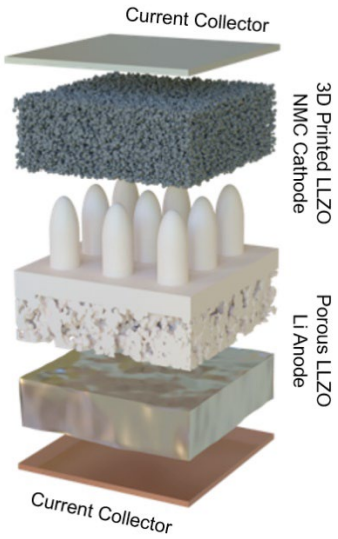

Figure 3.1: 3D schematic of our NMC622-Li full cell with an electrolyte scaffold made through direct ink writing. Self-supporting columns are printed on the dense side of a bilayer substrate. Lithium metal is infiltrated on the random porous side and NMC622 with carbon black infiltrated on the 3D printed side.[102]

3.2 Substrate Design

3.2.1 Tape Casting Li-Garnet Bilayers

To start developing our structure in figure 3.1, the substrate has to be eligible as a printing substrate. Since the bilayer and the DIW structure are the same material, they can be sintered in the same step, so the development of a flat substrate for the ink to print on is paramount.

The bilayers consist of two distinct components: 1) the porous tape, which serves as the medium for ionic conduction within the Li metal anode, and 2) the dense tape, which acts as the Li-ion conducting separator. LLCZN powder was obtained from Trans-Tech (a subsidiary of Skyworks). Using these powders, two tapes were cast: a dense tape with particle sizes ranging from 300 to 500 nm and a porous tape for use as an anode (particle size >1 μm) with PMMA pore former (15 μm diameter).

Each of the tapes were made in accordance to previous work with a BBP and PVB binder-plasticizer system.[69] The smaller particle sizes in the dense tape aid in densification, while the larger LLCZN particle sizes and pore former in the porous tape contribute to a more porous 3D structure, therefore increasing the interfacial area between the anode and electrolyte. To form the bilayer substrate, the two tapes were laminated together at 82°C under 2 metric tons of applied pressure. The tapes were laminated to achieve dense layers approximately 40 to 80 μm thick. The thickness of the dense layer is crucial, as overly thin samples become fragile and challenging to handle after sintering, while excessively thick layers adversely affect cell performance.

The LLCZN powders were characterized by a Bruker D8 X-ray diffractometer and the particle size distribution is the same as the LLCZN in chapter 2 in figure 2.13.

3.2.2 Laser Cutting for Increasing Sample Throughput

Preparing one sample at a time is highly inefficient. To enhance the throughput and consistency of this project, larger-than-necessary bilayers were prepared and then perforated into smaller pieces, each approximately 1 cm^2 in size. The bilayers prepared for sintering were sized 4 cm by 4 cm. Ensuring flatness during sintering poses challenges, leading to curling or warping along sample edges. To mitigate this, the edges of the 4 cm by 4 cm samples stabilize the internal Li-garnet. Consequently, each 4 cm by 4 cm sample comprises nine 1.1 cm by 1.1 cm pieces, as depicted in figure 3.2. This configuration provides space for curling along the edges

of all nine samples without compromising their flatness. As all samples remain in contact with each other, they collectively maintain each other's flatness.

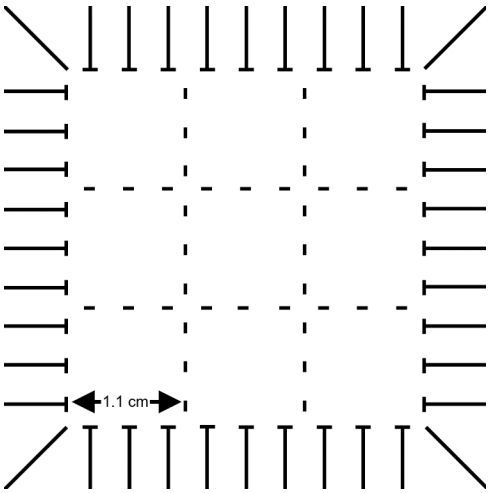

Figure 3.2: Laser cutting profile used for laser cutting the 4 cm by 4 cm LLCZN tape samples. Individual squares are 1.1 cm by 1.1 cm. The pattern is slightly larger than 4 cm by 4 cm to ensure proper cutting to the edges of the sample.

The separation between the perforation cuts varies depending on the sintering process. The cuts must be large enough to create weakness in the sample, causing it to break preferentially along the perforated edges, yet small enough to prevent separation during sintering which will lead to curling or warping.

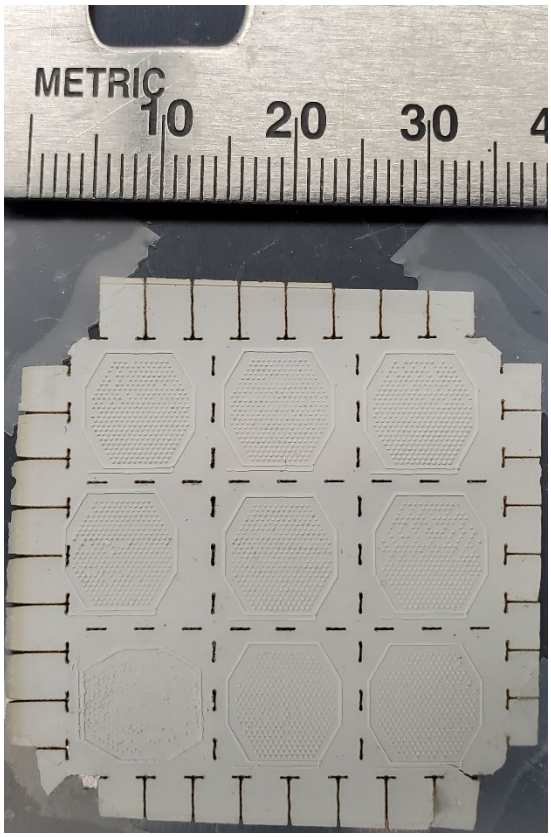

Figure 3.3: Nine 3D-printed column samples were produced on a laser-perforated sample. The entire sample measures 4 cm by 4 cm, with each internal sample measuring 1.1 cm by 1.1 cm. The sample is taped to the plate below to prevent sliding during the 3D printing process.

3.3 Direct Ink Writing

3.3.1 Direct Ink Writing Controls for Column Printing

The 3D printing process involves several direct controls, including tip size, extrusion pressure, valve rod position, valve rod speed, extrusion distance, and vertical speed. Tip size determines the diameter of the extruded ink stream, resulting in a column of equal diameter upon extrusion. As the ink stream contacts the substrate, the excess ink widens the structure, potentially increasing the diameter of the resulting column.

The operator can control pressure in DIW, which, along with another parameter, determines the extrusion rate of the ink. Higher pressure results in a faster extrusion rate. The n-Scrypt printer we use can apply a maximum pressure of 70 psi or 483 kPa.

We can control the position and speed of the valve rod. It is equipped with an O-ring at its end, which seals when lowered and opens when raised. The speed at which the valve moves significantly affects extrusion properties. Before printing, we establish set points for the open and closed positions of the valve rod where the open position has consistent extrusion, and the closed position does not allow the extrusion or leaking of any ink. Rapid opening of the valve can result in a strong burst of ink initially, posing challenges when aiming for consistent extrusion rates, especially during column printing.

Printing distance is a variable controlled during the 3D printing process. It interacts with the extrusion rate determined by pressure and valve rod positions. Adequate ink flow is necessary for substrate contact before nozzle translation upwards to form the upright column. However, excessive ink can lead to a larger column base if the printing height is too low.

The final parameter under our control for 3D printing columns is the vertical speed profile. It's essential to retract the printer head at the same rate as material extrusion to maintain column thickness. However, excessive retraction may prevent proper column deposition, leading to material accumulation at the base of subsequent columns. Gentle retraction is necessary to avoid carrying excess material to the next column, ensuring consistency. Careful adjustment of vertical nozzle speed is required

for each column structure to prevent weak adhesion or column removal during printing.

Each of these properties is meticulously adjusted for each DIW pattern and ink. The quality of columns may vary depending on ink adjustment and tuning. It is essential to recognize that calibration for each sample can evolve over time due to changes in ink rheology under pressure or the development of clogs in the printer nozzle.

3.3.2 Column Design

The objective is to 3D print low-constriction and high-tortuosity column structures using the nScrypt DIW. Columns offer limited mechanical support parallel to the LLCZN planar surface.

The 3D printer software directly controls two properties of columns: height and separation. While the n-Scrypt 3D printer has limited control over column shape, users can influence it through other parameters. The first directly controllable parameter is height. Essentially, users specify the extrusion stop height to determine the column height. However, due to the high viscosity and non-Newtonian nature of these inks, they may adhere to the nozzle tip and stretch when pulled away, inadvertently increasing the column height. The highly viscous nature of the inks means they do not flow well at rest, often adhering to the printer tip and stretching as the tip moves away from the column, making precise control of column heights, in practice, difficult. The more self-supporting the ink, the better for column structures.

Another crucial factor in controlling our column microstructure is the spacing between columns, which is directly programmed into the n-Scrypt system. The arrangement of columns is also a design decision. To minimize the distance between the cathode and any column, we opted for a hexagonal array, as depicted in figure 3.4.

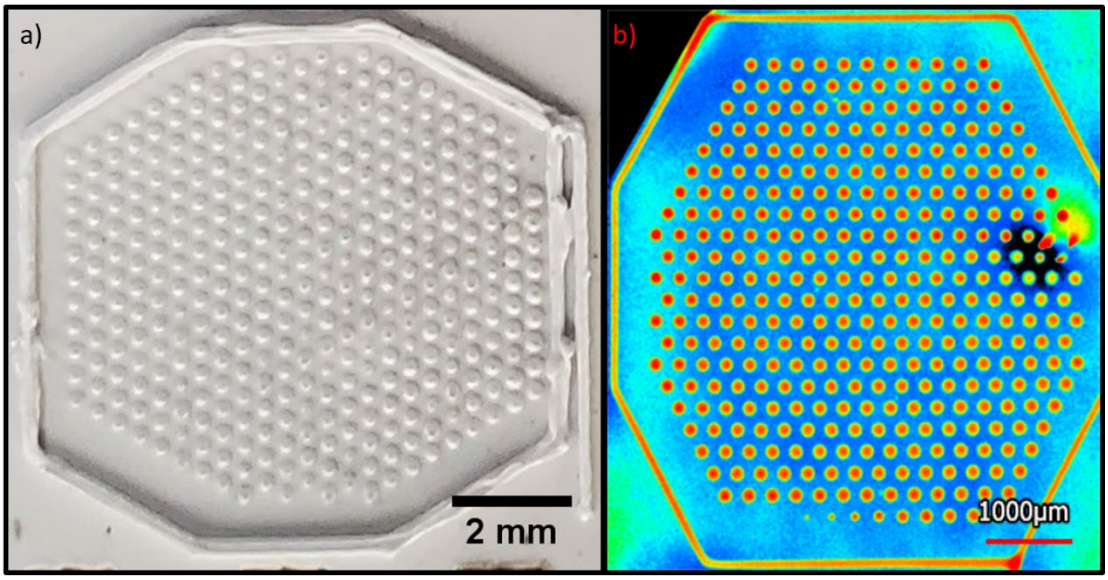

Figure 3.4: Top-down images depict 3D printed columns arranged in a hexagonal pattern: a) an optical image of inks before sintering, and b) a profilometer heat map generated from a sintered column structure.

3.4 3D Printing Process

3.4.1 N-scrypt Commands

Two methods were implemented for DIW columns: the text command method and the fly-by-dots method, with the latter being a more recent upgrade to the n-Scrypt system. The n-Scrypt recognizes three different commands: movement (xyz), translation speed, pauses, valve rod positions, and valve rod speed. Each of these tools can be combined to form the instructions for 3D printing columns. Pressure

remains constant throughout the entire print and is not varied during this process. An excerpt of the text code used for printing will be provided in the appendices.

Fly-by-dots is a more intricate system wherein the process of creating each column is predetermined and a pattern is implemented to specify the printing location of each column. This system is more forgiving, as parsing through 1000+ lines of code to find an error is tedious. Fly-by-dots offer more controls than regular text code, and the user interface provides a visual representation of the printing pattern.

3.4.2 Troubleshooting

Two basic types of issues occur during DIW columns: leaking and clogging. Leaking happens when the ink flows from the nozzle despite the valve rod being set to a height that should prevent ink extrusion. Common fixes for this issue include recalibrating the valve rod closing position due to the O-ring slightly shifting or replacing the O-ring altogether if it has unset itself or developed a crack, breaking the seal.

Clogging arises when an agglomerate or large particle accumulates or becomes stuck in the nozzle opening, impeding the ink flow. Addressing clogging involves removing the printer tip and cleaning out the clog. However, ink clogs tend to recur, indicating an underlying ink issue. Inks clog when the particle size is too large or when ink particles are prone to agglomerating, increasing the risk of clogging.

3.5 Sintering 3D Structures

3.5.1 Sintering Setup and Procedure

Sintering followed a method similar to previous work conducted in our lab. A Li-garnet powder bed was placed on a porous MgO plate, with the 3D-printed sample layer positioned on top and sacrificial-tapes protecting both sides. These tapes prevented the powder bed from adhering to the sample, while the excess Li from both the sacrificial-tape and powder bed served to volatilize sacrificially, preventing Li loss in the samples. Internal investigations conducted by our lab indicated that bilayer structures exhibited better structure after sintering when the dense layer faced downward. This orientation is believed to facilitate the easier removal of extra organics from the porous layer during burn-off, preventing entrapment. Despite the high porosity and open space of the 3D-printed structure, placing it face down should still enable the efficient exit of burn-off species. The mechanical strength of the 3D-printed inks post-printing is sufficient to support the weight of the bilayer and an additional thin sacrificial-tape.

The samples underwent solid-state sintering in tube furnaces. The ramp-up to 600°C was conducted at a slower rate, with temperatures under 240°C ramping up even more gradually to prevent rapid burnout of organics. Temperature holds were set at 240°C and 600°C for one hour each to ensure temperature equilibrium. The designated sintering temperature for Li-garnet was 1100°C for a duration of 3 hours. A schematic of the sintering profile is shown below in figure 3.5.

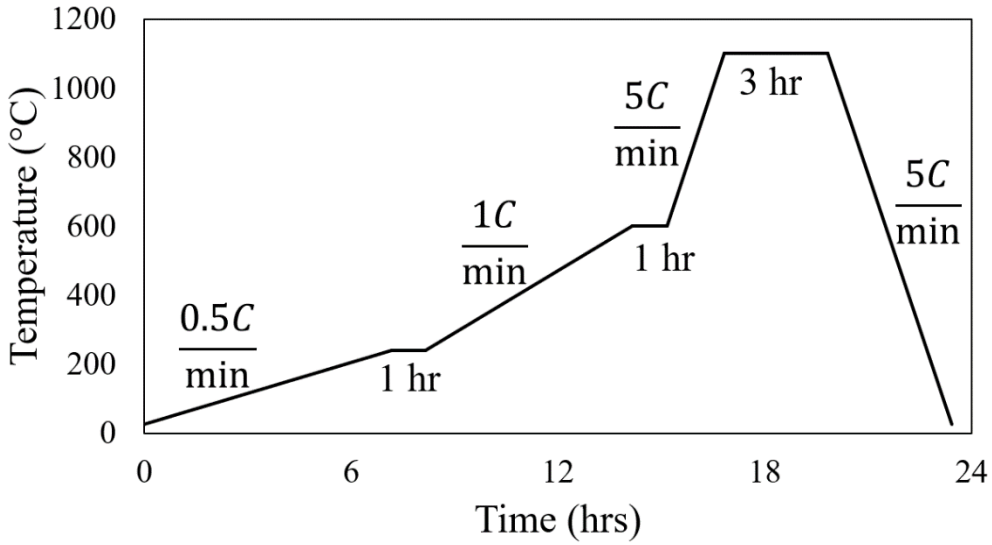

Figure 3.5: Sintering profile of Li-garnet in tube furnaces. The entire process is done in flowing oxygen for just under 24 hours. Holds are at 240°C, 600°C, and 1100°C.

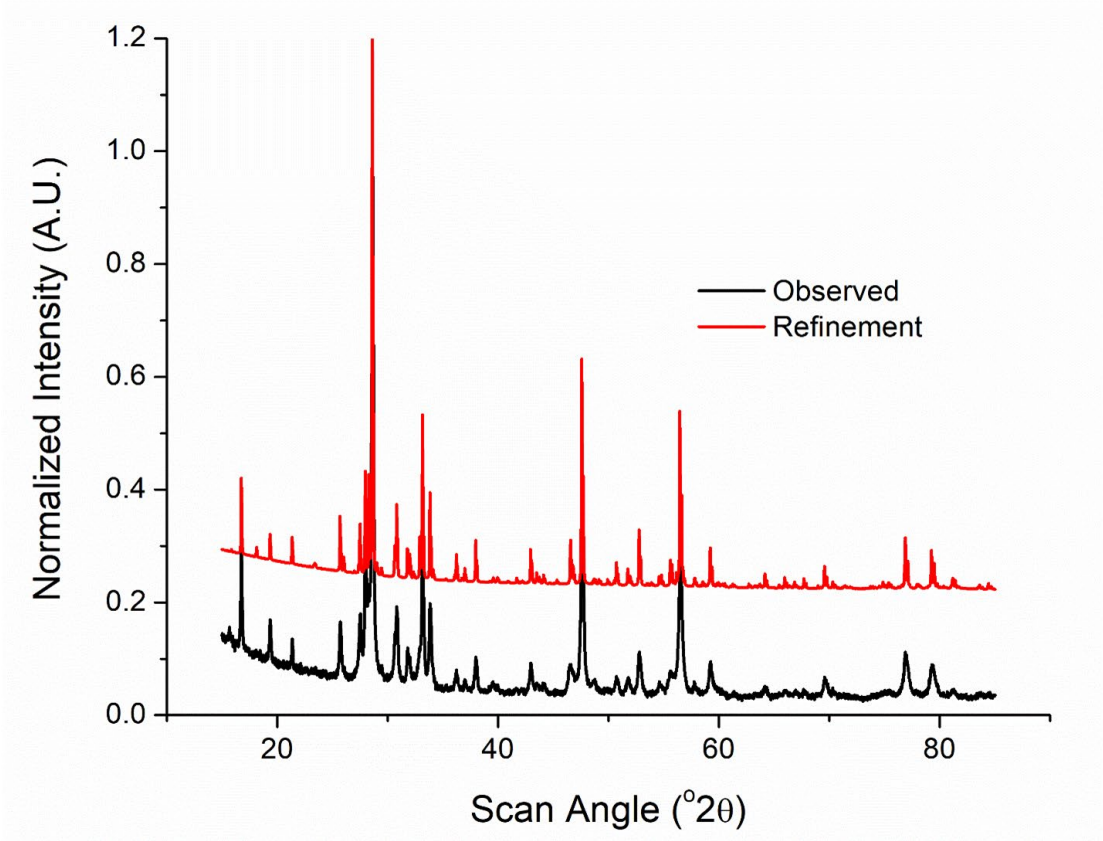

Figure 3.6: XRD pattern of LLZO powder from Trans-Tech after sintering (black) and its Rietveld refinement (Red). No splitting at the peaks indicates cubic phase as opposed to tetragonal.

Oxygen is essential for effectively burning out the organics from the tape and inks; otherwise, residual carbon may remain, potentially leading to cell shorting. A slow organic burnout rate is also necessary to prevent defects arising from excessive organic vapor escaping the system.

The Li-garnet phase of the powder prior to sintering showed high tetragonal phase which is less favorable for ionic conductivity; however after sintering all samples showed cubic phase garnet suitable for solid electrolyte applications as shown in figure 3.6.

3.5.2 Post-sintering Processing

Following sintering, the samples undergo two post-processing steps before cell assembly: Li_2CO_3 removal and ALD. In the Li_2CO_3 removal step, the samples are heated in a furnace to 800°C to eliminate Li_2CO_3 from the surface. This high heat causes an exchange between Li^+ and H^+ ions, resulting in the formation of a species that can be driven off as water and CO_2. This process is conducted in an N_2 or Ar environment. Finally, the ALD process was conducted in the glovebox to facilitate Li metal wetting for the anode.

3.6 Effects of Solvents on Structure

Ethanol, a low-viscosity solvent, was employed to uniformly mix the inks and decrease their overall viscosity. However, an oversight occurred regarding the similarity in composition between the inks and the green tapes, allowing excess fluid in the inks to permeate back into the green tape. As only localized sections of the tape

experience rewetting, no uneven drying issues arise in the green tape. As depicted in figure 3.7, localized cracking at the base of the column resulted from liquid-induced damage to the bilayer structure during uneven drying.

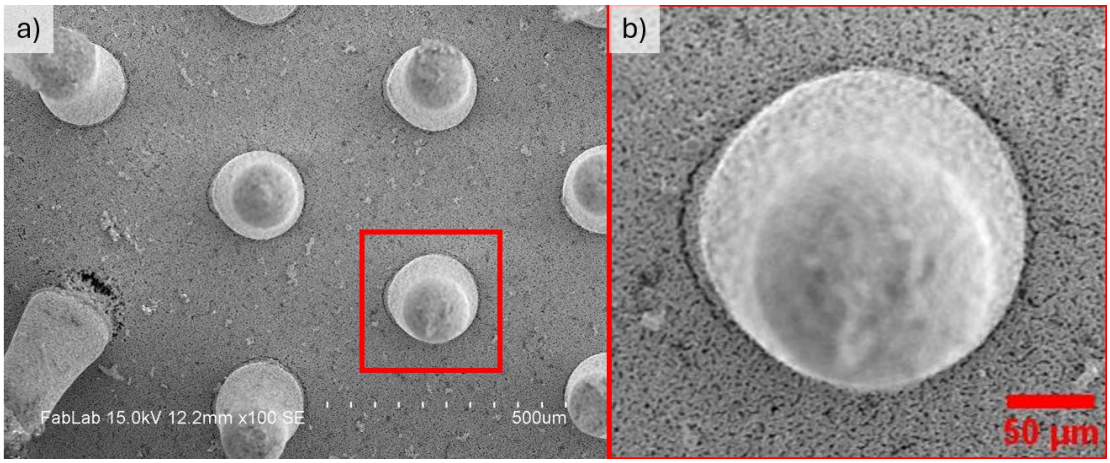

Figure 3.7: SEM images depict columns printed with high solvent loading, resulting in damage to the dense layer due to uneven drying after rewetting of the layers during the 3D printing process.

Due to the rewetting capability of DIW inks on the bilayer substrate, a favorable sintering contact was established between the 3D printed structures and the underlying dense layer. This contact is crucial, as inadequate adhesion would result in poor sintering of the 3D structures to the dense layer, leading to detachment after sintering. Figure 3.8 illustrates a column that toppled over during handling, pulling out the remainder of the dense LLZO layer, serving as evidence of the effective contact achieved by our 3D printed garnet on bilayers.

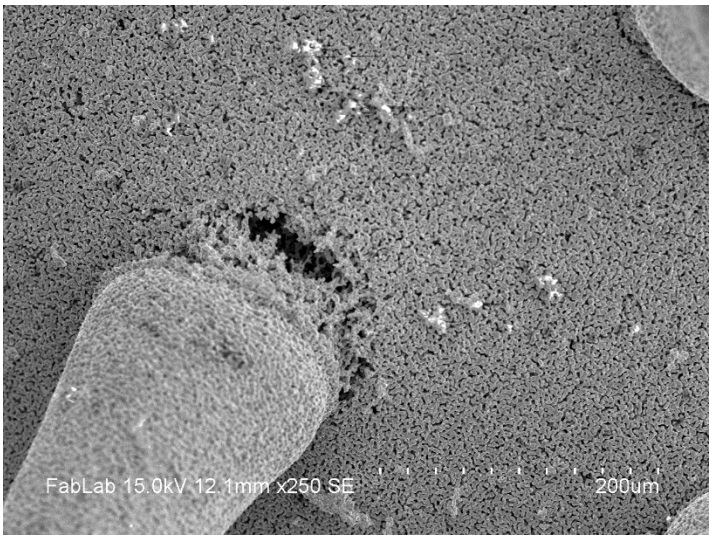

Figure 3.8: SEM images reveal excellent contact between the 3D printed garnet columns and the dense garnet. Accidental knocking over of the column during handling resulted in the extraction of a significant portion of the dense garnet, highlighting the intimate contact achieved.

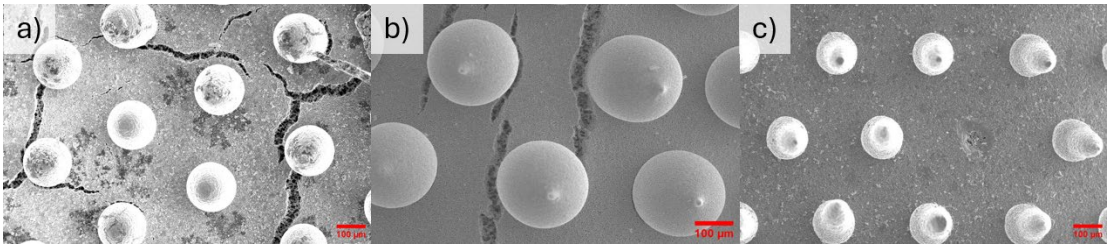

Figure 3.9: SEM images depict samples with 3D printed columns containing varying ethanol content: a) 5.1 wt% EtOH, b) 2.2 wt% EtOH, and c) 1.8 wt% EtOH.

Figure 3.9 illustrates three distinct column structures with varying rheological properties. In figure 3.9a, a highly conformal ink containing 5.1 wt% EtOH is depicted, resulting in the infiltration of a high percentage of EtOH into the dense layer. This led to excess solvent absorption by the dense layer, causing significant cracking during the redrying in the sintering burn off process. Although reducing the EtOH content to 2.2 wt% in figure 3.9b alleviated some cracking issues compared to the 5.1% sample, the problem persisted, ultimately would have resulted in shorting when assembled into a cell. Conversely, in figure 3.9c, the least damaged sample of the three showcases a combination of lower EtOH content (1.8 wt%) and a slower

ramp during the organic burnout phase. Despite a missing column revealing direct visibility into the porous layer, indicating robust adhesion to the dense layer, a portion of the removed dense layer exhibits a shape consistent with solvent absorption, suggesting some degree of solvent adsorption creating weakness in the sample.

3.7 Column Structures and Surface Morphology

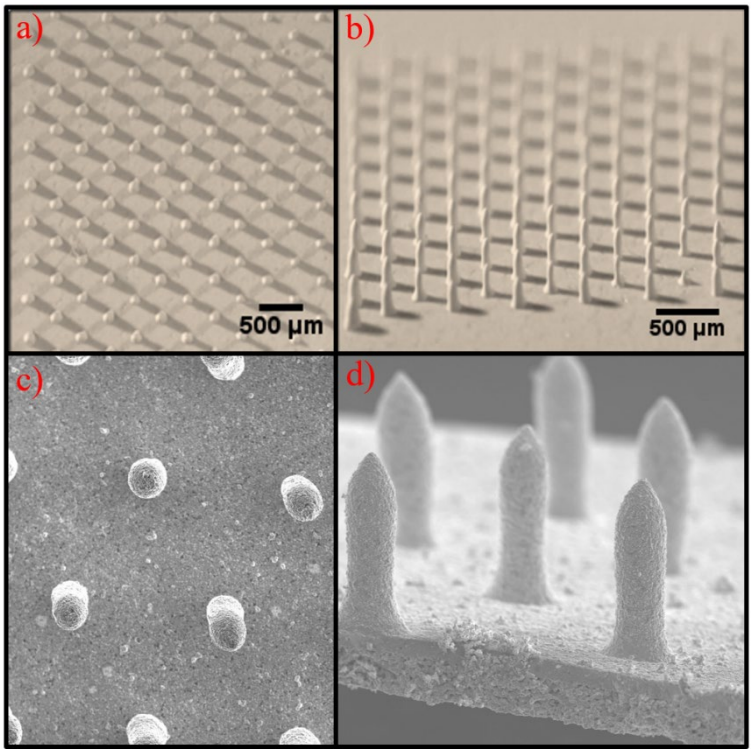

Figure 3.10 a-b) Top-down images show 3D printed columns employing high viscosity inks with rapid recovery time. a) Top-down optical microscope images capturing the pre-sintering 3D printed column structure. b) Isometric view of a column sample before sintering. c) Top-down SEM image capturing the sintered 3D printed column structure. d) Cross section view of a column sample after sintering.

Figures 3.10a-b demonstrate the printing capability of high-quality self-supporting structures prior to sintering. Figures 3.10c-d exhibit top-down and a cross section view of the sintered 3D printed Li-garnet printed structures. As shown in figure 3.10, the structures maintain their shape and integrity throughout the 3D

printing process and are proportionally unchanged during sintering. The structures shrinkage around the same rate as the bilayer LLCZN substrate. A boundary was printed around the entire column array to aid in preventing NMC622 cathode slurry from spilling over the edge of the samples, thus avoiding short circuits.

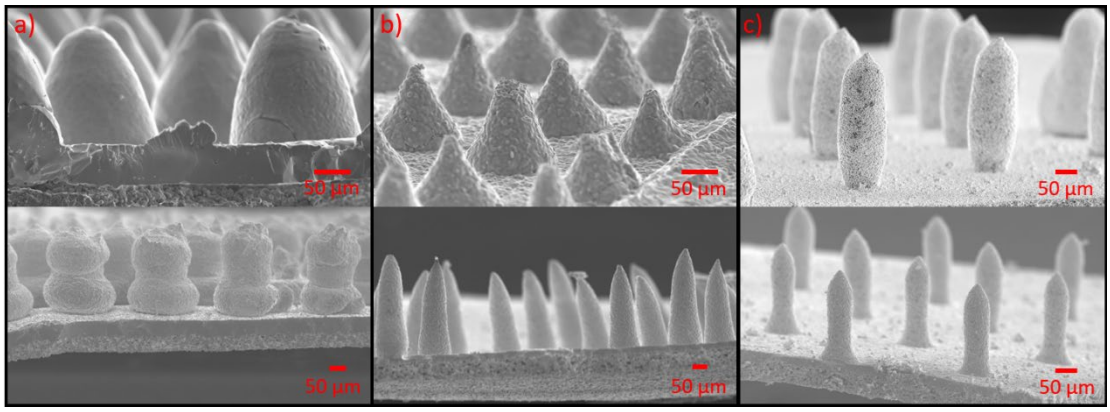

Figure 3.11 a-c) SEM images of various sintered column structures a) columns printed with more conformal inks. b) Columns printed with semi self-supporting inks. c) Columns printed with self-supporting inks.

Figure 3.11a displays SEM images showing column structures printed using conformal inks. These structures exhibit distinct profiles, including half-circle, half-oval, and hourglass shapes. The observed shapes imply lower moduli and higher τ, aligning with the findings of the stress- and time-sweep tests shown in chapter 2. The hourglass shape primarily arises from column collapse directly after extrusion as τ of the ink is high.

Figure 3.11b shows column structures printed using semi self-supporting inks, exhibiting a higher moduli and lower τ compared to figure 3.11a. The rheological properties of the semi-self-supporting inks can be directly compared in chapter 2. The decreased τ leads to straighter, non-vertical edges, resulting in diverse cone profiles which improve direct path conductivity and tortuosity. The higher moduli facilitate

the formation of taller cones because each of these structures were made by inks which have low τ making direct control over the inks final structure possible. Figure 3.11c exhibits a column structure printed using a highly self-supporting ink, as characterized in chapter 2. This ink possesses a significantly high moduli and near-instantaneous recovery time (τ close to zero). The near-instantaneous recovery ensures minimal deviation from the printed shape, enabling the formation of nearly perfect cylindrical columns. Precise adjustment of printing parameters (applied pressure, printing speed, and other minor parameters) is critical for achieving optimal results with these inks. When parameters are properly set, the columns exhibit a near 90° angle at the base, providing minimal tortuosity and direct path conductivity. Slight imperfections to printing parameters can lead to necking at the base of the columns, resulting in constriction. Consequently, Li^+ must conduct through a more narrow pathway compared to the rest of the column which is bad for diffusion and by extension conductance. Cells with necking at the base of the column as seen in top sample of figure 3.11c were also more likely to break after sintering because that narrow connection to the dense layer is a mechanical weakness.

3.8 Li-NMC Cell Assembly and Testing

In an argon glovebox environment, lithium metal was melted into the pores of the LLZO samples. Typically, NMC calendaring is employed to enhance NMC cathode performance.[103] However the proposed 3D structure combined with the brittle nature of Li-garnet, poses challenges for calendaring without fracturing the Li-garnet structure, so on the cathode side, 3 μL of 1M $LiPF_6$ in EC:DEC (1:1) liquid electrolyte are employed to promote improved interfacial contact. Additional carbon-

black was drop cast on the surface of Li-garnet 3D printed structure for extra electronic conductivity. A well-mixed conventional NMC622 cathode was prepared for the batteries, so conductivity is not affected by any localized tortuosity within the cathode. 1 mg/cm^2 NMC loading is deposited within the 3D structure of the cell (Figure 3.1). The assembled cells were sealed in a 2032 coin cell within an argon-filled glovebox.

LLZO sintered 3D-printed layers were observed using a Hitachi SU-70 SEM in the UMD AIMLab and a Hitachi S-3400 SEM in the UMD FabLab. EIS was performed over a frequency range of 1 MHz to 1 Hz on a Solartron SI-1260. Cell testing was conducted using an Arbin battery cycler at a 0.05C rate, with voltage cycling between 2.5 V and 4.35 V at room temperature (22°C).

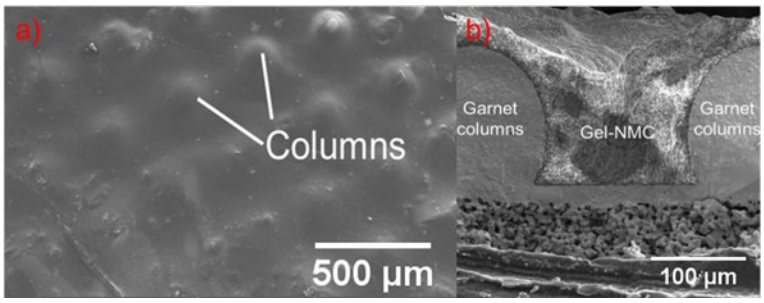

Figure 3.12: SEM images show 3D printed cells infiltrated with a NMC622 slurry containing carbon black. a) Top-down view of columns coated with the drop-casted NMC622 slurry. b) Presents cross-section images showing the close contact between the NMC622 slurry and the 3D printed Li-garnet electrolyte.

Full cells were fabricated and filled with an NMC622 and carbon black slurry. Figure 3.12 shows that the cathodes were made with good interfacial contact between Li-garnet structures and NMC/carbon black slurry. The gel-NMC fills the porosity left by the columns and no identifiable voids were found in the cathode layer. In figure 3.12b, our additional carbon layer for improved electronic conductivity is shown in between the garnet columns and the NMC622 cathode.

We used 3D printing to shape Li-garnet ink into columnar structures with different physical dimensions on Li-garnet bilayer tape substrates as shown in figures 3.13a-c. Figure 3.13a-c shows the cross-sectional SEM images of 3D printed Li-garnet electrolytes used to make Li-NMC full cells. Additional information about the printed structures is listed in Table 3.1. The corresponding cell impedance is shown in figures 3.13d-f and cell cycling is shown in figures 3.13g-i.

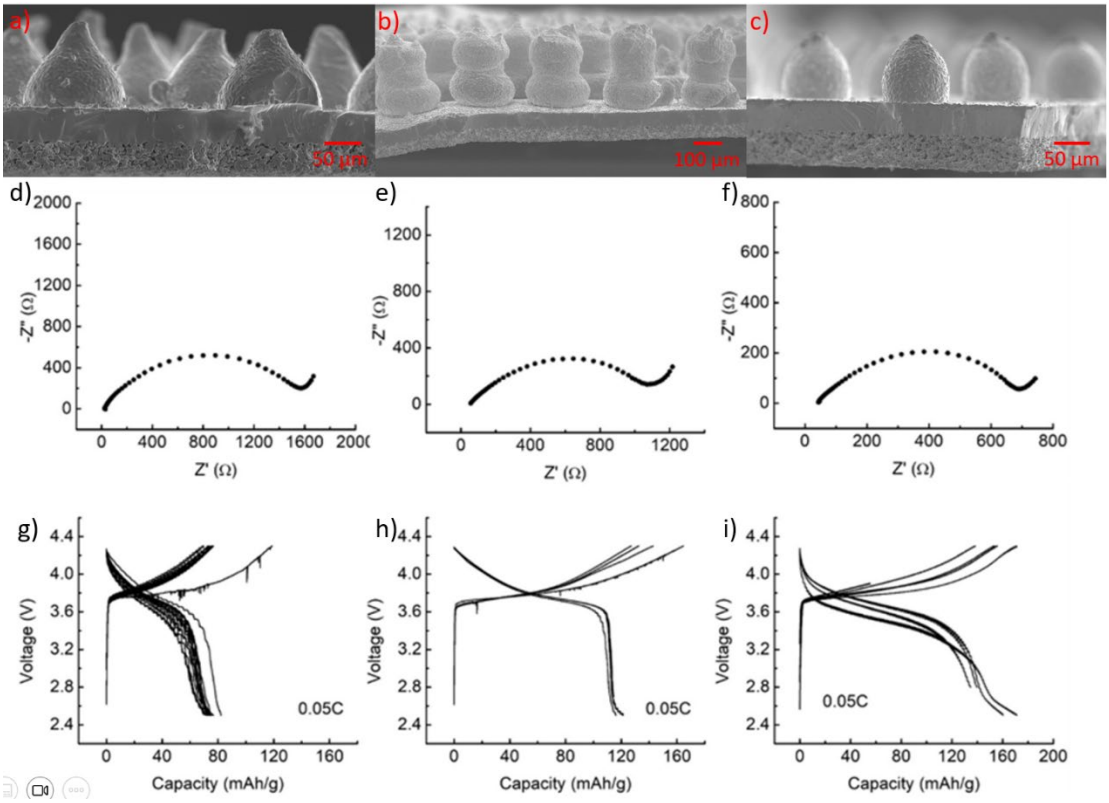

Figure 3.13: a-c) SEM cross-section images illustrate the DIW structure of three cells reported in this work. d-f) EIS measurements were conducted on the structures when assembled into Li-NMC622 cells. g-i) Cell cycling results show 20 cycles for each of the assembled structures in Li-NMC622 cells. The cells were tested between 2.5V to 4.3V, a rate of 0.05C, and at room temperature (22°C).

Figure 3.13a shows the cross section of cell 1 showing an increased in the available surface area of 99.8%, with 75.4% open porosity, and with column height

average of 106 μm. Figure 3.13b shows cell 2, showing taller average column height at 280 μm with a higher surface area increase of 331%, and a low open porosity of 60.5%. Figure 3.13c shows the cross section of cell 3 which had the lowest added surface area of 57.8%, the most open porosity of 88.0%, and an average column height of 96.3 μm. Each of the above cells were printed to take up about a 0.5 cm^2 area after sintering.

Table 3.1: Compiled information about the 3D printed structures and cells shown in figure 3.13. Additional surface area represents the percent increase to surface area compared to a planar interface. Surface area to volume ratio only considers the surface area and volume added by the columns. Porosity is calculated from the void space between the columns and nothing above the column height. Impedance is measured from the EIS. Discharge capacity was taken from the initial capacity after the formation cycle and coulombic efficiency is the final coulombic efficiency after 20 cycles.

Cell Number	Additional Surface Area	Surface Area/Volume Ratio	Median Column Height	Porosity	Impedance	Discharge Capacity	Coulombic Efficiency
1	100%	3.86×10^{-2} μm^{-1}	106 μm	75%	1590 Ω	82 mAh/g_{NMC}	97.6%
2	331%	3.02×10^{-2} μm^{-1}	280 μm	61%	1080 Ω	120 mAh/g_{NMC}	91.7%
3	58%	5.06×10^{-2} μm^{-1}	96.3 μm	88%	690 Ω	170 mAh/g_{NMC}	98.2%

Figure 3.13d presents the Nyquist plot for the EIS characterization of cell 1. The limited increase of NMC utilization resulting from the size and shape of the structures led to a cell impedance of 1590 Ω. Figure 3.13e is the Nyquist plot of cell 2 showing reduced impedance of cell 2 compared to cell 1, likely from the increased surface area of the structures creating more interface for Li^+ transfer. These columns

may introduce minor losses associated with tortuous paths. The overall improvement in surface area led to a cell impedance of 1080 Ω. Cell 3 demonstrated the lowest impedance among the three cells at 690 Ω (Figure 3.13f). This is likely attributed to the shorter diffusion distance of the Li^+ enabled by increased porosity.

In figure 3.13g, Cell 1 exhibited a low initial capacity of 81.9 mAh/g_{NMC}, which can be attributed to loss in performance from higher impedance compared to Cell 2 and Cell 3. The coulombic efficiency of the cell remained high at 97.6% after 20 cycles. The presence of capacity fade, along with the poor initial capacity, indicates the deterioration of interfacial contact between NMC and Li-garnet during cycling, resulting in reduced access to the cathode over time likely due to minimal additional surface area added by the DIW. Cell 2 in figure 3.13h demonstrated enhanced initial capacity and low capacity fade over 20 cycles. The high capacity of 120.3 mAh/g can be attributed to the significantly increased interfacial area between NMC and Li-garnet achieved by the improved column structure. The specific geometry of the columns may mitigate interfacial separation during cycling, resulting in the lowest capacity fade among the three reported cells. In figure 3.13i, Cell 3 showed the highest capacity among the three cells, with an initial capacity of 169.9 mAh/g although it still showed some capacity fade. The column structure of cell 3 likely facilitated improved NMC interface which enabled more cathode utilization improving the capacity.

From the cell data in figure 3.13, notably cell 2 had the least amount of capacity fade among the tested cells. The 3D printed structure of cell 2 had visually the highest tortuosity of the 3 cells. The roughness of the columns could trap the

cathode preventing it from separating between cycles. Since each of the cells in figure 3.13 were constructed by hand, there are possible dependencies not captured by the cell performance data. We hypothesize that increasing surface area and surface area to volume ratio are beneficial to improving battery performance. There is likely an optimum height for Li-garnet columns as too short columns limits cathode capacity and too tall columns increases cell resistance by increasing conduction path length. Increased porosity allows a higher amount of cathode to be infiltrated. Li-garnet structure provides an ionic conduction pathway and a surface for an electronically conductive coating. There is likely an optimum porosity for 3D column structures dependent on the surface area to volume ratio and spacing of the columns. 3D modelling could help support these hypotheses in future work.

3.9 Column Structures with a Li-SPAN Battery

3.9.1 SPAN Background

Cobalt has been a rising concern in the battery community due to its rarity and methods of acquisition. There are estimates of global cobalt shortages as early as 2042 if new sources of cobalt are not discovered and cobalt consumption does not decrease.[104] Many researchers have started investigating other promising cathodes. One of which is sulfur as it is much more earth abundant than cobalt and it is also far cheaper. Sulfur has an extremely high theoretical capacity at 1675 mAh/g which is much higher than other commercially available cathodes as seen in figure 3.14.

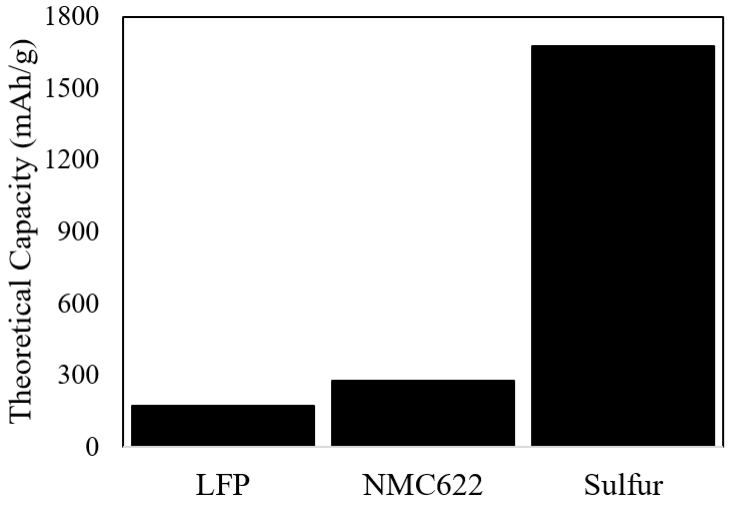

Figure 3.14: Bar chart comparing the theoretical capacities of LFP (170 mAh/g), NMC622 (277 mAh/g), and elemental sulfur (1675 mAh/g).

SPAN emerged as the preferred choice for the sulfur active material, owing to its demonstrated superior cycling stability, enhanced electronic conductivity, and reduced volume expansion compared to elemental sulfur.[105–107] Shi et al. introduced Li-S solid-state systems with gel-polymer catholytes, incorporating SPAN as the cathode material, which exhibited remarkable capacity and capacity retention on a planar interface.[108] The SPAN/LiFSI cathodes can easily undergo melt infiltration, enabling seamless integration with 3D LLZO microstructures possessing sufficient porosity.[108] The SPAN/LiFSI cathode developed by Shi et al.[108] was used within a 3D printed column structure atop a bilayer configuration.

3.9.2 SPAN Cell Assembly and Results

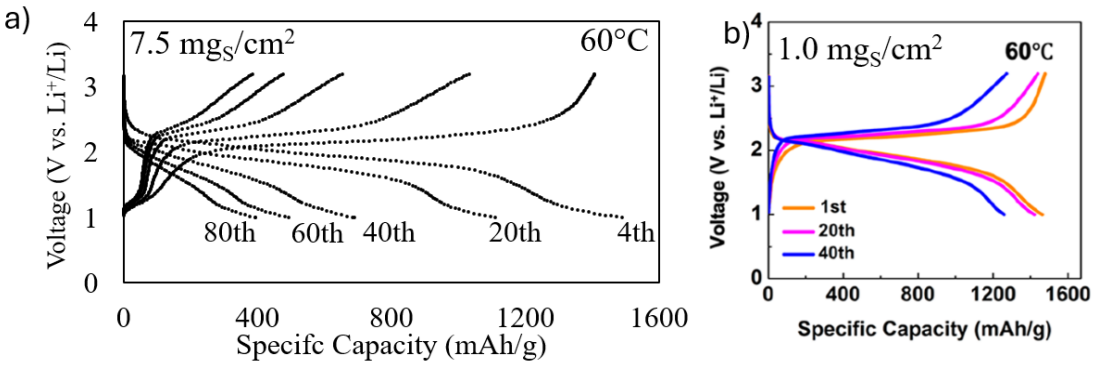

Figure 3.15: Comparison of 3D printed Li-SPAN cell (a) and bilayer Li-SPAN cell from literature (b).[108] 3D printing allowed achieving theoretical capacity of SPAN at 1594 mAh/g_S. with 7.5 mg_S/cm^2 loading. Bilayer SPAN cell did not achieve theoretical and only had 1.0 mg_S/cm^2 loading. Both cells were cycled at 60°C at similar rates.

The SPAN/LiFSI cells were assembled following the methodology described in Li-NMC cells. Figure 3.15 presents the cycling performance of the cell incorporating Shi et al's[108] procedure into a DIW LLZ scaffold. In figure 3.15a, I achieve the theoretical capacity 1594 mAh/g_S with 7.5 mg_S/cm^2 loading at 60°C and 0.05C rate. This is a major improvement over the earlier work done with a bilayer Li-SPAN cell with only 1.0 mg_S/cm^2 loading (figure 3.15b).[108]

Capacity fade was a major issue for the 3D printed cell which lost 75.3% of its original capacity over the 81 cycles averages about 1.5% capacity loss per cycles which is poor. This capacity fade is likely attributed to the exceptionally high loading accomplished which also drastically increases the amount of volume expansion experienced by the SPAN cathode.

Post-mortem SEM analysis in figure 3.16a confirmed the separation between the SPAN/LiFSI cathode and the LLZO surface. Furthermore, a comprehensive top-

down view in figure 3.16b revealed surface cracking on the SPAN/LiFSI cathode, indicating that the performance decay is likely attributable to sulfur volume expansion.

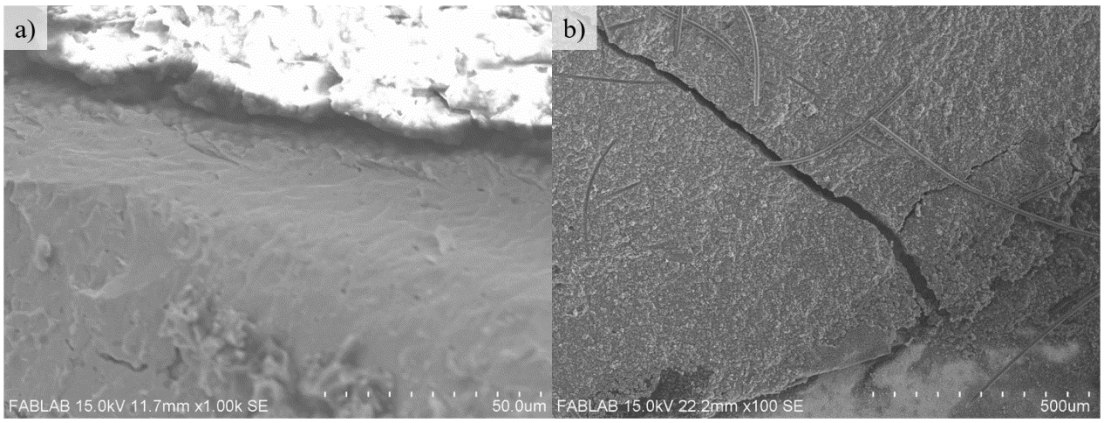

Figure 3.16: SEM images revealing degradation of the SPAN/LiFSI after cycling caused by volume expansion and loss of cathode contact.

3.10 Conclusions

In this chapter, the sintering of DIW Li-garnet samples and cell performance (EIS and cell cycling) of 3D printed Li-garnet batteries with a Li-NMC622 system were studied. The results indicate the following:

(1) Reduction of carrier solvents such as ethanol are necessary to prevent damaging of green tapes. Additional ethanol causes cracking rendering the bilayer structure unusable.

(2) NMC/carbon black slurry was homogenous and had good contract with the Li-garnet enabling low impedance and high-capacity cells. Additional carbon layer added with drop casting successfully conformed the 3D printed structures creating an electronic conduction aid.

(3) The 3D printing added significantly more surface area compared to the planar surface of the dense layer. These structures are not providing as much additional surface area as the porous layers created by Hitz et al.,[69] but this can be improved with more self-supporting inks by increasing the surface area to volume ratio of 3D printed structures. 169.9 mAh/g_{NMC} with minimal capacity fade was achieved.

(4) Implementation of DIW columns with Li-SPAN cells produced extremely high specific capacity (1594 mAh/g_S), but ultimately failed due to volume expansion during cycling. Improvements could be made with implementing methods to maintain good contact between Li-garnet and the SPAN cathode.

Chapter 4: Direct Ink Writing $Li_7La_3Zr_2O_{12}$ Grids for Li-S Batteries

4.1 Direct Ink Writing Li Garnet Grid Structure

4.1.1 Sulfur Cathodes

40% of the global cobalt supply is currently allocated to battery cathodes making the escalating price of cobalt a concern for the future of affordable batteries.[104,109] While cobalt is a key component in high-performance cathode materials, exploring suitable alternatives is crucial to maintain affordability of future batteries. A promising solution lies in the combination of the high capacity lithium metal anode with globally plentiful sulfur cathode with a high theoretical capacity 1675 mAh/g).[2,41,110,111] However, the use of liquid electrolytes in lithium-sulfur

systems introduces complications, including polysulfide shuttling, Li dendrite growth, and low coulombic efficiency.[35–39] The implementation of ceramic SSEs addresses many of these issues since lithium sulfide species are incapable of dissolving into them.[112,113] Of these options, garnet-type electrolytes have demonstrated exceptional performance attributed to their high ionic conductivity, chemical stability, and electrochemical stability.[50,53,69,73,114,115] In previous research, a trilayer structure demonstrated consistent performance, yielding over 1075 mAh/g_S in Li-S cells for more than 50 cycles, with minimal capacity degradation.[70]

4.1.2 Grid Structures for Cathode Scaffolds

In the preceding chapter, Sulfur-Solid-State Batteries (SSBs) were fabricated utilizing a Li-NMC and Li-SPAN system integrated with a Li-garnet column architecture. Notably, significant losses were observed in these structures, primarily attributable to volume expansion-induced detachment of the cathode from the garnet interface. In contrast, prior utilization of sulfur cathodes within the trilayer configuration showed minimal capacity loss, suggesting a potential role of the narrow pores within the structure in mitigating volume expansion-related capacity decay. However, the fabrication of column structures presents constraints, particularly concerning the spacing between features and column height. Taller columns necessitate increased separation to avert collision between the column tip and the printer nozzle, underscoring the need for further exploration into alternative pore geometries.

This chapter will employ the same Li-garnet inks and correlate their rheological characteristics with grid structures. Furthermore, these structures will be integrated into Li-S batteries to correlate the influence of 3D architecture on battery performance. We will construct Li-S batteries by printing a mechanically confining grid structure onto a bilayer Li-garnet structure, while filling the random porous layer of the bilayer with Li metal and a sulfur/carbon slurry cathode within the 3D printed framework, as illustrated in figure 4.1.

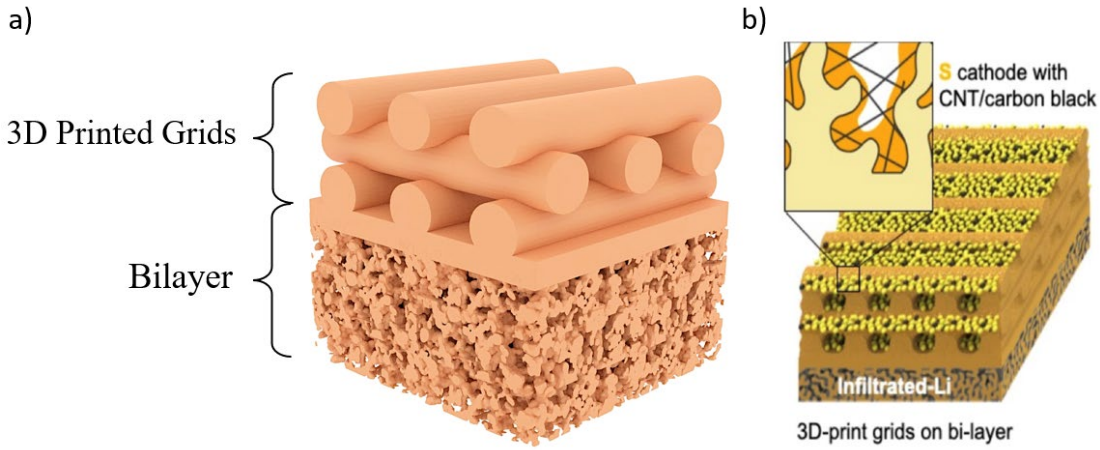

Figure 4.1: a) 3D schematic of a grid DIW electrolyte scaffold. b) Schematic representation of a complete Li-S/C cell, showcasing Li metal infiltration on the porous side of the bilayer and sulfur and carbon infiltration into the 3D printed side opposite to the Li metal.[116]

4.2 3D Printing Design

4.2.1 Substrate Design

To start DIW LLZO as established in chapter 3, an appropriate substrate must be constructed. The design goal is to use the trilayer structure developed by Hitz et al. and replace one of the porous layers with a 3D printed grid structure as shown in figure 4.1.[69] The grid structure offers superior mechanical stability compared to its

column counterparts, suggesting the potential to decrease the thickness of the dense layer for support purposes. Moreover, the grid structure's capability in this regard opens the possibility of 3D printing on both sides of a dense substrate, a topic slated for exploration in an upcoming section. Overall, substrate design for the Li-S cells will not change from chapter 3 except for the 3D printed symmetrical structures will no longer require a porous tape cast and laminated.

Laser perforation of the samples will follow the same procedure as the previous samples, utilizing the identical nine samples from a 4 cm by 4 cm bilayer. One notable advantage of the purely symmetric 3D printed structures is the elimination of concerns regarding warping due to differing shrinkage rates on the dense and porous layers.

4.2.2 Structure Design

Unfortunately, the implementation of an alternating stacked-raster grid structure means a sacrifice the structure tortuosity is being made at the cost of improving Li-garnet and sulfur cathode interface. There is a risk of increasing constriction in the structure if the inks exhibit excessive self-supporting properties and fail to amalgamate to create a sizable contact area. This could also lead to a reduction in cathode depth, which is essential for increasing solid loading. Excessive merging of the two layers would result in a single layer and a substantial loss of available porosity for the cathode. For this specific application, it is important that relaxation time is more moderate to ensure self-supporting behavior while also facilitating proper contact between raster layers to avoid the formation of highly constrictive interfaces.

Printing was performed using an nScrypt 3Dn-300 printer, which was equipped with ceramic printer heads measuring with 50 µm and 75 µm diameter heads. The presence of large LLZO powder particles within the ink will cause blockages in the printer's nozzle and had to be minimized. Extra milling in ZrO_2 media was utilized to ensure smooth extrusion and optimal printing performance. The extrusion pressure, printer head speed, and other minor printing properties were adjusted individually for each ink based on their distinct rheological characteristics and printing requirements. The sulfur/carbon cathode cells in this study utilized the grid structures initially demonstrated by McOwen et al.[82] The grid structures are created by extruding line raster pattern stacking with each subsequent layer rotated 90° bridging on top of the layer below.

4.3 3D Printing Grid Structures

4.3.1 N-scrypt Instructions and Raster Design

Several methods exist to implement the stacked raster design using DIW. In this study, text-based instructions were employed to control the structure. Due to the simplicity of stacked rasters, text commands are highly effective in controlling the movements for this type of print.

Unlike column structures, this approach involves printing layer by layer to ensure consistent printing per layer before proceeding. This means that only XY movements need to be tuned, and a constant flow is all that is necessary to ensure the ink prints consistently, as this type of instruction does not require the valve rod to open or close constantly. An example code will be provided in the appendices.

The grid structures need to be stacked to increase the cathode thickness unlike the column structures which can just adjust the height of the columns in the print file. Stacking these structures can have complications however. For a layer to print successfully, the previous layer just have successfully printed fully to prevent errors or collapse of the current layer. Each layer printed has a certain success rate, so therefore stacking up higher and higher grid structures becomes increasingly harder. In figure 4.2, it is demonstrated that 3-layer grid structures are achievable, but it was not consistent. If a minor deviation, such as excessive layer merging, occurs, it affects all subsequent layers. These cumulative deviations significantly reduce the consistency of 3-layer grid structures during printing. Achieving higher grid structures necessitates more precise control over ink rheology.

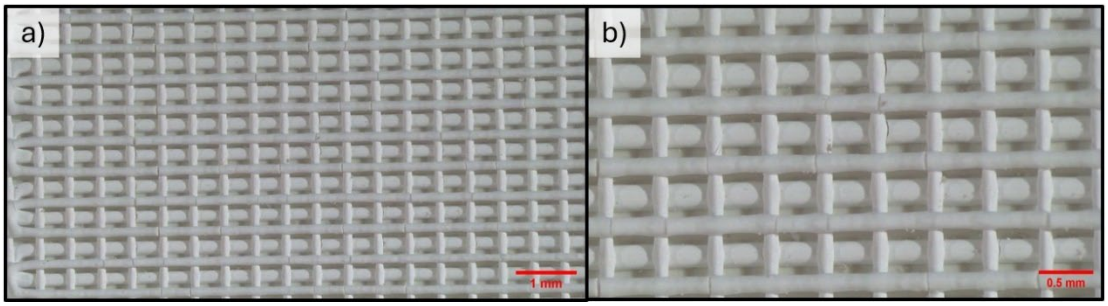

Figure 4.2: Top-down optical microscope images depict 3-layer grid structures. Layers 1 and 3 are aligned in the same direction, while layer 2 runs perpendicular to layers 1 and 3. Layers 1 and 3 are offset from each other, allowing both layers to be visible in the optical image.

4.3.2 Direct Ink Writing Grid Adjustments

Utilizing the inks from our previous studies, we successfully printed grid structures characterized by thin features (~100 µm) with low spacing (~577 µm). Figure 4.3 shows a range of unsintered DIW LLZ structures fabricated using our self-supporting inks. As described in our earlier research, adjustments to storage modulus

(G'), loss modulus (G''), and viscoelastic recovery time (τ) enabled us to achieve finer structures compared to our previous iterations.

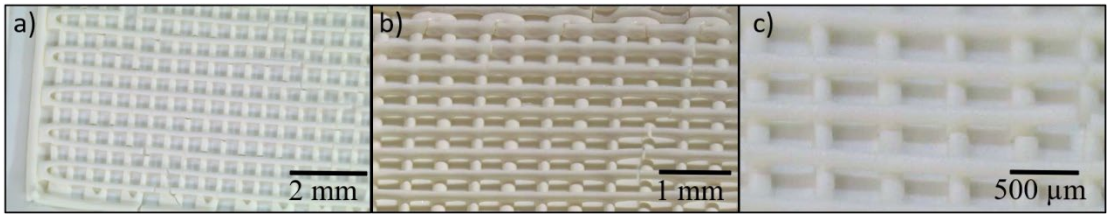

Figure 4.3: a-c) Top-down optical microscope images showcasing 3D printed grid structures prior to sintering. High-definition representations of each structure were obtained, demonstrating precise control during the 3D printing process.

4.4 Sintering LLZO Grid Structures

4.4.1 Sintering and Post Sintering Procedure

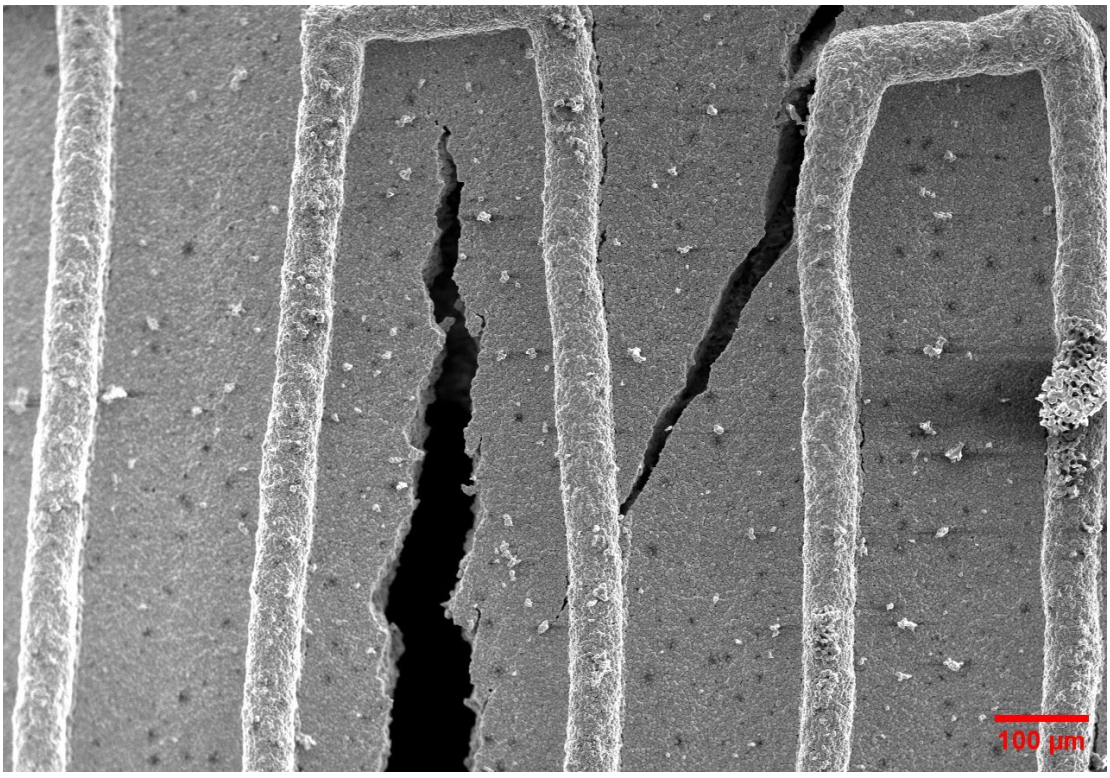

Figure 4.4: Splitting in the dense layer due to excess liquid absorption, resulting in localized weaknesses that cracked during sintering.

In line with the preceding research, this study employs the heating profile outlined in chapter 3, featuring a gradual increase in temperature to facilitate slow organic burnout, followed by a 3-hour hold at 1100°C for solid-state sintering. Consistently, maintaining a slow ramp rate for organic burnout and minimizing organic solvents in the ink remains crucial to prevent damage to the dense layer. Figure 4.3 emphasizes analogous damage to the dense layer observed previously in figure 3.9.

Li_2CO_3 removal occurs under flowing Ar environment at 800°C, facilitating the volatilization of hydrogen and adhered carbon as water and CO_2. ALD of ZnO enhances Li^+ wetting within the porous layer.

4.4.2 Shrinkage-Based Cracking

From a sintering perspective, the column structure offers a significant advantage, as shrinkage mismatch does not significantly impact structural defects. However, when examining the alternating raster grid structure, extensive lengths of ink are printed parallel to the dense layer substrate plane. Consequently, any shrinkage disparity between the dense layer and DIW ink leads to stress accumulation within the sample. There are two critical points in time where the ink undergoes shrinkage: 1) immediately after printing, where the high printed surface area allows for the volatilization of organic species, and 2) during sintering, where the organics are burned off during the heating step en route to sintering. Like the study in chapter 3, this exemplifies the importance of minimizing the EtOH and other organics content in the inks.

4.5 Cell Assembly and Cycling

4.5.1 Lithium Symmetric Testing

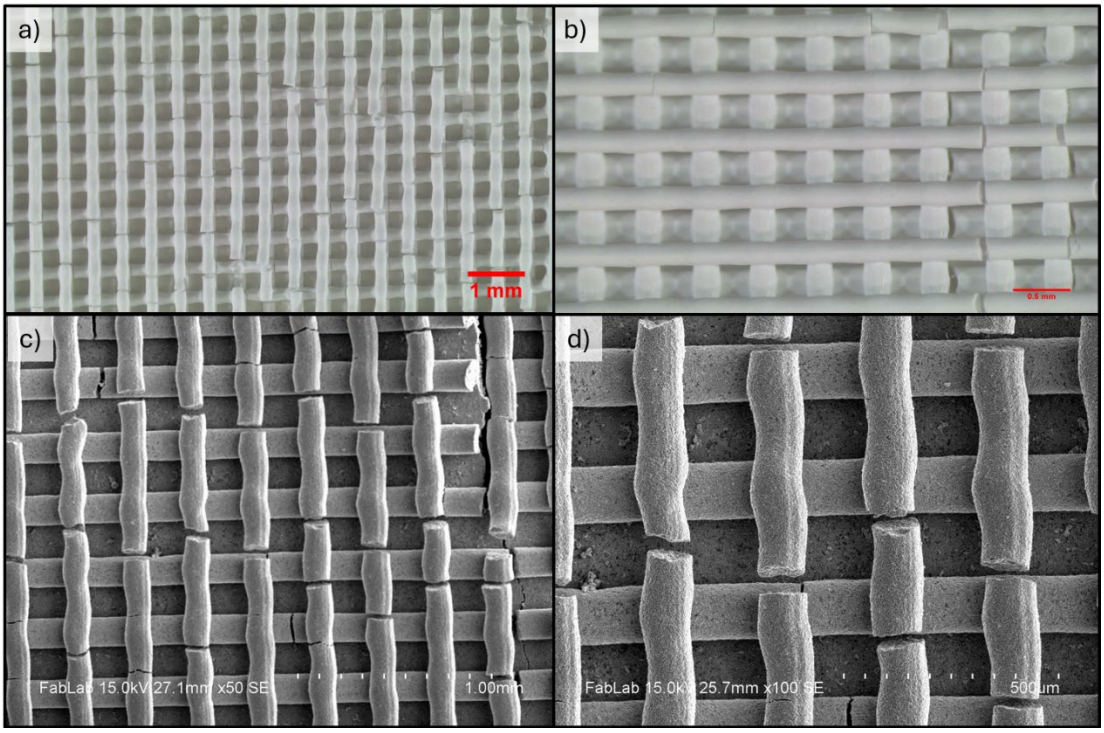

Figure 4.5: Shrinkage-induced cracking is evident in the grid structure both before and after sintering. a-b) depict grid structures experiencing structural breakages during the drying process after 3D printing. c-d) show an increased frequency of grid structure breakages after sintering, likely due to greater shrinkage during the organic burnout step.

Lithium symmetric cells were constructed from 3D printed grid structures to directly compare with previous work.[82] Figure 4.6 shows a direct comparison between Li-symmetric cells made by McOwen et al. and the newest Li-symmetric with the updated ink composition. In figure 4.6a, McOwen et al. reported an impedance of approximately 38 Ω cm^2 in their symmetric cells from their EIS with their 3D printed structures shown in figure 4.6b.[82] By incorporating more self-supporting inks, a slightly improved impedance of 27 Ω cm^2 was achieved, as shown

in figure 4.6c due to reduced constriction and more self-supporting structures as seen in figure 4.6d. The latest improvements of inks significantly improve the consistency of the 3D structure aspect ratio by reducing the inconsistencies caused by conformal ink behavior.

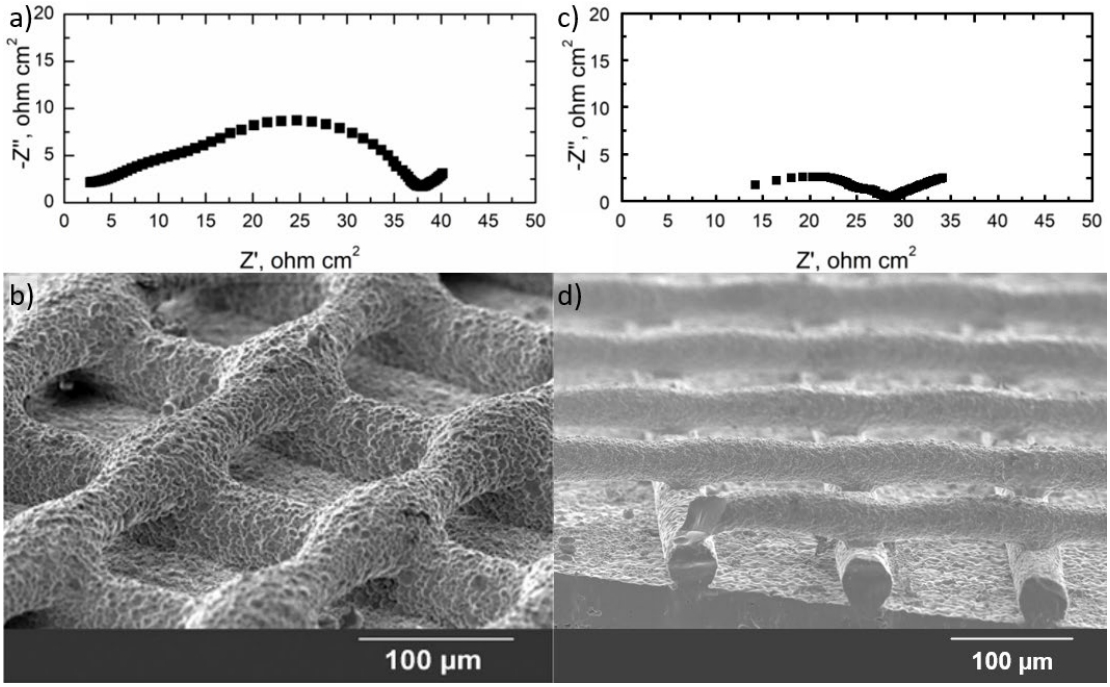

Figure 4.6: a) Li-Li symmetric cell EIS area-normalized Nyquist plot was reported by McOwen et al.[82] b) SEM of the 3D printed raster pattern reported by McOwen et al.[82] c) Li-Li symmetric cell EIS area-normalized Nyquist plot is presented in this study. d) SEM of the 3D printed raster pattern printed for direct comparison to past work.

4.5.2 Sulfur Infiltration and Cell Assembly

In an argon environment, lithium metal was melted into the pores of the bilayer LLZO structure. On the cathode side, a carbon nanotube slurry was drop cast to aid electronic conductivity. The cathode was created by drop casting a mixture of sulfur and carbon nanotubes in a ratio of 35:1. A sulfur loading of 1 mg_S/cm2 and a liquid electrolyte consisting of 3 µL of LiFSI dissolved in DME were employed to facilitate improved interfacial contact between LLZO and the sulfur cathode.

Following assembly, the cells were enclosed within a 2032 coin cell and sealed in an Ar-filled glovebox. Impedance measurements were conducted using a Solartron SI-1260 impedance analyzer across a frequency range spanning from 1 MHz to 1 Hz. Cell testing was performed using an Arbin battery cycler at a rate of 0.02C, with voltage cycling between 1.1 V and 3.0 V at 22°C.

Li metal was melted into the random pores for intimate contact, as seen in figure 4.7. The 3D printing structure was adapted on top of a bilayer from previous work.[102] Full cells were assembled and drop cast filled with a slurry comprising elemental sulfur and carbon nanotubes. Figure 4.7 illustrates the cathodes showing excellent interfacial contact between the Li-garnet structures and the sulfur/carbon nanotube slurry. The sulfur slurry occupies the porosity created by the grids, and no discernible voids were observed in the cathode layer.

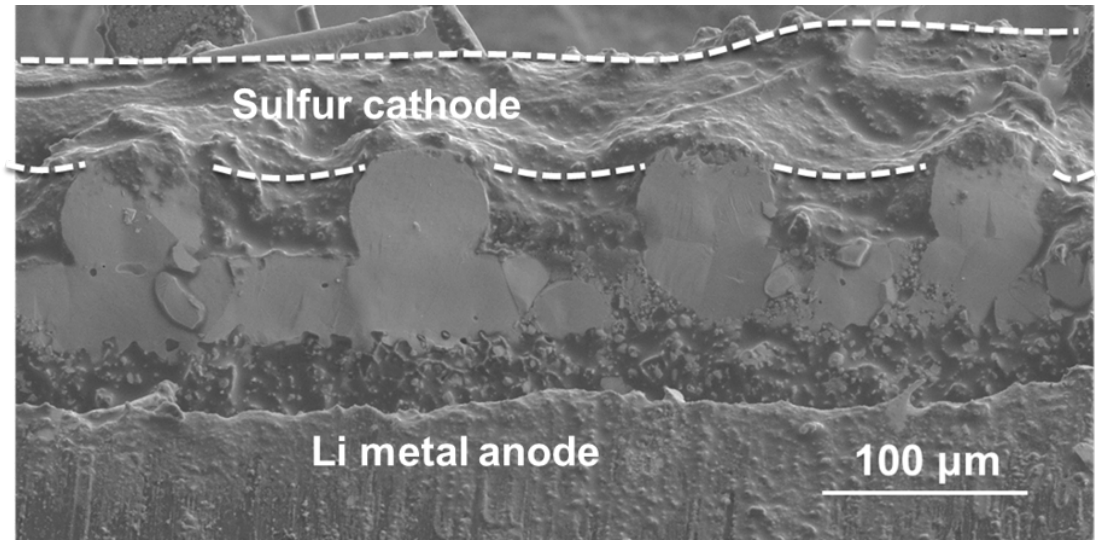

Figure 4.7: Cross-sectional image showcasing intimate interface between the S/C slurry and the 3D printed grid LLZO electrolyte.

4.6 Li-S Cell Results and Analysis

4.6.1 Li-S Impedence and Cycling

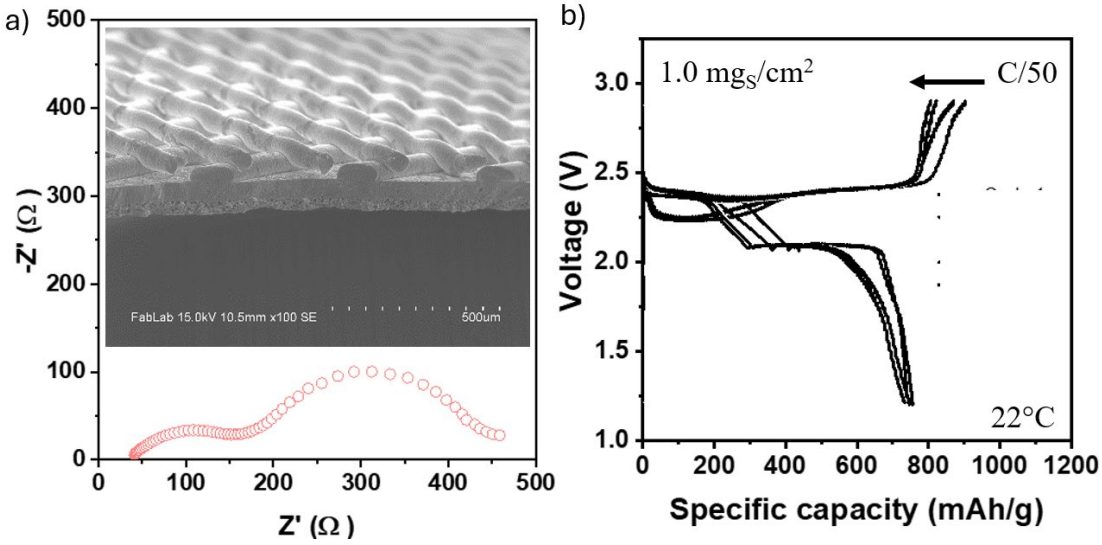

Figure 4.8: a) EIS measurement of a Li-S/C with an inlayed SEM of the 3D printed grid microstructure. b) Cell cycling results of this cell after cycling 16 cycles. The cell had a mass loading of 1 mg_S/cm^2, had impedance measured from 1 MHz to 1 Hz, and was full cell cycled between 1.1V to 3.0V and a rate of 0.02C.

Figure 4.8 presents the cycling data of two full cells using the S/C cathode, accompanied by their respective SEM images of the grid structure. Figure 4.8a shows the EIS performance of cell 1, exhibiting the lowest impedance among our two cells, measuring at 433 Ω. Consequently, it demonstrates the highest initial discharge capacity at 763 mAh/g_S, as illustrated in figure 4.8b. The SEM image inset reveals distinct features indicative of self-supporting characteristics, but layers 1 and 2 have good interlayer contact. The high aspect ratio structures added around 150% increased area for Li ion transfer. This cell was cycled for 16 cycles averaging only 0.25% discharge capacity loss per cycle as shown in figure 4.8b.

Based on the cell data depicted in figure 4.8, the theoretical capacity of elemental sulfur was not achieved, but minimal capacity loss was achieved suggesting that the mechanically confining structure limited capacity fade of the sulfur cathode. Enhancing sulfur utilization requires refining the 3D structure by reducing feature size and bringing features closer together to maintain higher porosity to improve sulfur utilization. Optimization of the cathode's 3D structure could be facilitated through 3D modeling. The cell in figure 4.8 were manually assembled, employing a carbon felt mesh for electronic contact between the cathode and current collector. This interface may have resulted in underutilization of parts of the sulfur cathode. Moreover, improvements in ionic and electronic conductance within the cathode are essential. Enhancements in the 3D structure could improve ionic conductance throughout the cathode, while augmenting carbon content or integrating MIEC Li-garnet could improve electronic conductance.

Table 4.1 presents compiled information regarding the 3D printed structure and cell shown in figure 4.8. Additional surface area denotes the percentage increase compared to a planar interface. Porosity is calculated based on the void space within the grid structure. Impedance is measured via EIS across a frequency range from 1 MHz to 1 Hz. Discharge capacity refers to the initial capacity, while coulombic efficiency represents the final coulombic efficiency.

Additional Surface Area	Porosity	Impedance	Discharge Capacity	Coulombic Efficiency	Capacity Fade per Cycle
150%	68%	433 Ω	763 mAh/g_S	92%	0.25%

4.6.2 Tortuosity and Constriction in Grids

The SEM images of the grid structure clearly reveal additional issues regarding the increased tortuosity of the 3D structure. In certain areas of the second layer, where the ink bridges over the first layer, a direct path to the dense layer is not established. Similarly, as previously noted, excessive self-supporting characteristics of the ink can lead to highly constrictive connections between 3D printed grid layers. Unlike the tortuosity issues associated with the grid structure, this problem can be addressed through meticulous tuning of rheological properties to impart a slightly more conformal nature to the ink, thereby reducing constriction.

However, these issues share a common solution to be explored in future research: the adoption of channel structures rather than grids. Unlike grids, channels repeat the raster pattern directly on top of the previously printed layer instead of alternating patterns. This approach simultaneously addresses the tortuosity issue and mitigates the constriction problem. However, it comes with a trade-off: the grid structure's main benefit is lost. The crossing raster patterns, which help trap the cathode against the electrolyte surface, are forfeited. Yet, this loss could potentially be reversed if the channel separation is drastically reduced.

4.7 Direct Ink Writing Symmetric Cells

One objective of this project was to entirely substitute the 3D porous layer structure with layers printed by a DIW printer. While optimizing the cathode would notably profit from the diminished tortuosity and constriction of the 3D printed

structure, enhancements in anode performance would also be realized since the principles of ion diffusion are universal. Achieving this goal necessitates a printing aid to facilitate 3D printing on both sides. Maintaining sample flatness during direct ink writing is crucial; any thickness variation after the first side is printed and flipped to the other side would affect the 3D printing on the reverse side. Figure 4.9 illustrates a sample holder crafted explicitly for this purpose. Internally, the sample features nine large square inlays where the 3D printed structures on the first side can rest, while the walls of the inlay support the sample. The remainder of the sample is designed to minimize the amount of material needed to create a flat surface to support the rest of the sample.

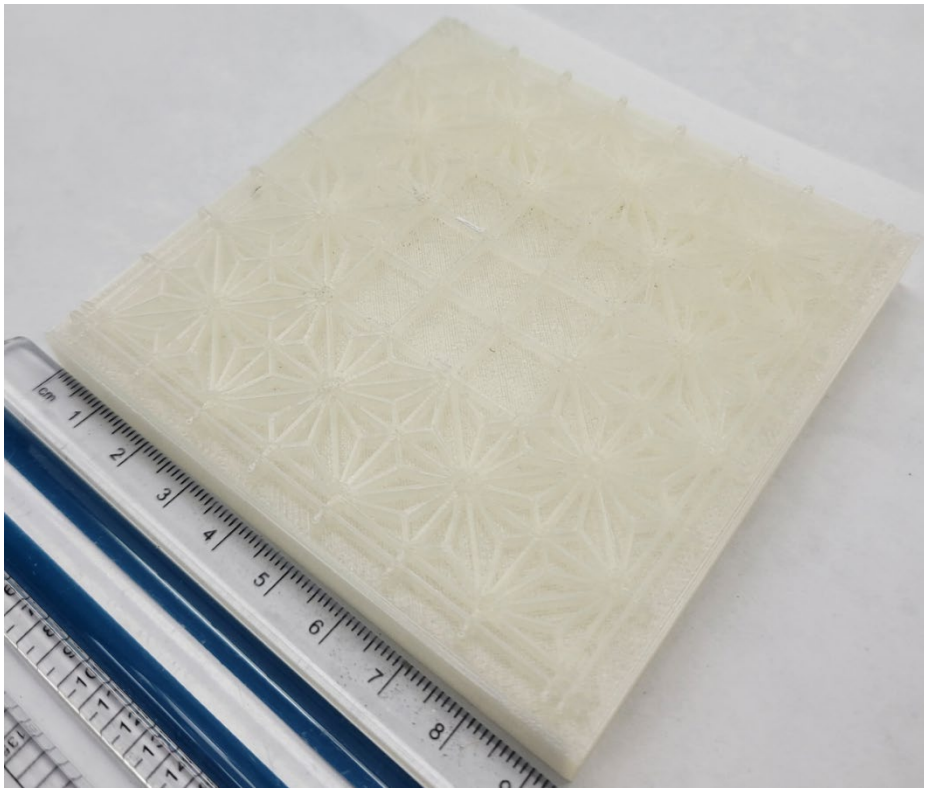

Figure 4.9: Image of the 3D printing support for DIW double-sided samples. Square inlays serve as rests for 3D printing on the first side while the second side is being printed. During the printing process, the sample is secured to the sample holder with tape.

Some observations regarding this process indicate that each side should be 3D printed on a separate day. Rushing through the process could result in sagging of the samples due to organics absorbed by the dense layer softening the dense substrate. Although the amount of organics was significantly reduced, some solvents are still leached out of the inks and into the dense layer. It is crucial that the first layer is allowed to dry completely to ensure sample flatness. Therefore, the first side of the structure is printed on a flat surface and left to dry overnight before being mounted to the sample holder for printing of the second side. Subsequently, the samples can be taken to the furnace for sintering, and if the organic burnout steps are ramped slowly enough, the organics should not cause any defects in the samples due to rapid drying.

For these samples, a slightly thicker dense garnet layer was employed solely to provide additional mechanical support, as the overall mechanical strength conferred by the 3D printed layer remains uncertain. Figure 4.10 illustrates the resulting double-sided 3D printed structure. Good structure and densification was achieved.

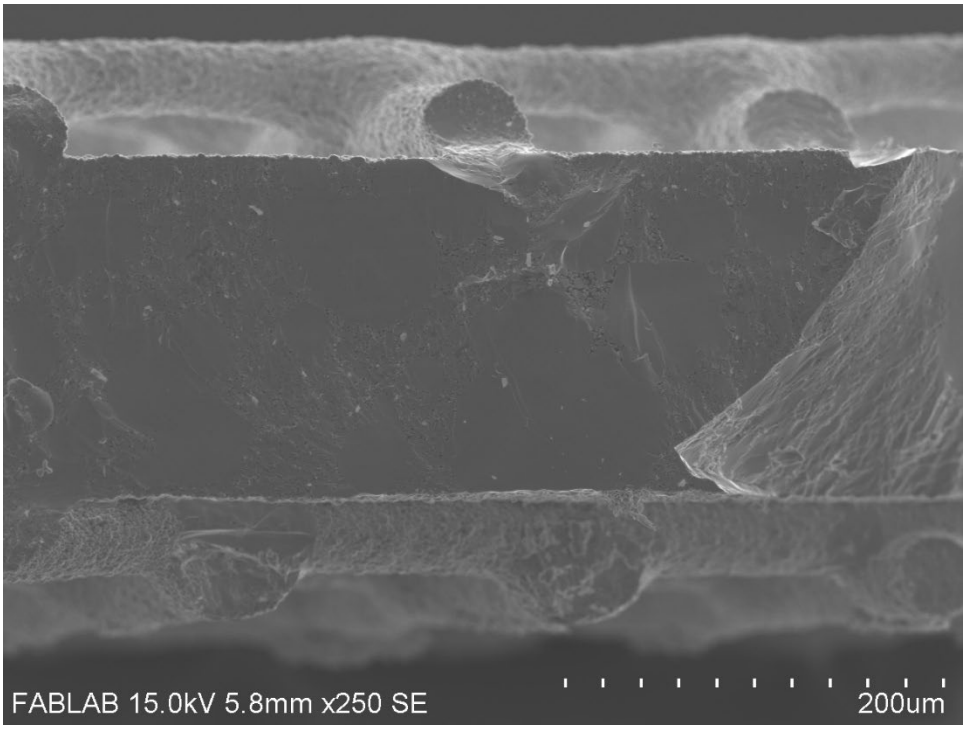

Figure 4.10: SEM cross-sectional image of a symmetrical 3D printed cell. Both grid patterns on opposing sides exhibit self-supporting characteristics while maintaining effective contact with the initial layer to mitigate constriction. The density of the dense layer appears satisfactory for the designated thickness.

The study aimed to investigate the effect of structure and Li+ cycling through a lithium metal symmetric cell analysis. However, issues arose with lithium wetting in the 3D printed structure. Despite attempts with ALD, inconsistent Li wetting into the 3D structure persisted. The cause of these issues remains unclear, but it is hypothesized that the open porosity of the 3D printed structure hinders lithium metal attachment to any surface. Figure 4.11 illustrates the inconsistency in Li wetting observed in the samples, suggesting that refinements in closer features could enhance wetting. Further discussion on this topic will be presented in the future works section.

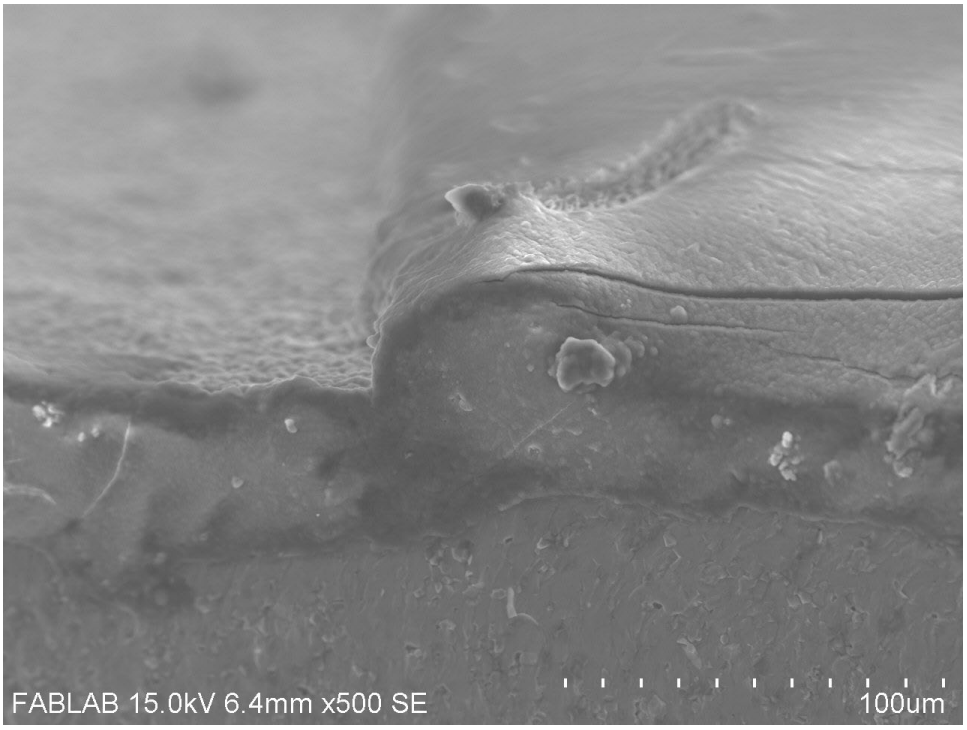

Figure 4.11: The SEM cross-section of a Li wet sample of a 3D printed raster pattern. In the middle of the image, a 3D printed feature is visible, with open space on the left unfilled by Li metal, while the space on the right is fully occupied by Li metal. Uniform application of Li metal was applied across the entire surface of this sample.

4.8 Conclusions

In this chapter, the application of DIW inks to solid-state Li-S batteries employing a stacked grid structure is explored, along with an assessment of the cells' performance through EIS and cell cycling. The results indicate the following:

(1) Precise adjustment of inks plays a crucial role in fabricating self-supporting structures while preventing areas of excessive constriction. In contrast to optimal formulations for DIW column structures, inks with slightly higher conformal characteristics are sought to ensure effective contact between stacked layers. Modest reductions in moduli and marginal increases in τ are potential approaches to achieve such behavior.

(2) The S/carbon nanotube slurry exhibited homogeneity and established good contact with the Li-garnet grid structure, effectively occupying the available pore space. While these structures may not yield as much additional surface area as the random porous layers devised by Hitz et al.,[69] they do offer the reductions to constriction that DIW provides.

(3) 3D printing introduced substantially greater surface area compared to the flat surface of the dense layer. Li-S cycling resulted in a capacity of 763 mAh/g_S with less than 0.25% capacity loss over 16 cycles. Minimal capacity fade was observed with sulfur cathode.

(4) Double-sided DIW structures were realized for future improvement of SSBs through conventional solid-state sintering. Further exploration of optimized structures is necessary to enhance and leverage Li wetting in such samples.

Chapter 5: Overall Conclusions and Future Outlook

The research within this thesis investigated a DIW Li-garnet and variety of possible structures for the future of SSB. Of note, G', G'', and τ where used to characterize and develop high performing inks for DIW Li-garnet. From this increased understanding of rheology high aspect ratio 3D structures could be produced. A summary of these insights and conclusions is shown below, along with potential areas for future research.

5.1 Summary of Research Results

5.1.1 Li-Garnet Inks and their Rheological Properties

The rheological properties of DIW inks, including storage modulus, loss modulus, and recovery time, were thoroughly examined in the context of 3D printed Li-garnet inks. The findings underscore the limitations of stress-strain plots in adequately characterizing complex inks for DIW applications. Instead, stress sweep and time sweep tests emerged as more suitable methodologies for delineating an ink's response to applied stress and its viscoelastic recovery behavior.

Self-supporting inks exhibited distinctive characteristics, including high values of storage modulus (G'), loss modulus (G''), and low relaxation time (τ). The optimization of rheological properties for self-supporting inks was found to hinge on factors such as high solid loading and large particle size for Li-garnet. These attributes play a pivotal role in facilitating the fabrication of high aspect ratio structures, offering promising prospects for advanced DIW applications. Conversely,

conformal inks demonstrated lower G', $G^{"}$, and higher τ compared to their self-supporting counterparts. While conformal inks may not be ideal for certain DIW scenarios, achieving a delicate balance between ink properties is essential for optimizing specific structural configurations.

5.1.2 Li-Garnet Column Structures

The investigation focused on the sintering process of DIW Li-garnet samples and the subsequent assessment of cell performance, encompassing EIS and cycling tests, for 3D printed Li-garnet batteries employing a Li-NMC622 and Li-SPAN systems. The findings unveil several noteworthy observations. Firstly, it was revealed that the reduction of carrier solvents, particularly ethanol, is essential to prevent the detrimental effects of solvent-induced damage to green tapes, as excessive ethanol content led to cracking and rendered the bilayer structure unusable. Secondly, the homogeneity of the NMC/carbon black slurry and its robust adhesion to the Li-garnet layer were found to facilitate the development of low impedance and high-capacity cells. Furthermore, the incorporation of an additional carbon layer via drop casting effectively enhanced electronic conduction within the 3D printed structures, contributing to their overall performance.

Moreover, the analysis revealed that while 3D printing significantly increased surface area compared to the planar configuration of the dense layer, the resulting structures did not match the enhanced surface area achieved by porous layers reported in previous studies. However, it was inferred that further enhancements could be achieved using more self-supporting inks, thereby increasing the surface area-to-

volume ratio of 3D printed structures. Additionally, the implementation of DIW columns with Li-SPAN cells exhibited extremely high specific capacity; however, these efforts ultimately failed due to volume expansion during cycling. Addressing this challenge will require the development of strategies to maintain optimal contact between the Li-garnet and SPAN cathode components through mechanically confining structures.

5.1.3 Li-Garnet Grid Structures

In this chapter, the focus is on the application of DIW inks to solid-state Li-S batteries utilizing a stacked grid structure, coupled with an evaluation of the cells' performance via EIS and cell cycling. Key findings emerged from this investigation. Firstly, meticulous adjustments of inks are paramount in crafting self-supporting structures while averting regions of undue constriction. Unlike the formulations optimized for DIW column structures, the pursuit here is for inks possessing slightly augmented conformal traits to ensure intimate contact between stacked layers. Modest reductions in moduli and marginal increases in τ present potential avenues to attain such desired behavior.

The S/carbon nanotube slurry displayed uniformity and established robust contact with the Li-garnet grid structure, efficiently occupying the available pore space. While these structures may not confer as extensive additional surface area as the random porous layers devised by Hitz et al., they do offer the advantages of constriction reduction afforded by DIW. Furthermore, 3D printing introduced a significantly greater surface area compared to the flat surface of the dense layer. Li-S cycling yielded a capacity of 763 mAh/gS with less than 0.25% capacity loss over 16

cycles, yet enhancements are imperative to optimize sulfur utilization, possibly via the reduction of spacing between features. Additionally, double-sided DIW structures were realized for the future enhancement of SSBs through conventional solid-state sintering, highlighting the need for further exploration of optimized structures to leverage and enhance Li wetting in such samples.

5.2 Future Work

5.2.1 Tying Particle Size to Rheology

Chapter 2 elucidated the significant influence of particle size on the rheological properties of DIW inks. Figure 2.14 reveals a considerable effect on modulus within the range of 300 nm to 425 nm. While it is logical to expect that particle size would influence rheology, the observation that a mere 100 nm difference can result in over two orders of magnitude effect on modulus is surprising. Further investigation into the impact of particle size is warranted.

One limitation encountered in previous studies has been the method used for powder milling. In this thesis, all powders were milled to size using a ball mill in soft bottles. As depicted in figure 2.13, this results in a highly broad distribution of powder size, making it challenging to precisely control the extracted particle size when drawing powder from a large bottle. Exploring additional milling techniques that offer more precise control over particle size distribution is warranted to evaluate the impact of particle size on modulus.

In April 2024, the laboratory acquired a high-energy ball mill for this experiment. Although the ball mill is currently non-operational, the plan is to

commence operations upon acquiring the ZrO2 bottle, allowing for the collection of rheological data, including particle size measurements from a narrow distribution.

5.2.2 Effects of 3D structure on Lithium Cycling

Upon achieving a better understanding of particle size's influence on rheological properties, a transition towards more refined, small aspect ratio DIW structures is envisaged. This transition should facilitate a comprehensive investigation of the impact of 3D structure on Li cycling in symmetric cells. Simultaneously, an independent study could be conducted to determine the necessary separation for optimal Li metal infiltration. It is plausible that attaining the required feature separation for effective Li infiltration may be inconsistent. In such instances, further exploration may involve printing a more textured surface onto the LLZO print to enhance the adherence of Li metal to the electrolyte.

5.2.3 Implementation of MIEC into DIW inks

A recent breakthrough involves the discovery of MIEC Li-garnet, demonstrating potential for enhancing cathode electronic conduction. Given its integration into the cathode structure, there is a drive to incorporate 3D printed structures with minimal tortuosity and constriction using this material. Initial efforts have been made to introduce MIEC into DIW inks, but MIEC does not readily integrate into the ink. Figure 5.1 illustrates the standard LLZO ink and attempts with MIEC inks. While the standard LLZO ink exhibits homogeneity with high viscosity (figure 5.1a), the replacement with MIEC leads to ink phase separation into a viscous

phase and a thin phase (figure 5.1b), neither of which are suitable for DIW. Although some stabilization of the phase was achieved through ink tuning (figure 5.1c), further adjustments to rheology are required to ensure printability. Implementing DIW of MIEC structures could have massive implications for the future of SSBs.

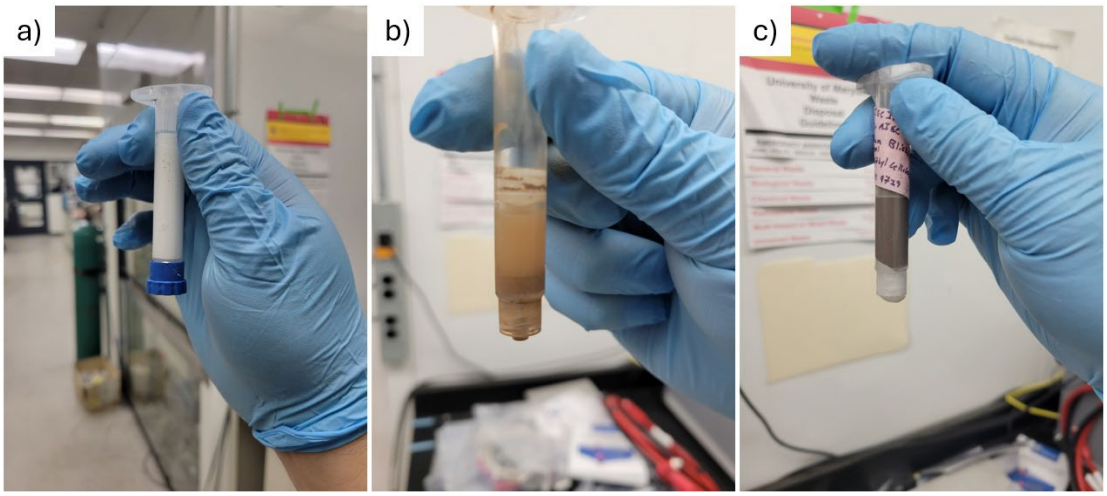

Figure 5.1: Three images of various DIW inks: a) standard LLZO ink, b) MIEC ink with 1 to 1 LLZO replacement, and c) adjusted MIEC ink.

Appendices

Appendix A: Example Ink Recipes for LLZO

Recipes and further information from the inks in figure 2.16.

	Ink 1	Ink 2	Ink 3	Ink 4
LLZO mass (g)	5.0002	5.0080	4.8613	4.9009
ESL mass (g)	1.7556	1.5952	1.6866	1.6644
22 wt% Ethyl-cellulose in Alpha-Terpineol (g)	0.5025	0.6314	.5136	0.5135
LLZO wt%	68.89%	69.22%	68.84%	69.23%
LLZO vol%	33.62%	34.02%	33.58%	33.99%
Average Particle Size (nm)	421.9	376.4	311.7	296.8
Low Stress G' (Pa)	$4.838*10^6$	$4.882*10^5$	$6.912*10^4$	$3.011*10^4$

Appendix B: Excerpt of Text Code Used to 3D Print Column Structures

```
speed   30

move    0       0       10              //initialization
move    0.422   8.55    0
move    0       0       -10
trigwait        0

//border
speed   3
valverel        0.1     0.1
trigwait        0.4                     //startflow
move    0.3     0       0
move    0       -3.031  0
move    1.5     -3.031  0
```

```
move   2.5      0        0
move   1.5      3.031    0
move   -1.5     3.031    0
move   -2.5     0        0
move   -1.5     -3.031   0
valverel        0        0.5
trigwait        0.1
move   0        0        2.43
move   0.25     -2.598   0

//start row 1

//blank
move   0.5      0        0

//blank
move   0.5      0        0

//blank
move   0.5      0        0

move   0        0        -2.43      //prepare to print
valverel        0.2      0.4
trigwait        0.4                 //startflow
speed  1.5                          //printspeed
move   0        0        .03        //columnheight
valverel        0        1.5
trigwait        0.3                 //cutofftime
speed  3                            //anti-pulloff
move   0        0        .4         //createseparation
trigwait        0.0                 //waittime
speed  30                           //transition
move   0        0        2          //move to next column
move   0.5      0        0

move   0        0        -2.43      //prepare to print
valverel        0.2      0.4
trigwait        0.4                 //startflow
speed  1.5                          //printspeed
move   0        0        .03        //columnheight
valverel        0        1.5
trigwait        0.3                 //cutofftime
speed  3                            //anti-pulloff
move   0        0        .4         //createseparation
trigwait        0.0                 //waittime
speed  30                           //transition
```

```
move   0      0      2          //move to next column
move   0.5    0      0

…….

move   0      0      -2.43      //prepare to print
valverel      0.2    0.4
trigwait      0.4               //startflow
speed  1.5                      //printspeed
move   0      0      .03        //columnheight
valverel      0      1.5
trigwait      0.3               //cutofftime
speed  3                        //anti-pulloff
move   0      0      .4         //createseparation
trigwait      0.0               //waittime
speed  30                       //transition
move   0      0      2          //move to next column
move   0.5    0      0

//blank
move   0.5    0      0

//blank
move   0.5    0      0

//blank
move   0.25   0.433  0
//finish
```

Appendix C: Text Code Used to 3D Print Grid Structures

```
speed  5

move   0      0      10
move   0.1    10.5   0
move   0      0      -10
trigwait      5
speed  3
valverel      .5     .25
trigwait      0

move   0      -10    0
move   0.4    0      0

move   10     0      0
move   0      0.3    0
move   -10    0      0
```

```
move  0    0.3  0
move  10   0    0
move  0    0.3  0
move  -10  0    0
move  0    0.3  0
move  10   0    0
move  0    0.3  0
move  -10  0    0
move  0    0.3  0
move  10   0    0
move  0    0.3  0
move  -10  0    0
move  0    0.3  0
move  10   0    0
move  0    0.3  0
move  -10  0    0
move  0    0.3  0
move  10   0    0
move  0    0.3  0
move  -10  0    0
move  0    0.3  0
move  10   0    0
move  0    0.3  0
move  -10  0    0
move  0    0.3  0
move  10   0    0
move  0    0.3  0
move  -10  0    0
move  0    0.3  0
move  10   0    0
move  0    0.3  0
move  -10  0    0
move  0    0.3  0
move  10   0    0
move  0    0.3  0
move  -10  0    0
move  0    0.3  0
move  10   0    0
move  0    0.3  0
move  -10  0    0
move  0    0.3  0
move  10   0    0
move  0    0.3  0
move  -10  0    0
move  0    0.3  0
move  10   0    0
move  0    0.3  0
move  -10  0    0
move  0    0.3  0
move  10   0    0
```

```
move   0      0.3    0
move   -10    0      0
move   0      0.3    0
move   10     0      0
move   0      0.3    0
move   -10    0      0
move   0      0.3    0
move   10     0      0
move   0      0.3    0
move   -10    0      0
move   0      0.3    0
move   10     0      0
move   0      0.3    0
move   -10    0      0
move   0      0.3    0
move   10     0      0
move   0      0.3    0
move   -10    0      0

move   0      0.2    0
move   10.1   0      0
move   0      -10.2  0
move   -10.2  0      0
move   0      10.2   0
move   0.1    0      0

valverel      0      1
trigwait      2
speed  30

move   0      0      3
```

Bibliography

1. Armand, M. & Tarascon, J.-M. Building better batteries. *Nature* **451**, 652–657 (2008).
2. Manthiram, A., Yu, X. & Wang, S. Lithium battery chemistries enabled by solid-state electrolytes. *Nat. Rev. Mater.* **2**, 1–16 (2017).
3. Goodenough, J. B. & Park, K. S. The Li-ion rechargeable battery: A perspective. *J. Am. Chem. Soc.* **135**, 1167–1176 (2013).
4. Albertus, P. *et al.* Challenges for and Pathways toward Li-Metal-Based All-Solid-State Batteries. *ACS Energy Lett.* **6**, 1399–1404 (2021).
5. Department of Energy. How Li-Ion Batteries Work. https://www.energy.gov/science/doe-explainsbatteries#:~:text=When the electrons move from,circuit and discharge the battery.
6. How Batteries Work. https://www.electricity-magnetism.org/electric-battery/how-batteries-work/.
7. Scrosati, B. & Garche, J. Lithium batteries: Status, prospects and future. *J. Power Sources* **195**, 2419–2430 (2010).
8. Lisbona, D. & Snee, T. A review of hazards associated with primary lithium and lithium-ion batteries. *Process Saf. Environ. Prot.* **89**, 434–442 (2011).
9. Mizushima, K., Jones, P. C., Wiseman, P. J. & Goodenough, J. B. LixCoO2 (0<x<1) - a New Cathode Materials for Batteries of High-energy Density. *Mater. Res. Bull.* **15**, 783–789 (1980).
10. Thackeray, M. M., David, W. I. F., Bruce, P. G. & Goodenough, J. B. Lithium Insertion in Manganese Spinels. *Mater. Res. Bull.* **18**, 461–472 (1983).
11. Thomas, M. G. S. R., Bruce, P. G. & Goodenough, J. B. Lithium Mobility in

the Layered Oxide Li1-xCoO2. *Solid State Ionics* **17**, 13–19 (1985).

12. Evarts, E. C. To the Limits of Lithium. *Nature* **526**, S93–S95 (2015).

13. Valøen, L. O. & Reimers, J. N. Transport properties of LiPF6-based Li-Ion battery electrolytes. *J. Electrochem. Soc.* **152**, 882–891 (2005).

14. Xu, K. Nonaqueous liquid electrolytes for lithium-based rechargeable batteries. *Chem. Rev.* **104**, 4303–4417 (2004).

15. Troitzsch, J. H. Electrical applications in Internet of things and e-vehicles: Passive fire safety needs and solutions. *J. Fire Sci.* **40**, 347–363 (2022).

16. Kapp, E. A., Wroth, D. S. & Chapin, J. T. Analysis of Thermal Runaway Incidents Involving Lithium Batteries in U.S. Commercial Aviation. *Transp. Res. Rec.* **2674**, 584–592 (2020).

17. Hess, S., Wohlfahrt-Mehrens, M. & Wachtler, M. Flammability of Li-Ion battery electrolytes: Flash point and self-extinguishing time measurements. *J. Electrochem. Soc.* **162**, A3084–A3097 (2015).

18. Smart, M. C., Ratnakumar, B. V. & Surampudi, S. Electrolytes for Low-Temperature Lithium Batteries Based on Ternary Mixtures of Aliphatic Carbonates. *J. Electrochem. Soc.* **146**, 486–492 (1999).

19. Samsung Note7 Exploded. *Sohu* https://www.sohu.com/a/125020048_467791/ (2017).

20. The iPhone XS Max caught fire for the first time abroad: users said they might sue Apple. *Sohu* https://www.sohu.com/a/285734633_499322/ (2018).

21. A Summary Analysis on the 35 Fire Accidents of New Energy Vehicles in 2016. *Sohu* https://www.sohu.com/a/123335110_526255/ (2017).

22. Electric Vehicle Fire Accident Inventory in the First Half of 2017. *Sohu* https://www.sohu.com/a/155869592_118021/ (2017).

23. Electric Vehicle Fire Accident Inventory in the First Half of 2018. *EV Partner* http://www.evpartner.com/news/8/detail-36915.html/ (2018).

24. Patterson, T. Dreamliner battery probe ends: 8 questions and answers. *CNN* https://www.cnn.com/travel/article/boeing-787-dreamliner-investigation-report/index.html (2014).

25. Neuman, S. Japan: Probe Of Battery Fire On Boeing 787 Finds Improper Wiring. *NPR* https://www.npr.org/sections/thetwo-way/2013/02/20/172485845/japan-probe-of-battery-fire-on-boeing-787-finds-improper-wiring (2013).

26. Blanco, S. Tesla Model S catches fire near Seattle, no injuries reported. *Autoblog* (2013).

27. Lambert, F. Tesla Model S fire vs 35 firefighters - watch impressive operation after a high-speed crash. *Electrek* (2017).

28. Sun, P., Bisschop, R., Niu, H. & Huang, X. *A Review of Battery Fires in Electric Vehicles*. *Fire Technology* vol. 56 (Springer US, 2020).

29. Zhang, S. S. A review on electrolyte additives for lithium-ion batteries. *J. Power Sources* **162**, 1379–1394 (2006).

30. Brissot, C., Rosso, M., Chazalviel, J. & Lascaud, S. Dendritic growth mechanisms in lithium/polymer cells. *J. Po* **81**–**82**, 925–929 (1999).

31. Zhang, S. S. A review on the separators of liquid electrolyte Li-ion batteries. *J. Power Sources* **164**, 351–364 (2007).

32. Aurbach, D. *et al.* Design of electrolyte solutions for Li and Li-ion batteries: A review. *Electrochim. Acta* **50**, 247–254 (2004).

33. Hofmann, A. F., Fronczek, D. N. & Bessler, W. G. Mechanistic modeling of polysulfide shuttle and capacity loss in lithium-sulfur batteries. *J. Power Sources* **259**, 300–310 (2014).

34. Mikhaylik, Y. V. & Akridge, J. R. Polysulfide Shuttle Study in the Li/S Battery System. *J. Electrochem. Soc.* **151**, A1969 (2004).

35. Cheng, Q. *et al.* Full Dissolution of the Whole Lithium Sulfide Family (Li 2 S 8 to Li 2 S) in a Safe Eutectic Solvent for Rechargeable Lithium–Sulfur Batteries. *Angew. Chemie - Int. Ed.* **58**, 5557–5561 (2019).

36. Bhargav, A., He, J., Gupta, A. & Manthiram, A. Lithium-Sulfur Batteries: Attaining the Critical Metrics. *Joule* **4**, 285–291 (2020).

37. Rosenman, A. *et al.* Review on Li-Sulfur Battery Systems: An Integral Perspective. *Adv. Energy Mater.* **5**, 1–21 (2015).

38. Wang, H. *et al.* Graphene-wrapped sulfur particles as a rechargeable lithium-sulfur battery cathode material with high capacity and cycling stability. *Nano Lett.* **11**, 2644–2647 (2011).

39. Ji, X. & Nazar, L. F. Advances in Li-S Batteries. *J. Mater. Chem.* **20**, 9821−9826. (2010).

40. Tarascon, J.-M. & Armand, M. Issues and challenges facing rechargeable lithium batteries. *Nature* **414**, 359–367 (2001).

41. Bruce, P. G., Freunberger, S., Hardwick, L. & Tarascon, J.-M. Li-O2 and Li-S batteries with high energy storage. *Nat. Mater* **11**, 19–29 (2012).

42. Yu, S. *et al.* Elastic Properties of the Solid Electrolyte Li7La3Zr2O12 (LLZO). *Chem. Mater.* **28**, 197–206 (2016).

43. Luntz, A. C., Voss, J. & Reuter, K. Interfacial Challenges in Solid-State Li Ion Batteries. *J. Phys. Chem. Lett.* **6**, 4599–4604 (2015).

44. Xu, W. *et al.* Lithium metal anodes for rechargeable batteries. *Energy Environ. Sci.* **7**, 513–537 (2014).

45. Lin, D., Liu, Y. & Cui, Y. Reviving the lithium metal anode for high-energy batteries. *Nat. Nanotechnol.* **12**, 194–206 (2017).

46. De Luna, Y., Abdullah, M., Dimassi, S. N. & Bensalah, N. All-solid lithium-sulfur batteries: present situation and future progress. *Ionics (Kiel).* **27**, 4937–4960 (2021).

47. Wang, C. *et al.* Garnet-Type Solid-State Electrolytes: Materials, Interfaces, and Batteries. *Chem. Rev.* **120**, 4257–4300 (2020).

48. Ramakumar, S., Deviannapoorani, C., Dhivya, L., Shankar, L. S. & Murugan, R. Lithium garnets: Synthesis, structure, Li+ conductivity, Li+ dynamics and applications. *Prog. Mater. Sci.* **88**, 325–411 (2017).

49. Cussen, E. J. Structure and ionic conductivity in lithium garnets. *J. Mater. Chem.* **20**, 5167–5173 (2010).

50. Thangadurai, V., Narayanan, S. & Pinzaru, D. Garnet-type solid-state fast Li ion conductors for Li batteries: Critical review. *Chem. Soc. Rev.* **43**, 4714–4727 (2014).

51. Fu, Z. & Wachsman, E. Mechanical properties of three-dimensional trilayered Li–garnet electrolyte for high-rate cycling in solid-state batteries. *J. Am.*

Ceram. Soc. **107**, 1481–1489 (2023).

52. Zhu, Y., He, X. & Mo, Y. First principles study on electrochemical and chemical stability of solid electrolyte-electrode interfaces in all-solid-state Li-ion batteries. *J. Mater. Chem. A* **4**, 3253–3266 (2016).

53. Murugan, R., Thangadurai, V. & Weppner, W. Fast lithium ion conduction in garnet-type Li7La 3Zr2O12. *Angew. Chemie - Int. Ed.* **46**, 7778–7781 (2007).

54. Lee, J. M. *et al.* High lithium ion conductivity of Li7La3Zr 2O12 synthesized by solid state reaction. *Solid State Ionics* **258**, 13–17 (2014).

55. Manthiram, A., Fu, Y. & Su, Y. Challenges and Prospects of Lithium-Sulfur Batteries. *Acc. Chem. Res.* **46**, 1125–1134 (2013).

56. Huang, M. *et al.* Effect of sintering temperature on structure and ionic conductivity of Li 7 - XLa 3Zr 2O 12 - 0.5x (x = 0.5 ~ 0.7) ceramics. *Solid State Ionics* **204**–**205**, 41–45 (2011).

57. Wolfenstine, J., Rangasamy, E., Allen, J. L. & Sakamoto, J. High conductivity of dense tetragonal Li 7La 3Zr 2O 12. *J. Power Sources* **208**, 193–196 (2012).

58. Awaka, J., Kijima, N., Hayakawa, H. & Akimoto, J. Synthesis and structure analysis of tetragonal Li7La3Zr2O12 with the garnet-related type structure. *J. Solid State Chem.* **182**, 2046–2052 (2009).

59. Rangasamy, E., Wolfenstine, J. & Sakamoto, J. The role of Al and Li concentration on the formation of cubic garnet solid electrolyte of nominal composition Li 7La 3Zr 2O 12. *Solid State Ionics* **206**, 28–32 (2012).

60. Huang, M., Dumon, A. & Nan, C. W. Effect of Si, in and Ge doping on high ionic conductivity of Li 7La 3Zr 2O 12. *Electrochem. commun.* **21**, 62–64

(2012).

61. Wang, Y. & Lai, W. Phase transition in lithium garnet oxide ionic conductors Li7La3Zr2O12: The role of Ta substitution and H2O/CO2 exposure. *J. Power Sources* **275**, 612–620 (2015).

62. Ahn, J. H., Park, S. Y., Lee, J. M., Park, Y. & Lee, J. H. Local impedance spectroscopic and microstructural analyses of Al-in-diffused Li7La3Zr2O12. *J. Power Sources* **254**, 287–292 (2014).

63. Ohta, S., Kobayashi, T. & Asaoka, T. High lithium ionic conductivity in the garnet-type oxide Li7-X La3(Zr2-X, NbX)O12 (X = 0-2). *J. Power Sources* **196**, 3342–3345 (2011).

64. Kihira, Y., Ohta, S., Imagawa, H. & Asaoka, T. Effect of simultaneous substitution of alkali earth metals and nb in li7la3zr2o12 on lithium-ion conductivity. *ECS Electrochem. Lett.* **2**, 3–7 (2013).

65. Han, X. *et al.* Negating interfacial impedance in garnet-based solid-state Li metal batteries. *Nat. Mater.* **16**, 572–579 (2017).

66. Luo, W. *et al.* Transition from Superlithiophobicity to Superlithiophilicity of Garnet Solid-State Electrolyte. *J. Am. Chem. Soc.* **138**, 12258–12262 (2016).

67. Wang, C. *et al.* Conformal, Nanoscale ZnO Surface Modification of Garnet-Based Solid-State Electrolyte for Lithium Metal Anodes. *Nano Lett.* **17**, 565–571 (2017).

68. Tsai, C. L. *et al.* Li7La3Zr2O12 Interface Modification for Li Dendrite Prevention. *ACS Appl. Mater. Interfaces* **8**, 10617–10626 (2016).

69. Hitz, G. T. *et al.* High-rate lithium cycling in a scalable trilayer Li-garnet-

electrolyte architecture. *Mater. Today* **22**, 50–57 (2019).

70. Xu, S. *et al.* All-in-one lithium-sulfur battery enabled by a porous-dense-porous garnet architecture. *Energy Storage Mater.* **15**, 458–464 (2018).

71. Yi, E. *et al.* All-Solid-State Batteries Using Rationally Designed Garnet Electrolyte Frameworks. *ACS Appl. Energy Mater.* **3**, 170–175 (2020).

72. Xu, S. *et al.* Three-Dimensional, Solid-State Mixed Electron-Ion Conductive Framework for Lithium Metal Anode. *Nano Lett.* **18**, 3926–3933 (2018).

73. Fu, K. *et al.* Three-dimensional bilayer garnet solid electrolyte based high energy density lithium metal-sulfur batteries. *Energy Environ. Sci.* **10**, 1568–1575 (2017).

74. Alexander, G. V., Shi, C., O'Neill, J. & Wachsman, E. D. Extreme lithium-metal cycling enabled by a mixed ion- and electron-conducting garnet three-dimensional architecture. *Nat. Mater.* **22**, 1136–1143 (2023).

75. Sharafi, A., Meyer, H. M., Nanda, J., Wolfenstine, J. & Sakamoto, J. Characterizing the Li-Li7La3Zr2O12 interface stability and kinetics as a function of temperature and current density. *J. Power Sources* **302**, 135–139 (2016).

76. Sharafi, A., Haslam, C. G., Kerns, R. D., Wolfenstine, J. & Sakamoto, J. Controlling and correlating the effect of grain size with the mechanical and electrochemical properties of Li7La3Zr2O12 solid-state electrolyte. *J. Mater. Chem. A* **5**, 21491–21504 (2017).

77. Hamann, T. *et al.* The Effects of Constriction Factor and Geometric Tortuosity on Li-Ion Transport in Porous Solid-State Li-Ion Electrolytes. *Adv. Funct.*

Mater. **30**, (2020).

78. Tjaden, B., Brett, D. J. L. & Shearing, P. R. Tortuosity in electrochemical devices: a review of calculation approaches. *Int. Mater. Rev.* **63**, 47–67 (2018).

79. Vivet, N. *et al.* 3D Microstructural characterization of a solid oxide fuel cell anode reconstructed by focused ion beam tomography. *J. Power Sources* **196**, 7541–7549 (2011).

80. Stenzel, O., Pecho, O., Holzer, L., Neumann, M. & Schmidt, V. Predicting Effective Conductivities Based on Geometric Microstructure Characteristics. *AIChE J.* **62**, 1834 (2016).

81. Fu, Z. *et al.* Probing the Mechanical Properties of a Doped Li7La3Zr2O12Garnet Thin Electrolyte for Solid-State Batteries. *ACS Appl. Mater. Interfaces* **12**, 24693–24700 (2020).

82. McOwen, D. W. *et al.* 3D-Printing Electrolytes for Solid-State Batteries. *Adv. Mater.* **30**, 1–7 (2018).

83. Deshpande, A. P., Krishnan, J. & Kumar, P. B. S. *Rheology of Complex Fluids*. (Springer New York, 2010). doi:10.1007/978-1-4419-6494-6.

84. Busch, A. *et al.* Rheological characterization of Polyanionic Cellulose solutions with application to drilling fluids and cuttings transport modeling. *Appl. Rheol.* **28**, 1–17 (2018).

85. Nan, B., Galindo-Rosales, F. J. & Ferreira, J. M. F. 3D printing vertically: Direct ink writing free-standing pillar arrays. *Mater. Today* **35**, 16–24 (2020).

86. Eom, Y., Kim, F., Yang, S. E., Son, J. S. & Chae, H. G. Rheological design of 3D printable all-inorganic inks using BiSbTe-based thermoelectric materials. *J.*

Rheol. (N. Y. N. Y). **63**, 291–304 (2019).

87. Loh, H. A., Graves, A. R., Stinespring, C. D. & Sierros, K. A. Direct ink writing of graphene-based solutions for gas sensing. *ACS Appl. Nano Mater.* **2**, 4104–4112 (2019).

88. Zhang, L. *et al.* In-situ preparation of copper azide by direct ink writing. *Mater. Lett.* **238**, 130–133 (2019).

89. Manthiram, A. A reflection on lithium-ion battery cathode chemistry. *Nat. Commun.* **11**, 1–9 (2020).

90. Li, M., Lu, J., Chen, Z. & Amine, K. 30 Years of Lithium-Ion Batteries. *Adv. Mater.* **30**, 1–24 (2018).

91. Dixit, M., Markovsky, B., Schipper, F., Aurbach, D. & Major, D. T. Origin of Structural Degradation during Cycling and Low Thermal Stability of Ni-Rich Layered Transition Metal-Based Electrode Materials. *J. Phys. Chem. C* **121**, 22628–22636 (2017).

92. Lipson, A. L. *et al.* Improving the Thermal Stability of NMC 622 Li-Ion Battery Cathodes through Doping during Coprecipitation. *ACS Appl. Mater. Interfaces* **12**, 18512–18518 (2020).

93. Zhang, N. *et al.* Structural, Electrochemical, and Thermal Properties of Nickel-Rich LiNi x Mn y Co z O 2 Materials. *Chem. Mater.* **30**, 8852–8860 (2018).

94. Bak, S. *et al.* Structural Changes and Thermal Stability of Charged LiNi. *Appl. Mater. Interfaces* **6**, 22594–22601 (2014).

95. Esho, I., Shah, K. & Jain, A. Measurements and modeling to determine the critical temperature for preventing thermal runaway in Li-ion cells. *Appl.*

Therm. Eng. **145**, 287–294 (2018).

96. Kong, L., Li, C., Jiang, J. & Pecht, M. G. Li-ion battery fire hazards and safety strategies. *Energies* **11**, 1–11 (2018).

97. Huawei P9 Plus Exploded and the Attitude Was Worse Than Samsung Note7. *Sohu* https://www.sohu.com/a/116273061_162764/ (2016).

98. Jerico Mandybur. Man claims iPhone 7 burst into flames in his car. *Mashable* https://mashable.com/article/iphone7-reportedly-catches-fire-in-australia (2016).

99. Fingas, R. iPhone battery fire forces brief evaluation of Zurich Apple store. *Apple Insider* https://appleinsider.com/articles/18/01/09/iphone-battery-fire-forces-brief-evacuation-of-zurich-apple-store (2018).

100. Liu, B. *et al.* 3D lithium metal anodes hosted in asymmetric garnet frameworks toward high energy density batteries. *Energy Storage Mater.* **14**, 376–382 (2018).

101. Shen, H. *et al.* Oriented porous LLZO 3D structures obtained by freeze casting for battery applications. *J. Mater. Chem. A* **7**, 20861–20870 (2019).

102. Godbey, G. L. *et al.* Direct Ink Writing of Li7La3Zr2O12 Electrolytes for Low Tortuosity Li-NMC Solid-State Batteries. *To be Submitt.* **1**, (2024).

103. Hawley, W. B. & Li, J. Electrode manufacturing for lithium-ion batteries—Analysis of current and next generation processing. *J. Energy Storage* **25**, 1–37 (2019).

104. Muralidharan, N. *et al.* Next-Generation Cobalt-Free Cathodes – A Prospective Solution to the Battery Industry's Cobalt Problem. *Adv. Energy Mater.* **12**, 1–

16 (2022).

105. Wei, S., Ma, L., Hendrickson, K. E., Tu, Z. & Archer, L. A. Metal-Sulfur Battery Cathodes Based on PAN-Sulfur Composites. *J. Am. Chem. Soc.* **137**, 12143–12152 (2015).

106. Ahmed, M. S. *et al.* Multiscale Understanding of Covalently Fixed Sulfur–Polyacrylonitrile Composite as Advanced Cathode for Metal–Sulfur Batteries. *Adv. Sci.* **8**, 1–34 (2021).

107. Beltran, S. P. & Balbuena, P. B. Sulfurized Polyacrylonitrile (SPAN): Changes in Mechanical Properties during Electrochemical Lithiation. *J. Phys. Chem. C* **125**, 13185–13194 (2021).

108. Shi, C. *et al.* All-Solid-State Garnet Type Sulfurized Polyacrylonitrile/Lithium-Metal Battery Enabled by an Inorganic Lithium Conductive Salt and a Bilayer Electrolyte Architecture. *ACS Energy Lett.* 1803–1810 (2023) doi:10.1021/acsenergylett.3c00380.

109. Gandon, S. No Cobalt, No Tesla? (2017).

110. Xin, S. *et al.* Smaller sulfur molecules promise better lithium'sulfur batteries. *J. Am. Chem. Soc.* **134**, 18510–18513 (2012).

111. Zhao, M., Li, B. Q., Zhang, X. Q., Huang, J. Q. & Zhang, Q. A Perspective toward Practical Lithium-Sulfur Batteries. *ACS Cent. Sci.* **6**, 1095–1104 (2020).

112. Tian, H. K., Liu, Z., Ji, Y., Chen, L. Q. & Qi, Y. Interfacial Electronic Properties Dictate Li Dendrite Growth in Solid Electrolytes. *Chem. Mater.* **31**, 7351–7359 (2019).

113. Basappa, R. H., Ito, T. & Yamada, H. Contact between Garnet-Type Solid Electrolyte and Lithium Metal Anode: Influence on Charge Transfer Resistance and Short Circuit Prevention. *J. Electrochem. Soc.* **164**, A666–A671 (2017).

114. Yonemoto, F. *et al.* Temperature effects on cycling stability of Li plating/stripping on Ta-doped Li7La3Zr2O12. *J. Power Sources* **343**, 207–215 (2017).

115. van den Broek, J., Afyon, S. & Rupp, J. L. M. Interface-Engineered All-Solid-State Li-Ion Batteries Based on Garnet-Type Fast Li+ Conductors. *Adv. Energy Mater.* **6**, 1–11 (2016).

116. Godbey, G. L. *et al.* Direct Ink Writing of Li7La3Zr2O12 Electrolytes for Low Tortuosity Stacked-Rastor Li-S Solid-State Batteries. *To be Submitt.* **1**, (2024).